# ENGINEERING ROBUST AND ENTANGLED CAT STATES IN SUPERCONDUCTING BOSONIC CIRCUITS

by

**JONATHAN SCHWINGER**

*(M. Sc., Ruhr University Bochum)*

**A THESIS SUBMITTED**

**FOR THE DEGREE OF DOCTOR OF PHILOSOPHY**

**CENTRE FOR QUANTUM TECHNOLOGIES**

**NATIONAL UNIVERSITY OF SINGAPORE**

**2025**

Supervisor:
Assistant Professor Yvonne Y. Gao

Examiners:
Associate Professor Dzmitry Matsukevich
Associate Professor Dagomir Kaszlikowski
Associate Professor Warit Asavanant, University of Tokyo

# Declaration

I hereby declare that this thesis is my original work and it has been written by me in its entirety. I have duly acknowledged all the sources of information which have been used in the thesis.

This thesis has also not been submitted for any degree in any university previously.

Jonathan Schwinger

30 July 2025

*To my family.*
*My parents, Annette and Bernd, whose unwavering support*
*continues to carry me through this world.*
*My sister Muriel, whose strength and perseverance in the face of*
*hardship never fail to inspire me.*
*My cousins, Christian and Manuel, who sparked in me a love for*
*physics that culminated in this thesis.*

# Acknowledgments

With all the effort required to conceive, plan, and execute the experiments reported in this thesis, writing these acknowledgments has proven to be the most difficult challenge. While every line brings me closer to completing my thesis and earning my PhD, it also brings me closer to graduating from Qcrew and saying goodbye. Though certainly not final, this departure leaves a bittersweet aftertaste.

While there are many people to thank, one name stands out first. **Yvonne Gao**, your decision to accept me as your first PhD student and allow me to help build and shape the lab while growing alongside it has been one of the greatest privileges and joys of my life. Through your guidance, I truly came to understand what it means to be a great scientist, never losing sight of the goal while achieving understanding through structure, consolidating ideas, and distilling them to their core. I want to thank you for your mentorship and for being an excellent role model, both as a scientist and as a leader. You taught me countless things in the lab and many more during our casual conversations at daily lunches. Among all your talents, your ability to select the right members for the lab has been outstanding. While the science was exceptional, the reason I will always look back on my PhD years as one of the best times of my life is the team and environment you allowed to blossom.

While a few paragraphs are hardly enough to convey my gratitude to all of you properly, I will give it my best try.

**Atharv Joshi**, not only are you the true OG of the Gaogang, but you are also my first friend in Singapore. I remember our first virtual meeting vividly, even before arriving in Singapore, I already knew I had found a friend. What I could not have known then is how important a friend you would become and how much I would learn from working alongside you. Your meticulously organized work style left me in awe more than once, and your dedication set me and the lab on the path to success. I miss hearing about your coffee experiments, random bits of trivia, and our philosophy discussions after a few glasses of booze. My sadness at your leaving was overshadowed only by the pride and joy I felt knowing you got into a PhD program of your choice!

**Fernando Valadares Calheiros de Siqueira**. Where to start? You joined shortly after me and are thus the one constant throughout my PhD. From the start, we just clicked, sharing the same sense of humor, love for science, and passion for video games. Besides the many things I learned from working beside you, I want to thank you for all the small daily interactions that brighten my day. Together, we have faced and beaten many challenges, like Dark Souls, Elden Ring, and setting up two labs. You are a great scientist, and you often inspired me to level up my game. I wish we had the opportunity to work on a project together. I wish you all the best in Canada and hope that one day you can show me the beauty of Brazil.

**Kong Lingda**, we first met by memeing back and forth in your quantum optics homework. I was thrilled when you joined our lab afterwards. My back thanks you for some of the best massages, and I thank you for being a great friend and for all the piggyback rides through the CQT corridors. I hope that our paths cross again.

**Weipin Maximilian Chua**, few people have had as profound an impact on my life in the last five years as you. After we'd known each other only a short time, you invited me to your home, introduced me to your friends, and thereby made me feel at home. You have the special ability to make any activity you're part of more fun, and I honestly admire your authenticity in living the 'too smart to be an Ah Beng' lifestyle. Some part of me selfishly hopes you will stay in Singapore while I am still here, but visiting you in Switzerland and conquering the Alps wouldn't be too bad either.

**Adrian Copetudo Espinosa**, I am deeply grateful for our shared memories as labmates and flatmates. We climbed mountains, explored mines, drove through Death Valley, enjoyed the wine, paella, and beaches of Barcelona, and occasionally did some science. Your gentleness, willingness to help, and hard work will surely help you succeed in whatever comes your way.

**Clara Yun Fontaine**, my PhD experience would not have been the same without you. You have expanded my awareness in so many domains, from realizing the importance of shaping your own experiences to many new fruits I didn't know existed. I deeply admire your insistence on having a voice and speaking up for what you believe, despite facing adversity. You are also one of the best presenters I have met, and I have learned a lot from you. Your contributions to Qcamp and the entire Quantum community in Singapore deserve much more praise than you are getting. I am excited to see the path you carve for yourself and where it leads you.

**Xiaozhou Pan**, we worked together on the compressed cat project, which is now the core of this PhD thesis, and your hard work and expertise were crucial for its successful outcome. Looking back, I romanticize those first years of us working together and figuring everything out. I wish you all the best as you start your research group.

**Pengtao Song**, your joining the lab was a blessing. You taught me a great deal about general lab operations and how to operate the fridge without breaking a sweat. Whenever there was a problem, a power shutdown, or cooling water issues, you remained iconically calm and knew what to do. Knowing that you were always there to turn to for help gave me great peace of mind. Thank you for this.

**Ni-Ni Huang**, nice to e-meet you, a line as iconic as its speaker. We collaborated on the compressed cat project, and I would like to thank you for your diligent efforts, which were instrumental to its success. Watching your growth over the past years has been one of the many joys of my PhD journey. Beyond this, it's impossible to overstate how much fun I have bickering with you. You have the most expressive facial reactions, which probably make up 80% of all the stickers on my phone. Furthermore, my palate thanks you for all the delicious food you've introduced us to.

**Fumiya Hanamura**, we only got to work together for a brief time, but that was enough for you to have a significant impact on my PhD. Thanks to your theoretical insights, we were able to give the compressed cat the story it deserved. Talking with you has often been a humbling experience, and I want to thank you for entertaining my questions and teaching me so much in the process. I'm glad you found your way back to Singapore so we can hang out more. Visiting the Furusawa Lab in Tokyo was a real highlight for me. Thank you for making this possible.

**Kyle Chu** is the superhero we need but don't deserve. Even while juggling too many tasks at once, you always find time to help the people around you, and you never lose patience. Thank you for the many hours of debugging you saved me from. The fact that I'm now moving on to work with and under you speaks volumes about how much I appreciate and respect you. Looking forward to the fun times ahead!

**Amon Maria Kasper**, it's remarkable how seemingly unassuming decisions can set actions in motion. My decision to join the NUS calisthenics training at the beginning of my PhD was one of those, as this is where I first met Mr. Full Enjoy Travel himself. I want to thank you for your friendship over the past few years. Whether it was a spontaneous weekend trek up Mt. Kinabalu or celebrating my 30th birthday moshing to ASAP Rocky. We share many memories that hold great meaning for me. Your consistently cheerful spirit is contagious, and I wouldn't have had nearly as much fun without you.

**Aleksandr Dorogov**, there really is nothing pusillanimous about your approach to life. You don't look for a good time; you make the good time happen. Your energetic good morning greetings in all languages of the world are still ringing in my ears. I genuinely believe that one could lock you in an empty room, throw away the key, and you would still have a better time than most people on their best night out. I want to thank you for always lighting up the mood and for some of the most interesting conversations about life, politics, and physics. It was an honor to be your senior.

**I Wayam Gedeh Tanjung Krisnanda**, you are a late joiner to Qcrew, but turned very quickly into a pillar, holding us all up. You are a menace of a scientist, a formidable mentor, a climber operating on gradient ascent, and a great friend. There have been many days when I just came to the office to chit-chat with you, make sure you don't go to lunch without me, and hear the latest proudly reported updates on your baby. Thank you for answering all my theory questions and for never failing to lift my spirit with your never-fading smile.

**Kehui Yu**, I was lucky enough to work with you on the entanglement project. You turned every idea I threw at you into something concrete and quickly provided the encompassing theory. I want to thank you for your forward-thinking, can-do attitude. I hope to visit you soon in China and hit the road together.

**May Chee Loke**, I want to thank you for the last few years that we spent working together. The demonstration of tripartite entanglement would not have been possible without your incredible hard work and dedication. While leaving it to you to finish the project is the one regret of my PhD, working with you has been one of the absolute highlights. You have grown enormously during this time, and I am proud to have contributed to that. I hope that you find more time to cultivate your many other hobbies; your quantum poem is beautiful. I wish you all the luck for what is coming next and hope to visit you during your PhD.

**Celine Trieu**, you went from the mysterious girl from Hamburg who was going to join our lab to a dear friend. Many times, when I had a rough day, a quick back-and-forth with you gave me a new burst of energy. Thank you for that. The sunfish you made for my graduation is one of my favorite gifts ever!

**Andrea Duina**, I am thankful that we got to work together. Many things connected us, our love for Zelda being just one of them. You must have had a fairy aiding you when making the hero cable, which remains unbeaten to this day. Our trip to Phuket has been one of my favorites, and undoubtedly not because of Phuket itself. Thank you for the best tennis matches and Roman pasta. Your PhD position at EPFL is very well deserved.

**Aniket Chatterjee**, it was my privilege to assist you on the Readout project. Your enthusiasm and curiosity are contagious, turning the project into an absolute treat. Your well-thought-out questions revealed several blind spots in my understanding, allowing me to learn a great deal in the process. I am thrilled that our hard work and after-hours meetings paid off and turned into a neat paper.

**Steven Touzard**, you had an enormous influence on my PhD. My thesis builds directly on your work, and I learned so much from our conversations and from reading your thesis over and over again. Your explanations are among the clearest I've found and greatly helped me appreciate the amazing science of bosonic cQED. I also have to give you a shout-out for great taste. The formatting of my thesis is directly inspired by yours.

**Alexander Hue**, my PhD experience started with you, and I am happy that you were able to make it to my defense. You were one of the first people I met in CQT and were an enormous help in showing me the ropes. Your three-day crash course in thermo and stat mech not only helped me through QE 1, but also nurtured my love for physics. I've been increasingly busy in the last two years of my PhD, and we haven't had the chance to hang out as often as we used to. Thank you for being one of my first friends in Singapore, and I look forward to hanging out more often in the future.

There are many people in and around CQT without whom my PhD would not have been possible. **Mohammad Imran**, you are an absolute legend at CQT. Not only was every chat with you an absolute pleasure, but I always came out learning something new. I want to thank the CQT **Admin Team** for doing a fantastic job, checking in on me during my quarantine and during the preparation of my thesis, and always being flexible and helpful with any issue I brought to them. Every morning, the first thing I would do is to visit **Uncle Wong**. I don't know how many of your coffees I drank during my PhD, but it must be in the upper hundreds.

I thank the members of my committee **Dzmitry Matsukevich**, **Dagomir Kaszlikowski**, and **Warit Asavanant** for evaluating my thesis. Your comments improved it. It is also good to know that there is a guaranteed readership.

I want to thank **Amber Zhai**. Your companionship during these last few years means a lot to me, and many of my best memories in Singapore are with you. You were a constant source of joy and happiness and an important counter-balance to my research life.

Finally, I want to thank my family. None of this would have been possible without your everlasting support. You nurtured my curiosity and helped me through every step along the way. **Annette** and **Bernd**, you are my role models for parenting done right. **Muriel**, thank you for paving the way throughout my childhood. I am glad that you are my older sister. Even if distance separates us, I know that you all are always with me.

# Contents

# Abstract

Engineering Robust and Entangled Cat States in Superconducting Bosonic Circuits

by

Jonathan Schwinger

Superconducting circuits have emerged as one of the most promising platforms in the race to build a useful quantum computer. Recent advances harness the extensive Hilbert space of Quantum Harmonic Oscillators (QHOs) to significantly reduce the overhead required for Quantum Error Correction (QEC). This hardware-efficient approach represents a broader paradigm shift. Rather than constructing hardware to fit the theoretical vision of an error-corrected quantum computer, hardware and theory are co-developed to identify optimal codewords that leverage intrinsic symmetries and capitalize on knowledge of dominant error channels.

This thesis demonstrates how hardware-aware design principles lead to more robust quantum codewords and enable efficient control schemes for generating multipartite entanglement. In the first experiment, we demonstrate deterministic protection of non-Gaussian interference features of cat states against photon loss, the dominant error channel in superconducting cavities. We report a five-fold increase in the lifetime of the coherence features of a cat state of size $1.8$ with $-7.6$ dB compression. We achieve this by engineering their phase-space distribution using a technique based on Echoed Conditional Displacement (ECD) gates.

In the second experiment, we exploit the multimode capabilities of ECD gates to implement and characterize tripartite entanglement. We create a GHZ-cat state and a W-cat state and experimentally demonstrate the creation of genuine tripartite entanglement. Furthermore, we efficiently characterize these macroscopic, entangled states by establishing a mapping between points in the high-dimensional multimode joint characteristic function and Pauli operators.

The results presented in this thesis demonstrate the vast potential of bosonic circuit quantum electrodynamics architectures for efficient quantum information storage and processing. The tools and protocols we develop have broad applications beyond quantum computing, including quantum metrology, quantum communication, and fundamental studies at the classical-quantum boundary.

# List of preprints and publications

## Core work presented in this thesis

1. X. Pan, **Schwinger, Jonathan**, N.-N. Huang, P. Song, W. Chua, F. Hanamura, A. Joshi, F. Valadares, R. Filip, and Y. Y. Gao, "Protecting the quantum interference of cat states by phase-space compression", *Physical Review X*, vol. 13, no. 2, p. 021 004, 2023

2. **Schwinger, Jonathan**, M. C. Loke, K. Yu, T. Krisnanda, A. Joshi, A. Kasper, and Y. Y. Gao, "Creating tripartite entangled states in bosonic cqed", in preparation, 2025

These two papers contain the main results of this thesis. They present details about phase-space engineering techniques to protect cat state coherences and the creation of tripartite entangled cat states.

## Related publications

3. A. Chatterjee, **Schwinger, Jonathan**, and Y. Y. Gao, "Enhanced qubit readout via reinforcement learning", *Physical Review Applied*, vol. 23, no. 5, p. 054 057, 2025

This paper details the development of a new readout waveform using a reinforcement learning agent.

# List of figures

# List of tables

# Chapter 1

# Introduction

## 1.1 Prologue

Looking back, the convergence of quantum mechanics and computer science into the field of quantum computation appears to be a foregone conclusion. Quantum mechanical systems exhibit phenomena, such as superposition and entanglement, that classical computers cannot capture. The exponential scaling classical computers face when simulating quantum systems exposes a daunting bottleneck. Nature effortlessly performs calculations that classical computers struggle to handle. Quantum computation emerged at this crossroad towards the end of the 20th century. Following, I will briefly recount the modern history of both fields, their eventual merger, and how my thesis fits into this context.

Living means constant problem-solving. As societies grew and technologies advanced, so did the complexity of the problems they faced. This increasing complexity drove the invention of novel, increasingly sophisticated computing tools, starting with mechanical machines like the ancient abacus (2700-2300 B.C.) and Charles Babbage's Analytical Engine (1830s). By the beginning of the 20th century, computational demands from scientific, economic, and, unfortunately, military applications skyrocketed. A new computational paradigm was needed.

In 1936, Alan Turing published a breakthrough paper [1] introducing the concept of universal computation. Instead of building a specialized machine for each task, he envisioned and proved that a single machine could, in principle, solve any problem reducible to well-defined calculations. This is formalized in the Church-Turing principle, which states that any computation that can be performed by following a finite set of rules can be done by Turing's abstract machine. While Turing conceptualized computation using abstract symbols on an infinite tape, Claude Shannon's insights transformed these theoretical ideas into practically implementable systems.

In 1938, in arguably one of the most profound master's theses ever written [2], Shannon demonstrated how Boolean algebra can be mapped onto electrical switching circuits, establishing the foundation for digital circuit design. Shannon did not stop there. A decade later, his landmark 1948 paper "A Mathematical Theory of Communication" [3] established information as a precisely quantifiable entity and formalized the bit as its fundamental unit. This work bridged the gap between information as a theoretical abstraction and its physical implementation with binary systems as its basic language. Or so it seemed. Just as quantum mechanics disrupted the view that physics was nearly complete at the beginning of the 20th century, it eventually demonstrated that classical information is an inadequate description of reality.

On December 14, 1900, Max Planck presented what he called "an act of desperation". In an attempt to bring his theory (Planck-Wien law) into accordance with experimental data, he concluded that energy itself must be composed of a definite number of equal parts called quanta. However, he saw it as no more than mathematical trickery, leaving question marks rather than a proper understanding. It was Einstein who took the next step. Taking Planck's idea seriously, he used it to explain the photoelectric effect [4]. In the traditional Maxwell picture of light, the energy of a light beam increases with its intensity. However, the photoelectric effect shows that even a high-intensity, low-frequency beam cannot cause electron emission, whereas a low-intensity, high-frequency beam can. To make sense of it, Einstein proposed that light is not a wave, but composed of individual particles, light quanta (later called photons), each storing a fixed amount of energy proportional to their frequency $E = hf$. Hence, only above a specific frequency does a quantum possess enough energy to overcome the binding energy of an electron, leading to its photoemission.

While this explained the photoelectric effect, it raised an entirely new question. What is light? Is it a wave or a particle? To add to the confusion, Louis de Broglie postulated in his PhD thesis (1924) [5] that electrons and all matter have wave properties. Davisson and Germer experimentally proved this fact in 1927 [6]. Bohr addressed the wave-particle paradox with his complementarity principle, arguing that quantum objects exhibit both wave and particle properties. Still, these complementary aspects cannot be observed simultaneously.

Despite many revolutionary insights, quantum theory lacked a comprehensive mathematical framework for fully describing quantum phenomena. This theoretical gap led to intense discussions among physicists and mathematicians, ultimately resulting in two complementary formulations. Heisenberg's matrix mechanics, Schrödinger's wave mechanics, and eventually von Neumann's rigorous mathematical foundation [7] that unified these approaches and established the abstract Hilbert space formalism for quantum mechanics.

By the mid-1930s, quantum theory had matured from a controversial theory into an established framework for understanding microscopic phenomena. While operational, quantum theory left some of its founders with unease. Deeply troubled by the abandonment of determinism and physical realism, Einstein proposed, along with Podolsky and Rosen, a thought experiment that they believed exposed a flaw in quantum mechanics [8]. In what is now known as the EPR paradox, they pointed out that quantum theory allows correlations between distant particles and entanglement, and used this to argue against the locality principle. They proposed a way out. Quantum mechanics is an incomplete theory, and there are hidden variables that, if known, would restore determinism and realism in quantum mechanics.

In 1964, Bell developed a mathematical inequality that could be experimentally tested to distinguish between the existence and non-existence of hidden variables [9]. Clauser conducted the first experimental tests of Bell's inequality in 1972 [10], which was subsequently refined by Aspect in 1982 [11]. Since then, further Bell test experiments have been done, each more rigorous than the last. In 2015, groups led by Hanson and Zoller performed what they called a loophole-free Bell test [12, 13]. These experiments disproved any hidden-variable theory and established entanglement as a fundamental nonclassical correlation.

Meanwhile, quantum theory began to be incorporated into engineers' toolkits. One of the most transformative inventions based on quantum mechanics is the transistor, the physical implementation of a classical unit of information, the bit. While early electronic computers, such as ENIAC (1945) and Colossus (1943-1945), operated using bulky vacuum tubes and relays, their scalability was severely limited by the unreliability of these components. A notable example is the origin of the term "computer bug", which is based on an actual bug found in a relay. The invention of the transistor in 1948 by Bardeen, Brattain, and Shockley at Bell Laboratories [14] marked a breakthrough, providing a more compact, reliable, and energy-efficient alternative.

As manufacturing techniques evolved, transistors became smaller. Eventually, many of them could be placed on a single silicon chip, and integrated circuits were born. The miniaturization of electronics led to an exponential increase in computing power. In 1965, Moore observed what came to be known as Moore's law [15], the density of transistors per unit area doubled approximately every two years. Remarkably, Moore's Law has held for the most part throughout the years. In 2023, a four trillion-transistor chip was unveiled, with each transistor measuring a mere $5\,\mathrm{nm}$ in its smallest dimension [16]. However, as transistors approach fundamental physical limits at the atomic scale, the pace of Moore's law has begun to decline [17].

Even though computing machines have rapidly advanced, a fundamental rift between classical computation and quantum theory has become increasingly apparent. Mathematically, quantum mechanics is described by matrices and vectors; the simplest quantum system, a two-level system (qubit), is fully described by a 2×2 matrix. However, due to the nature of entanglement, adding another qubit to the system doesn't increase the dimension by two as one would expect from a classical system, but by a factor of 2. This curse of dimensionality makes it practically impossible to simulate larger quantum systems on a classical computer. An entire level of reality remains locked away, unreachable. In 1982, Feynman addressed this problem by calling for a paradigm shift: "To simulate a quantum system, we have to use a quantum system."

In 1985, Deutsch provided the theoretical foundation for quantum computing [18], proving that a universal quantum computer could be constructed from qubits and that such a machine could efficiently simulate any finite physical system with only polynomial overhead, a fundamental improvement over classical computers' exponential resource requirements. This breakthrough extended the Church-Turing principle to quantum systems, establishing quantum computing as a fundamentally new computational paradigm with inherent advantages over classical computation.

The first quantum algorithm to demonstrate an exponential speedup was conceived by Deutsch and Josza in 1992 [19]. Although of no practical use, it proved the existence of problems with quantum advantage. The practical use came only a few years later. In 1995, Peter Shor published his factoring algorithm [20]. With this algorithm, a quantum computer can find the prime factors of an integer with an exponential speedup. This problem was deemed so intractable that a widely used cryptographic scheme (RSA public key cryptography) is based on it. Accordingly, quantum computers can break this encryption. One year later, in 1996, Lov Grover developed his database search algorithm, achieving a quadratic speedup for unstructured search problems [21]. While these algorithms demonstrate the utility of a quantum computer, they did not answer whether it was feasible to build such a device.

Quantum systems are intrinsically fragile, as the core of what makes them quantum mechanical, their coherence, degrades the more they are coupled to the outside world. However, for control, coupling to the outside is unavoidable. This seemingly hopeless paradox gave rise to the field of quantum error correction. In 1995, Shor demonstrated that quantum error correction was possible by showing how to encode a single qubit into a nine-qubit quantum error correcting code, protecting against both bit-flip and phase-flip errors without directly measuring the quantum information [22]. Steane's 1996 seven-qubit error-correcting code quickly followed this breakthrough [23], which represented a more efficient implementation. In the same year, Gottesman introduced stabilizer formalism, a robust framework for constructing codes [24]. The most studied code emerging from this framework is the surface code, which was developed after Kitaev's ideas in 2003 [25].

Another crucial theoretical advance came with the threshold theorem, independently developed by Aharonov and Ben-Or [26] and by Kitaev in 1997 [27], which showed that if error rates are kept below a threshold, arbitrarily reliable quantum computation can be achieved through concatenated error correction.

In 2002, Dowling and Milburn published a paper coining the term "second quantum revolution" [28]. While the first quantum revolution helped us understand how the quantum world works, giving us technologies like transistors and lasers that exploit quantum effects in bulk materials, the second quantum revolution represents our ability to directly create, manipulate, and control individual quantum systems. This transition from passive observation to active engineering of quantum states marked a fundamental shift. Physicists were no longer merely studying quantum mechanics but were actively designing quantum devices that could harness superposition and entanglement for computation and sensing.

This shift manifested across multiple experimental platforms. In 1995, a team around Wineland demonstrated the first quantum logic gate using trapped ions, achieving coherent control over the quantum states of a 9Be+ ion [29]. Brune et al. observed quantum Rabi oscillations between highly excited Rydberg atoms and a microwave cavity the following year [30]. In 1999, Nakamura et al. achieved the same milestone in superconducting circuit architecture [31]. Since then, all these fields have seen massive developments. As the experiments in this thesis are implemented in a superconducting circuit architecture, I will give a more detailed account of the history of this domain.

The field's origins lie in the discovery of superconductivity and the realization that the phase of the superconducting condensate is a macroscopic manifestation of the microscopic order in a superconductor. Josephson derived that the phase difference across a thin insulating barrier separating two superconductors, what we now call a Josephson junction, behaves as if it were the position coordinate of a classical particle moving in a tilted washboard potential.

Building on this insight, Leggett published a theoretical paper in 1980 exploring whether this "phase particle" could exhibit actual macroscopic quantum behavior [32]. In 1985, Martinis, Devoret, and Clark experimentally confirmed this prediction by demonstrating the quantization of the phase particle's energy levels trapped in the tilted washboard potential [33]. The path to superconducting qubits accelerated in 1998 when a group led by Devoret proposed and implemented the Cooper pair box, demonstrating quantum tunneling of individual Cooper pairs [34]. Leveraging an ultra-fast 40 ps pulse generator, Nakamura et al. subsequently achieved the first vacuum Rabi oscillations in a superconducting device [31]. Further progress came with the demonstration of Ramsey fringes in a hybrid charge-phase qubit architecture called quantronium [35], which achieved a $T_2$ of 0.5 µs by exploiting a simultaneous sweet spot for flux and charge noise.

Adapting cavity quantum electrodynamics (QED) principles to these systems enabled a significant breakthrough in coherence times and control techniques [36]. By placing the superconducting qubit between the lines of a coplanar stripline resonator detuned from the qubit's frequency, researchers can suppress unwanted modes, effectively reducing spontaneous decay and extending the qubit's lifetime. When properly tuned, this stripline resonator also enables quantum non-demolition readout of the qubit. Another significant advance was the conception of the transmon [37, 38], a Cooper-pair box with a large shunting capacitance. This design choice has two crucial benefits: while the increased capacitance slightly reduces anharmonicity, it exponentially suppresses charge noise, and the larger dipole moment enables stronger coupling to microwave photons. Another leap in coherence was achieved by transitioning from planar (2D) to three-dimensional (3D) architectures [39], reaching $T_2$ values of 10-20 µs.

As these technical advances accumulated, superconducting quantum computation turned from purely academic research into a serious industrial effort. IBM accelerated its commercial efforts by launching the IBM Q Experience in 2016, making cloud-based quantum computing accessible to researchers worldwide. Google entered the effort in 2014 by hiring the John Martinis group from the University of California, Santa Barbara. In 2019, Google claimed the significant milestone of quantum supremacy, using their 53-qubit transmon-based Sycamore processor [40]. IBM responded by unveiling their successively larger transmon processors: the 127-qubit Eagle in 2021, the 433-qubit Osprey in 2022, and announcing plans for the 1000+ qubit Condor processor. However, as the field races toward ever-larger qubit counts, the fundamental challenge of error correction looms large. While surface codes show theoretical promise [41, 42], current implementations require approximately 100-1000 physical qubits to create a single logical qubit. This unfavorable ratio means today's machines can, in principle, barely sustain a few logical qubits, severely constraining practical quantum advantage for meaningful algorithms. Until this ratio improves dramatically through higher qubit fidelities and more efficient error-correction schemes, the gap between demonstrating larger and larger quantum systems and achieving practical quantum computing applications remains enormous.

This challenge motivated the search for alternative approaches. Bosonic quantum computing emerged as a compelling alternative, where quantum information is encoded in the continuous degrees of freedom of a quantum harmonic oscillator rather than in discrete two-level systems. In their seminal 2001 paper, Gottesmann, Kitaev, and Preskill demonstrated that discrete quantum information can be encoded in the infinite-dimensional Hilbert space of an oscillator, correcting against displacements in position and momentum [43]. With this work, they demonstrated that oscillators are not just auxiliary modes for qubit control, but can store quantum information on their own. Beyond quantum computation, continuous-variable systems have proven to be valuable for quantum communication, sensing, and fundamental tests of quantum mechanics [44].

Bosonic circuit quantum electrodynamics emerged as the natural platform for realizing and pursuing these ideas. Superconducting microwave cavities exhibit remarkable coherence, routinely exceeding milliseconds [45] while also displaying a strong noise bias, with photon loss dominating over the significantly smaller pure dephasing rate.

Over time, multiple encoding strategies have emerged. The GKP code encodes quantum information on a grid in phase space, enabling correction of arbitrary displacements. [43, 46]. Cat codes encode information in the superposition of coherent states. They exhibit the interesting property that their bit-flip rate is exponentially suppressed with increasing coherent state size, whereas the dephasing rate increases linearly [47]. Binomial codes encode quantum information in the superposition of specific photon number states chosen to suppress specific errors [48]. Recently, the dual-rail encoding has gained attention. Quantum information is encoded across two oscillators, with photon loss manifesting as erasure errors, with the location and time of occurrence precisely known and correctable with minimal overhead [49–51].

Experimental progress has validated this approach through several groundbreaking results. Ofek et al. ran the first experiment to achieve error correction beyond the break-even point. They used a four-legged cat code that achieved a $2\times$ lifetime improvement over the uncorrected qubit [52]. Sivak et al. combined the Gottesman-Kitaev-Preskill (GKP) encoding with real-time neural network error correction to surpass break-even by a factor of $2.27$ [53]. In the same year, Ni et al. demonstrate a $1.2\times$ lifetime gain using a binomial encoding [48].

While recent experiments in bosonic circuit QED have demonstrated break-even error correction with various encoding schemes, realizing practical quantum computation requires both improved error-correction strategies and the ability to generate multi-mode entanglement. This thesis contributes to both directions through two experiments. The first demonstrates how phase space compression can protect the quantum interference features of cat states, and the second shows the first creation of macroscopic tripartite entanglement in the form of a GHZ-cat and W-cat state in bosonic cQED.

## 1.2 Thesis outline

The overarching theme of my thesis is the development of hardware-aware quantum state engineering techniques that exploit the extensive Hilbert space of bosonic systems to create more robust quantum states and enable efficient multipartite entanglement generation. These techniques look at the fundamental hardware limitations and capabilities and leverage them to achieve in situ protection against the dominant error mechanism and efficient multimode control.

I start my thesis in chapter 2 by establishing the theoretical foundations of bosonic circuit quantum electrodynamics, beginning with the quantum harmonic oscillator and its phase space representations. I will introduce the transmon as the nonlinear element and examine how dispersive coupling between transmons and oscillators enables both universal control and tomography over the quantum harmonic oscillator. Furthermore, I will discuss different control techniques and their respective interaction times. This chapter provides the framework to understand how bosonic modes serve as versatile platforms for storing and manipulating quantum information.

In chapter 3, I give a detailed discussion of the echo conditional displacement gate (ECD), the primary tool used in the weak dispersive coupling regime, where the experiments in this thesis are performed. I will detail the experimental implementation of the ECD gate and the displaced frame formalism, a crucial tool for enabling Hamiltonian simulations in the weakly dispersive coupling regime. Finally, I will cover different calibration protocols used to characterize the Hamiltonian and the experimental implementation of our tomography method, the characteristic function. These techniques provide the foundation for the two major experiments presented in subsequent chapters.

In chapter 4, I present the first major experiment of my thesis. We protected the fragile interference features of cat states through deterministic phase space compression. Viewing the effect of photon loss through the characteristic function lens transforms its action into a Gaussian low-pass filter. At the same time, the coherence features of cat states appear as high-frequency elements in this reciprocal phase space picture. I will demonstrate how to create compressed cat states deterministically and how this compression can push the interference features under the Gaussian filter, providing protection by design. Using this method, we present experimental results demonstrating a five-fold enhancement in the lifetime of the quantum interference features against photon loss. This experiment demonstrates the importance of understanding the hardware's dominant error mechanism in designing intrinsically robust codewords.

In chapter 5, I demonstrate and leverage the excellent multimode control capabilities of the ECD gate to implement the first tripartite entangled cat in a bosonic cQED architecture. For this, I design a one-to-all coupling architecture in which three bosonic modes are simultaneously controlled by a single transmon, enabling parallelized state preparation and direct joint-observable measurements. Besides preliminary data showing the implementation of a Greenberger-Horne-Zeilinger-cat (GHZ-cat) state, I also developed a protocol to create a W-cat state. This includes the novel Uneven Echo Conditional Displacement (UECD) transfer, allowing conditional displacements in the qubits g-f subspace. Finally, we develop and experimentally verify an efficient tomography method for our tripartite entangled cat states, mapping three-qubit Pauli operators to points in the 8D characteristic function. This experiment opens the door to a multitude of interesting follow-up experiments, including exploring the different entanglement structures of GHZ-cat and W-cat states, and designing and implementing more robust multimode codewords.

# Chapter 2

# Foundations of bosonic cQED

This Chapter serves as an introduction to the fundamental physics of bosonic cQED. Given that there exist excellent review articles [54, 55], books [56, 57], and Ph.D theses [58–61] that cover the physics of superconducting circuits and bosonic cQED in depth, I will only briefly go over the necessary fundamentals required to understand this thesis.

The logical progression of this Chapter moves from building blocks to coupling to operational principles. In section 2.1, I begin with the principal element of bosonic cQED, the quantum harmonic oscillator (QHO), followed by a discussion of the non-linear element, the transmon, in section 2.2. Section 2.3 provides details on how these elements are coupled in the dispersive regime, while section 2.4 demonstrates how the dispersive regime facilitates readout and a multitude of control techniques.

## 2.1 Quantum harmonic oscillator

The harmonic oscillator represents one of the most fundamental systems in all of physics, serving as both an introductory model and a powerful framework for understanding complex quantum phenomena. The Hamiltonian of a classical harmonic oscillator in dimensionless units takes the form:

$$H = p^2 + q^2. \tag{2.1}$$

Here, $p$ and $q$ are any canonical conjugate variables describing a single degree of freedom, such as momentum and position for a mechanical system or charge and flux for an electromagnetic system. The relevance of the harmonic oscillator becomes apparent when we realize that many systems around a potential minimum can be approximated as harmonic oscillators. Taylor expanding around the minimum and keeping only up to second-order terms naturally gives rise to the harmonic oscillator potential.

In circuit quantum electrodynamics, the harmonic oscillator manifests as an LC circuit, where energy oscillates between the electric field stored in a capacitor and the magnetic field stored in an inductor. The corresponding circuit diagram is shown in Fig. 2.1 (a). When a superconducting circuit is cooled to cryogenic temperatures and operated with appropriate energy scales, the circuit begins to exhibit quantum mechanical behavior. This transition is captured mathematically by following Dirac's canonical quantization approach, where dynamical variables are represented as operators that obey the Heisenberg uncertainty principle. For example, the canonical variables in Equation 2.1, $p$ and $q$ are promoted to operators obeying the commutation relation $[\boldsymbol{q}, \boldsymbol{p}] = i\hbar$. Note that throughout this thesis, I will indicate operators in bold.

The Hamiltonian of a quantum LC circuit can be written as:

$$\boldsymbol{H} = \frac{\mathbf{Q}^2}{2C} + \frac{\boldsymbol{\Phi}^2}{2L} \tag{2.2}$$

where the charge $\mathbf{Q}$ and the magnetic flux $\boldsymbol{\Phi}$ are canonical conjugate variables, and C and L are the capacitance and inductance of the circuit, determined by its geometry. As a consequence of quantization, the canonical conjugate variables obey the commutator relations $[\boldsymbol{\Phi}, \boldsymbol{Q}] = i\hbar$. From here, it is instructive to express the Hamiltonian in terms of dimensionless quantities. We express the total flux in terms of the reduced flux quantum $\phi_0 = \hbar/2e$ as $\boldsymbol{\Phi} = \phi_0 \boldsymbol{\varphi}$. Similarly, we decompose the charge operator $\boldsymbol{Q}$ in terms of the number of charges. Considering that charges in a superconductor come in Cooper pairs, we write $\boldsymbol{Q} = 2e\boldsymbol{n}$. Using this approach, the Hamiltonian takes the form:

$$\boldsymbol{H} = 4E_C \boldsymbol{n}^2 + \frac{E_L}{2}\boldsymbol{\varphi}^2 \tag{2.3}$$

where $E_C = \frac{e^2}{2C}$ and $E_L = \frac{\phi_0^2}{L}$. To diagonalize this Hamiltonian, we express $\boldsymbol{n}$ and $\boldsymbol{\varphi}$ through ladder operators.

$$\boldsymbol{\varphi} = \varphi^{ZPF}\left(\boldsymbol{a}^\dagger + \boldsymbol{a}\right), \quad \boldsymbol{n} = \tfrac{i}{2} n^{ZPF}\left(\boldsymbol{a}^\dagger - \boldsymbol{a}\right) \tag{2.4}$$

where $\varphi^{ZPF} = \left(\frac{2E_C}{E_L}\right)^{\frac{1}{4}}$ and $n^{ZPF} = \left(\frac{E_L}{2E_C}\right)^{\frac{1}{4}}$ are the zero point fluctuations of the flux and charge of the oscillator and $[\boldsymbol{a}, \boldsymbol{a}^\dagger] = 1$. These scales establish the fundamental vacuum fluctuation levels.

The newly introduced operators $\boldsymbol{a}^\dagger$ and $\boldsymbol{a}$ allow us to rewrite the Hamiltonian of the QHO:

$$\boldsymbol{H} = \hbar\omega\left(\boldsymbol{a}^\dagger \boldsymbol{a} + \frac{1}{2}\right). \tag{2.5}$$

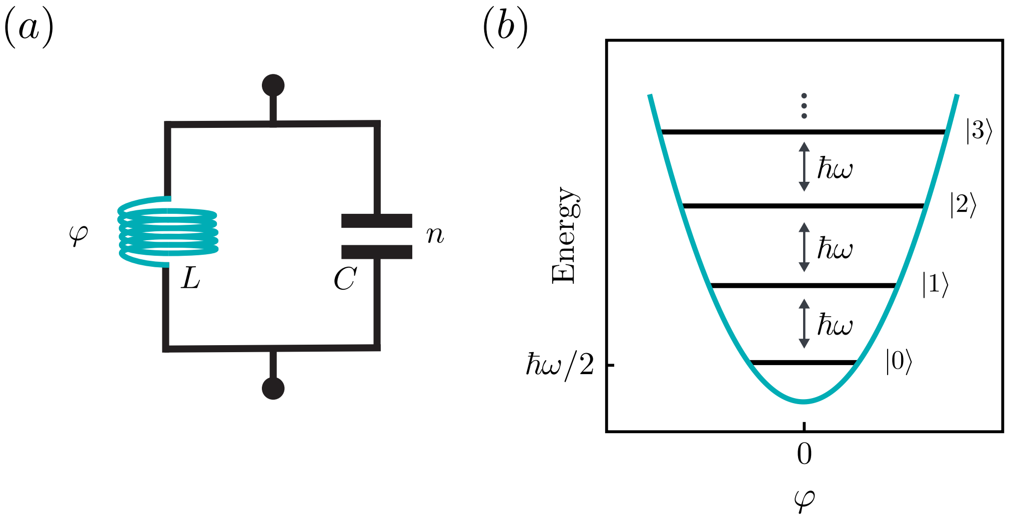

Figure 2.1: **LC circuit schematic and QHO spectrum.** (a) Lumped element representation of an LC circuit. The inductor stores energy in its magnetic field, while the capacitor stores energy in its electric field. Energy oscillates between these two components at the resonant frequency $\omega = \frac{1}{\sqrt{LC}}$. (b) Energy spectrum of the quantum harmonic oscillator showing the discrete, equally-spaced energy levels $E_n = \hbar\omega(n + \frac{1}{2})$. The ground state has zero-point energy $\hbar\omega/2$, and each excited state is separated by exactly $\hbar\omega$, creating the characteristic "ladder" structure.

with $\omega = \frac{1}{\sqrt{LC}} = \sqrt{8E_C E_L}/\hbar$. The spectrum of the eigenvalue equation $\boldsymbol{H}|n\rangle = E_n|n\rangle = \hbar\omega(n+\frac{1}{2})|n\rangle$, shown in Fig. 2.1(b), exhibits two fundamental characteristics. First, the spacing between energy levels is uniform by exactly $\hbar\omega$, lending the analogy to the rungs of a ladder. Second, the ground state ($n = 0$) has a vacuum energy of $\hbar\omega/2$.

The ladder operators $\boldsymbol{a}$ and $\boldsymbol{a}^\dagger$ are named after their actions on the eigenstates. The annihilation operator $\boldsymbol{a}$ moves eigenstates one rung down while the creation operator $\boldsymbol{a}^\dagger$ moves them one rung up. For many students, introducing ladder operators initially appears to sacrifice physical intuition for the sake of mathematical convenience. This misunderstanding stems from focusing too narrowly on specific physical quantities, such as electron motion in circuits or magnetic flux strength, rather than recognizing the more fundamental and straightforward description they provide: how energy is stored and transformed within the system. By inverting Equation 2.4, we can relate these operators to the physical variables of flux and charge:

$$\boldsymbol{a} = \varphi^{ZPF}\boldsymbol{\varphi} + \tfrac{i}{2}n^{ZPF}\boldsymbol{n}, \quad \boldsymbol{a}^\dagger = \varphi^{ZPF}\boldsymbol{\varphi} - \tfrac{i}{2}n^{ZPF}\boldsymbol{n} \tag{2.6}$$

This formulation reveals that the ladder operators are complex-valued. The quadrature operators

$$\boldsymbol{X} = \tfrac{1}{2}\left(\boldsymbol{a} + \boldsymbol{a}^{\dagger}\right), \quad \boldsymbol{P} = \tfrac{i}{2}\left(\boldsymbol{a}^{\dagger} - \boldsymbol{a}\right) \tag{2.7}$$

provide a natural way to represent the real and imaginary parts of the ladder operators, creating quantum analogs of classical position and momentum coordinates. For our quantum LC circuit, these quadratures operators are, up to the vacuum fluctuations, equivalent to flux and charge number, see Equation 2.4. I want to point out that the pre-factor in the definition of the quadrature operators varies between sources and is either $1/2$ or $1/\sqrt{2}$.

While every classical harmonic oscillator state corresponds to a either a single point or a distribution of points in phase space $(x, p)$, every QHO state can be described by a quasi-probability distribution over the quadrature operators $f(\boldsymbol{X}, \boldsymbol{P})$. This phase space representation bridges classical intuition with quantum mechanics, providing powerful tools for visualizing and characterizing quantum states in experimental implementations.

### 2.1.1 Quantum mechanics in phase space

Knowledge about the density matrix means full knowledge of the quantum state. Yet, density matrices of complex states living in a large Hilbert space are difficult to grasp. Is there a quasi-probability distribution that is isomorphic to the density matrix, captures intuition built from classical phase space, and is also experimentally accessible? The Wigner function is just that. It allows intuitive visualization that resembles classical phase space and is accessible in the lab. However, later in this thesis, we will find that measuring the Wigner function is not feasible in every cQED architecture. In these cases, the characteristic function, a relative of the Wigner function, is the tool of choice. Following, I will introduce both representations and connect them to experimentally accessible observables.

#### Wigner function

In 1932, Wigner found a mapping between the density matrix $\rho$ and a quasi-probability distribution that is now known as the Wigner function [62], as defined below:

$$W(x,p) = \frac{1}{\pi}\int_{-\infty}^{\infty} \left\langle x - \frac{y}{2}\right| \boldsymbol{\rho} \left| x + \frac{y}{2}\right\rangle e^{i2py} dy \tag{2.8}$$

The Wigner function formalism provides a complete alternative formulation of quantum mechanics.

Unlike a traditional probability distribution, the Wigner function takes negative values, lending it the name quasi-probability distribution. It has been proven that these negative features are witnesses of non-classical behavior [63, 64]. Another fundamental property of the Wigner function is that we can obtain the marginal probability distributions of position and momentum by integrating over the complementary variable:

$$P(x) = \langle x | \boldsymbol{\rho} | x \rangle = \int_{-\infty}^{\infty} W(x,p)dp \tag{2.9}$$

$$P(p) = \langle p | \boldsymbol{\rho} | p \rangle = \int_{-\infty}^{\infty} W(x,p)dx \tag{2.10}$$

By inverting Equation 2.8, we can construct the density matrix in either the position or momentum basis from the Wigner function, as shown here in the position basis.

$$\left\langle x - \frac{y}{2} \middle| \boldsymbol{\rho} \middle| x + \frac{y}{2} \right\rangle = \int_{-\infty}^{\infty} W(x,p)e^{-i2py}dp \tag{2.11}$$

For experimental purposes, the Wigner function can be directly related to a measurable quantity, the photon number parity operator $\boldsymbol{\mathcal{P}} = e^{i\pi \boldsymbol{a}^\dagger \boldsymbol{a}}$. The complete derivation can be found in [56].

$$W(\alpha) = \frac{1}{\pi}\int_{-\infty}^{\infty} \left\langle \frac{y}{2} \middle| \boldsymbol{D}(\alpha)^\dagger \boldsymbol{\rho} \boldsymbol{D}(\alpha) \boldsymbol{\mathcal{P}} \middle| \frac{y}{2} \right\rangle dy = \frac{2}{\pi}\mathrm{Tr}[\boldsymbol{D}(\alpha)^\dagger \boldsymbol{\rho} \boldsymbol{D}(\alpha) \boldsymbol{\mathcal{P}}] \tag{2.12}$$

where $\alpha = x + ip$ and $\boldsymbol{D}(\alpha)$ is the displacement operator as defined in the next section.

In the next Chapter, we will discuss how cQED architectures allow measurement of the parity operator $\boldsymbol{\mathcal{P}}$ and, as such, direct experimental access to the Wigner function.

### Characteristic function

The characteristic function is another representation of the density matrix in phase space. It is related to the Wigner function through a double Fourier transform and is thus also referred to as reciprocal phase-space. As such, it is less intuitive than the Wigner function, but it becomes experimentally invaluable in regimes where accessing the Wigner function is challenging.

$$W(\alpha) = \frac{1}{\pi^2}\int C(\nu) e^{\alpha\nu^* - \alpha^*\nu} d^2\nu \tag{2.13}$$

Alternatively, the characteristic function is defined as the expectation value of the displacement operator. For a state $|\psi\rangle$, this takes the form:

$$\mathcal{C}(\nu) = \langle \psi | \boldsymbol{D}(\nu) | \psi \rangle \tag{2.14}$$

with the displacement operator itself defined as

$$\boldsymbol{D}(\nu) = e^{\nu \boldsymbol{a}^\dagger - \nu^* \boldsymbol{a}} = e^{-i2\mathrm{Re}(\nu)\boldsymbol{P} + i2\mathrm{Im}(\nu)\boldsymbol{X}} \tag{2.15}$$

The displacement operator translates states in phase-space (Wigner function representation) by Re$(\nu)$ along the $\boldsymbol{X}$ axis and Im$(\nu)$ around the $\boldsymbol{P}$ axis. Hence, for a pure state, the characteristic function maps out the overlap of the state with itself after being displaced by $\nu$.

Unlike the Wigner function, the characteristic function is complex-valued and satisfies $\mathcal{C}(-\nu) = \mathcal{C}^*(\nu)$. It follows that the characteristic function is real for states that follow the symmetry $\mathcal{C}(\nu) = \mathcal{C}(-\nu)$. An imaginary part shows up when this symmetry is broken.

All experiments in this thesis are performed in a regime where the coupling between qubit and cavity is small compared to the qubit lifetimes. As a result, the Wigner function is not accessible, and the characteristic function is our tool of choice. The protocol to directly measure the real or imaginary part of the characteristic function is detailed in Section 3.3.2.

In the following section, I will examine several commonly encountered quantum harmonic oscillator states and discuss their representations in both the Wigner and characteristic functions to build an intuitive understanding of how to read these phase-space distributions.

### 2.1.2 States of the QHO

The utility of the QHO stems from its rich, infinite-dimensional state space, which accommodates diverse quantum states with distinctive properties. Here, I will introduce some of the most common QHO states, which are of importance for this thesis. In particular, I will discuss Fock states (energy eigenstates), coherent states (quasi-classical states), squeezed states (which demonstrate reduced uncertainty in one quadrature), and cat states (superpositions of coherent states).

#### Fock states

Fock states, or photon number states, occupy a privileged position as energy eigenstates of the quantum harmonic oscillator $\boldsymbol{a}^\dagger \boldsymbol{a} |n\rangle = \boldsymbol{n} |n\rangle = n |n\rangle$. They form a complete orthonormal basis that is often used to represent any arbitrary quantum state. Their discrete nature allows for effective truncation of the infinite-dimensional Hilbert space to a computationally manageable subspace, making them ideal for numerical simulations. Furthermore, Fock states exhibit trivial time evolution, simply acquiring a phase factor $e^{-iE_n t/\hbar}$, significantly simplifying dynamic calculations.

In phase space, Fock states possess a well-defined energy but an undefined phase, manifesting as rotationally symmetric distributions around the origin. Fig. 2.2 (a) depicts the Wigner and characteristic function of $|n = 2\rangle$. Their shapes are described by Laguerre polynomials under

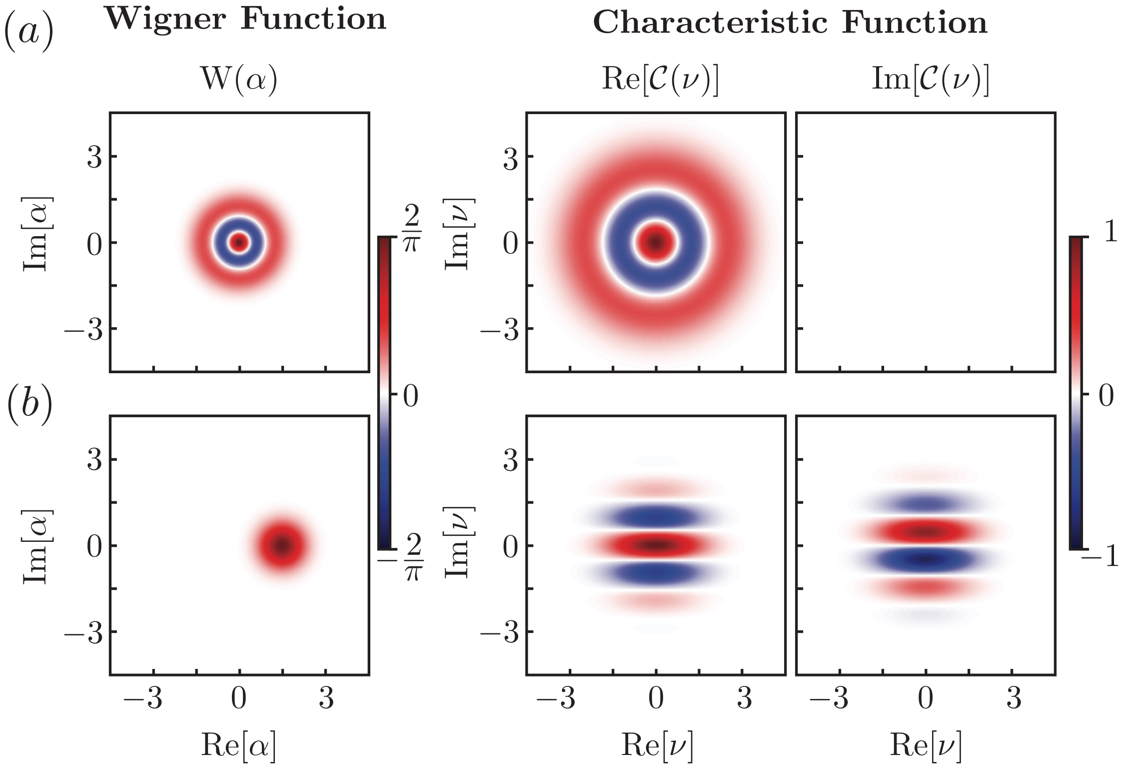

Figure 2.2: **Wigner and characteristic function of a Fock and coherent state.** (a) Depiction of $|n=2\rangle$. In both functions, Fock states appear as Laguerre polynomials under a Gaussian envelope. Fock states are states with well-defined energy and complete phase uncertainty, resulting in a doughnut-like shape. (b) Depiction of $|\alpha=1.5\rangle$. In the Wigner function, coherent states appear as a Gaussian distribution with minimal uncertainty. Their resemblance to states of the classical HO earns them the alternative name of quasi-classical states. In the characteristic function, a coherent state appears as a Gaussian modulated by a cosine in the real part and a sine in the imaginary part. The coherent state size determines the oscillation frequency, while the phase determines the angle of the oscillations. The full phase information is encoded in the imaginary part.

a Gaussian envelope. Fock states are inherently non-classical, with negativity in their Wigner function. However, it is essential to note that, unlike in the Wigner representation, negativity in the characteristic function does not indicate quantum features.

### Coherent states

Coherent states are eigenstates of the annihilation operator $\boldsymbol{a}$, with $\boldsymbol{a}\,|\alpha\rangle = \alpha\,|\alpha\rangle$. Their Wigner function representation is a Gaussian distribution that minimizes the uncertainty relationship between position and momentum with equal uncertainty in both quadratures as shown in Fig.

2.2 (b). Furthermore, their time evolution follows classical trajectories, oscillating in a circle while maintaining their Gaussian shape, which is why they are also known as quasi-classical states.

In the Fock space basis, coherent states take the form:

$$|\alpha\rangle = e^{-\frac{|\alpha|^2}{2}} \sum_{n=0}^{\infty} \frac{\alpha^n}{\sqrt{n!}} |n\rangle \tag{2.16}$$

From this, we find the overlap of two coherent states as $\langle\beta|\alpha\rangle = e^{-\frac{|\alpha|^2}{2}-\frac{|\beta|^2}{2}+\beta^*\alpha}$. The Fock state population of a coherent state follows a Poisson distribution $P(n) = e^{-\langle \boldsymbol{n}\rangle}\frac{\langle \boldsymbol{n}\rangle^n}{n!}$ with average photon number $\langle \boldsymbol{n}\rangle = |\alpha|^2$ and variance $|\alpha|^2$.

Applying a displacement operator to a coherent state displaces it and generates a geometric phase:

$$\boldsymbol{D}(\nu)\,|\alpha\rangle = e^{\alpha\nu^*-\alpha^*\nu}\,|\alpha+\nu\rangle \tag{2.17}$$

The characteristic function representation of coherent states follows by combining this relation with the overlap formula between two coherent states:

$$C_{|\alpha\rangle}(\nu) = \langle\alpha|\boldsymbol{D}(\nu)|\alpha\rangle = e^{-\frac{|\nu|^2}{2}} e^{\alpha^*\nu-\nu^*\alpha} \tag{2.18}$$

Finally, using $\alpha = a_1 + ia_2$, $\nu = v_1 + iv_2$, we can express this in terms of real and imaginary components:

$$\begin{aligned}\mathrm{Re}(C(\nu)) &= e^{-\frac{|\nu|^2}{2}}\cos(2a_1v_2 - 2a_2v_1)\\ \mathrm{Im}(C(\nu)) &= e^{-\frac{|\nu|^2}{2}}\sin(2a_1v_2 - 2a_2v_1)\end{aligned}$$

The characteristic function of a coherent state $|\alpha = 1.5\rangle$ is plotted in Fig. 2.2 (b). A key observation is that the amplitude of the coherent state is encoded in the oscillation frequency of the fringes, which appear perpendicular to the state's position in phase space. One can only recover the complete phase information from the imaginary part of the characteristic function. As a bridge, if your left foot stands on the first positive oscillation and your right on the first negative, the position of the coherent state in the Wigner function is in line of sight.

### Squeezed states

Squeezed states represent another fundamental class of non-classical states where uncertainty is redistributed between conjugate variables. While coherent states have equal uncertainty in both quadratures, squeezed states reduce uncertainty in one quadrature at the expense of increased uncertainty in the other, still satisfying the Heisenberg uncertainty principle. Mathematically, squeezed states are generated by applying the squeezing operator:

$$\boldsymbol{S}(z) = e^{\frac{1}{2}(\xi^* \boldsymbol{a}^2 - \xi \boldsymbol{a}^{\dagger 2})} \tag{2.19}$$

where I assume for simplicity that $\xi$ is real. Applying this operator to a vacuum yields a squeezed vacuum state, with the defining property that the standard deviation in the X quadrature is reduced

$$\Delta \boldsymbol{X} = \frac{1}{2} e^{-\xi} \tag{2.20}$$

while the P quadrature is increased

$$\Delta \boldsymbol{P} = \frac{1}{2} e^{\xi} \tag{2.21}$$

It is common practice to quote the squeezing in dB, which is found from the squeezing parameter $\xi$ as $20\log_{10}\left(|e^{\xi}|\right)$.

A general squeezed coherent state is given by:

$$|\alpha, \xi\rangle = \boldsymbol{D}(\alpha)\boldsymbol{S}(\xi)|0\rangle \tag{2.22}$$

In phase space, these states appear as elliptical Gaussian distributions rather than circular ones. Squeezed states have practical applications in quantum communication and quantum metrology, where, e.g., they are used for gravitational wave detection [65, 66]. The Wigner and characteristic functions of a squeezed vacuum state are depicted in Fig. 2.3(a).

### Cat states

Cat states are superpositions of coherent states with opposite phases, named after Schrödinger's cat thought experiment.

$$|\psi_{\text{cat}}\rangle = \mathcal{N}(|\alpha\rangle + e^{i\phi}| - \alpha\rangle) \tag{2.23}$$

Here $\mathcal{N}$ is a normalization constant, and $\phi$ determines the type of cat state: $\phi = 0$ gives an even cat state containing only even Fock states, while $\phi = \pi$ gives an odd cat state with only odd Fock states. The distinct parity of even and odd cat states can be used to detect flips between the two, making them a promising candidate for quantum error correction.

The defining property of a cat is that it is a superposition of macroscopic coherent states. In our system, they are a superposition of electromagnetic fields on a geometric scale of millimeters. In the Wigner function, this quantum behavior manifests in the fringes between the two Gaussian peaks. These coherent fringes are incredibly fragile and quickly vanish due to

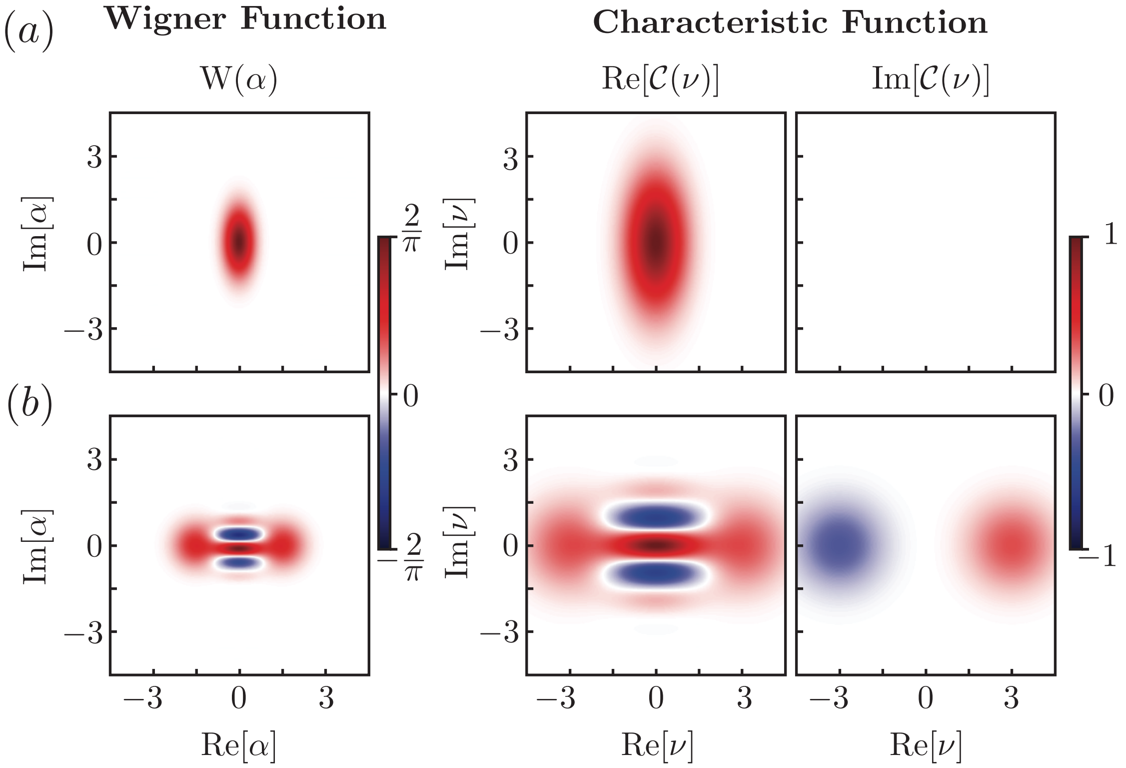

Figure 2.3: **Wigner and characteristic function of a squeezed and cat state.** (a) Depiction of $|\alpha = 0, \xi = 0.4\rangle$. Both representations exhibit elliptical Gaussian distributions, reflecting the redistribution of quantum uncertainty between conjugate quadratures. The variance of one quadrature is reduced with a corresponding amplification in the other quadrature. A phase would show up as a rotation of the Gaussian distribution. (b) Depiction of $\mathcal{N}\left(|\alpha\rangle + e^{i\pi/4}\,|-\alpha\rangle\right)$ with $\alpha = 1.5$. While Wigner and characteristic functions appear visually similar, they encode information in a complementary manner. In the Wigner function, the size is encoded in the location of the blobs, while the interference appears as fringes between the blobs. A relative phase between the coherent states appears as a phase offset in the oscillating fringes. The characteristic function reverses this encoding. The size is encoded in the fringes, while the coherence appears as blobs. A relative phase transfers the blobs between real and imaginary parts of the characteristic function.

decoherence. They are also the reason why cat states are valuable for metrology and tests of fundamental quantum mechanics [67].

Fig. 2.3 (b) shows a cat state with $\phi = \pi/4$. This particular phase is chosen to demonstrate the impact a phase has in the different representations. At first glance, the Wigner function and the real part of the characteristic function appear similar. However, the information is encoded in reverse. The cat's size is encoded in the blobs in Wigner and the fringes in the characteristic

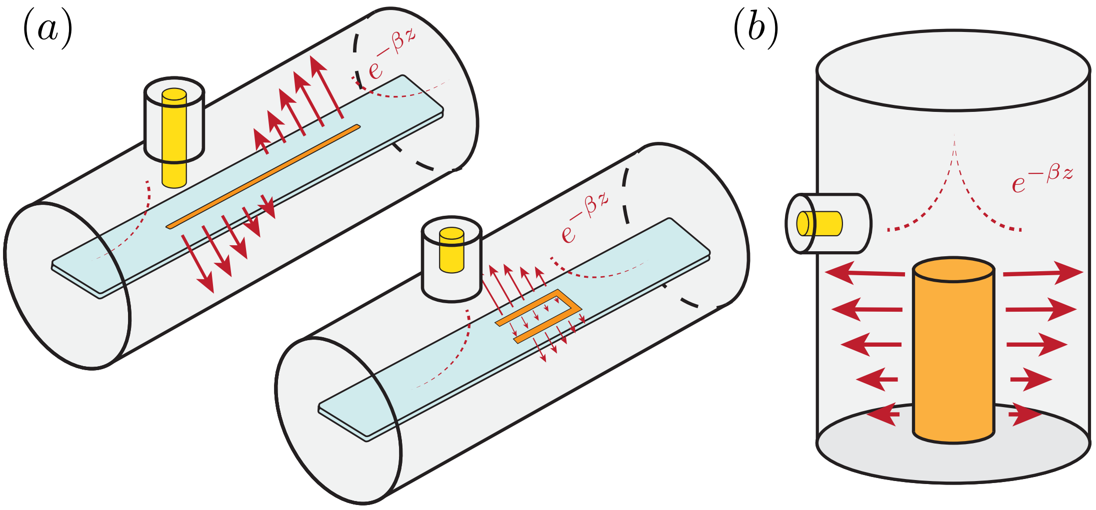

Figure 2.4: **Implementations of LC resonators.** (a) Sputtered thin-film stripline and hairpin resonators on a sapphire substrate. The chips are housed in a waveguide made of high-purity aluminum, featuring a sufficiently high cutoff frequency that prevents the resonator's field from spreading. Stripline resonators are often used as a readout resonator and are strongly coupled through a pin to a transmission line. The geometry of Hairpin resonators minimizes field loss by diluting the field in lossy interfaces, allowing $Q_{\text{int}}$ to exceed $3 \times 10^7$. When used as a storage mode, they are weakly coupled to the outside. (b) 3D Coaxial stubline cavity made out of a single piece of high-purity aluminum. Most of the field is stored in vacuum, and the elimination of seams allows us to routinely achieve $Q_{\text{int}}$ above $\sim 10^8$. Like the Hairpin resonator, they are typically used as a storage mode and are thus weakly coupled to the control line.

function.

On the other hand, the coherence and phase are encoded in the fringes in Wigner and the blobs in the characteristic function. A critical observation in the context of this thesis is that the quantum features appear as high-frequency components in the reciprocal phase space. This insight is used in chapter 4 to protect the coherence features of cat states through compression in reciprocal phase space.

### 2.1.3 Physical implementation

Quantum LC oscillators require two fundamental components: an inductive element that stores energy in magnetic fields from moving charges, and a capacitive element that stores energy in electric fields from static charges on opposing surfaces. To exhibit quantum mechanical behavior, these elements must be fabricated from superconducting materials and cooled to temperatures where the system predominantly resides in its ground state $|0\rangle$.

Both thermal and material considerations constrain the frequency range in which we can operate. The lower bound is set by commercially available dilution refrigerators operating at approximately $T = 10\,\mathrm{mK}$. Unwanted thermal excitation follows the Boltzmann distribution $e^{-\frac{\hbar\omega}{k_B T}}$. To suppress thermal excitations, the oscillator frequency must be sufficiently high (typically $\sim 4\,\mathrm{GHz}$). Material properties set the upper bound. The superconducting gap of aluminum is at $1.2\,\mathrm{K}$ corresponding to $\sim 40\,\mathrm{GHz}$. To ensure that we do not break the Cooper pairs and create lossy quasi-particles, we have to operate well below that point. An additional, though not fundamental, constraint is the availability of affordable control electronics, which sets the effective frequency range for our experiments between 4-8 GHz.

The quality of a resonator is quantified by its $Q$-factor, $Q = \omega T_1$, where $\omega$ is the resonator's frequency and $T_1$ is the characteristic energy decay time. This $Q$-factor comprises two contributions:

$$\frac{1}{Q} = \frac{1}{Q_{\text{ext}}} + \frac{1}{Q_{\text{int}}} \tag{2.24}$$

The intentional coupling to control lines is quantified by $Q_{\text{ext}}$, while $Q_{\text{int}}$ accounts for all dissipative losses to the environment. Naturally, for a storage element, we want the $Q$-factor to be as large as possible. At the same time, for a readout element, we artificially limit the $Q$-factor by engineering a small $Q_{\text{ext}}$.

To achieve a high $Q_{\text{int}}$, we have to ensure that the electrical field of a mode is stored with minimal losses. For that, vacuum is ideal, bulk material a little worse, and the interfaces and seams are bad [59]. With this in mind, we can achieve high $Q_{\text{int}}$ through material choice and engineering the mode structure, for example, by diluting the field stored in interfaces and placing the resonators in waveguides with appropriate cutoff frequencies to minimize participation in seams and suppress unwanted couplings to other modes.

The design of the resonator depends on its role as either a readout or a storage device. For readout, simple stripline $\lambda/2$ resonators, as shown at the top of Fig. 2.4 (a), are used. Their $Q_{\text{int}}$ is currently limited to $Q_{\text{int}} \approx 10^6$ [68]. However, their overall Q-factor is artificially limited by strong external coupling to a pin, resulting in $Q_{\text{ext}} \approx 10^4$ to achieve readout in hundreds of nanoseconds.

For storage cavities, we either use coaxial stubline cavities or on-chip tantalum hairpin resonators. 3D architectures, such as the coaxial stubline $\lambda/4$ resonator shown in Fig. 2.4 (b), are manufactured from a single piece of high-purity aluminum, eliminating seams and retaining most of the field in a lossless vacuum. As a result, they consistently achieve $Q_{\text{int}} \approx 10^8$ [59]. While these 3D architectures have starred in many groundbreaking cQED experiments, they are bulky and difficult to scale for multimode experiments. Recent advancements in fabrication techniques, better understanding of relaxation mechanisms, and material properties have led to the design of tantalum on-chip hairpin $\lambda/2$ resonators, achieving $Q_{\text{int}} \approx 3 \times 10^7$ [69]. A schematic is shown at the bottom of Fig. 2.4 (a).

In this thesis, I utilize a coaxial stubline cavity for my first single-mode experiment in Chapter 4. At the same time, the more compact tantalum hairpin resonators are a natural choice for the multimode experiment in Chapter 5.

### 2.1.4 Loss mechanisms

Quantum systems are inherently fragile and susceptible to environmental perturbations. Despite careful fabrication of resonators and their surrounding environment, interactions with external degrees of freedom are unavoidable. These interactions manifest through two distinct decoherence mechanisms: energy relaxation characterized by the time constant $T_1$, and pure dephasing characterized by $T_\phi$. The total dephasing time $T_2$, which quantifies the combined effect of decay-induced and pure dephasing, is given by

$$\frac{1}{T_2} = \frac{1}{2T_1} + \frac{1}{T_\phi} \tag{2.25}$$

In superconducting resonators, energy loss arises from multiple mechanisms, including two-level systems (TLS), radiative losses, magnetic vortices, and quasiparticles generated by stray infrared radiation and microwave-induced pair-breaking [70]. In contrast, pure dephasing unrelated to coupled nonlinear modes is essentially negligible [71]. This absence of intrinsic dephasing stems from the exceptional frequency stability of resonators, whose resonant frequency depends on the macroscopic circuit parameters $L$ and $C$.

This intrinsic noise bias $T_\phi \gg T_1$ is extremely valuable for quantum error correction, particularly for bosonic codes such as the Gottesman-Kitaev-Preskill (GKP) [43] and 4-legged cat codes [52]. The dual-rail encoding [49] leverages this bias more directly by encoding the logical qubit in only the first two levels of the resonator, sacrificing the large Hilbert space to exploit the favorable noise structure fully.

To model these decoherence processes mathematically, we employ the Lindblad formalism [72], which provides the necessary framework for describing non-unitary evolution in open quantum systems. The general Lindbladian takes the form

$$\mathcal{L}[\rho] = \sum_k \gamma_k \left( \boldsymbol{L}_k \rho \boldsymbol{L}_k^\dagger - \frac{1}{2}\{\boldsymbol{L}_k^\dagger \boldsymbol{L}_k, \rho\} \right) \tag{2.26}$$

where $\boldsymbol{L}_k$ are the jump operators and $\gamma_k$ are the corresponding rates.

For photon loss, the relevant jump operator is $\boldsymbol{L} = \boldsymbol{a}$ with rate $\gamma = \kappa$. Under these dynamics, a coherent state $|\alpha\rangle$ evolves as $|\alpha(t)\rangle = |\alpha e^{-\kappa t/2}\rangle$, where the amplitude exponentially decays while preserving the coherent state structure. The average photon number $\langle \boldsymbol{n} \rangle = |\alpha|^2$ decreases as $|\alpha|^2 e^{-\kappa t}$, yet the quantum state remains a minimum uncertainty state with Poisson photon statistics throughout the decay process.

While pure intrinsic dephasing is negligible, the coupling to nonlinear elements can induce cavity dephasing. The corresponding jump operator is $\boldsymbol{L}_\phi = \boldsymbol{a}^\dagger \boldsymbol{a}$ with rate $\gamma_\phi$. Under dephasing, a coherent state $|\alpha\rangle$ evolves into a mixed state that retains the original Poissonian photon number distribution with $\langle \boldsymbol{n} \rangle = |\alpha|^2$, but loses all phase coherence between different Fock states.

### 2.1.5 Driving a QHO

We control our Quantum LC circuits by coupling them to a transmission line. In our architectures, this is accomplished by introducing a coupling pin, connected to an SMA connector, into the waveguide that hosts the resonator. The distance between the pin and resonator determines the coupling strength and thus the external quality factor of the resonator $Q_{\text{ext}}$.

For readout resonators, we aim to achieve the overcoupled regime where $Q_{\text{ext}} \ll Q_{\text{int}}$. This design choice ensures that the electromagnetic field of the resonator, which contains the information we are looking for, decays into our control line rather than dissipating into the environment. Conversely, we operate storage elements in the undercoupled regime where $Q_{\text{ext}} \gg Q_{\text{int}}$ to preserve their intrinsic lifetime without imposing an artificial limit.

Input-output theory provides the mathematical framework for how a microwave tone with amplitude $\epsilon(t)$ affects our resonator. Assuming the drive power significantly exceeds the coupling strength (the stiff pump approximation), we can express the drive Hamiltonian as [55]:

$$\frac{\boldsymbol{H}_{\text{drive}}}{\hbar} = \epsilon(t)\boldsymbol{a}^\dagger + \epsilon^*(t)\boldsymbol{a} \tag{2.27}$$

Where we've assumed the drive is resonant with the resonator.

The capabilities of just having a driving tone to manipulate a QHO are surprisingly limited. For an arbitrary drive $\epsilon(t)$, the resulting time evolution unitary is:

$$\boldsymbol{U}(t) = e^{-i(\boldsymbol{a}\int \epsilon^*(t)dt + \boldsymbol{a}^\dagger \int \epsilon(t)dt)} = e^{\boldsymbol{a}\alpha^* - \boldsymbol{a}^\dagger \alpha} \tag{2.28}$$

where $\alpha = i\int \epsilon(t)dt$. This is just the displacement operator, indicating that driving a QHO can only produce coherent states, which are rather unspectacular by themselves.

This fundamental limitation stems from the quantum harmonic oscillator's equally spaced energy levels. Since a drive cannot distinguish between transitions, it simultaneously excites and induces stimulated emission, always resulting in a coherent state. To access more interesting quantum states, such as Fock states, squeezed states, or cat states, we must couple our QHO to an element with uneven energy spacing - a non-quadratic potential.

## 2.2 Transmon

The Josephson junction is the circuit element that provides the sought-after non-quadratic potential. While structurally simple, it consists of two pieces of superconducting metal separated by a thin insulating layer as depicted in Fig. 2.5 (a); it is an element of rich physics enabled by superconductivity. The two Josephson equations capture its behavior [73]. The first Josephson equation relates the supercurrent going through the Junction to the phase difference $\varphi$ of the two superconducting wave functions on each side of the barrier.

$$I = I_c \sin(\varphi). \tag{2.29}$$

Here, $I_c$ is the junction's critical current, the maximum supercurrent that the junction can support before Cooper pairs begin to break, and the junction gains resistance. The second equation relates the time evolution of $\varphi$ to the voltage $V$ across the junction:

$$\frac{d\varphi}{dt} = \frac{2eV}{\hbar} \tag{2.30}$$

Combining these two equations and solving for the voltage reveals that a Josephson Junction behaves like a nonlinear Inductor.

$$V = \frac{\Phi_0}{2\pi I_c \cos(\varphi)} \frac{dI}{dt} = L_J(\varphi)\frac{dI}{dt} \tag{2.31}$$

where $L_J(\varphi) = \frac{\Phi_0}{2\pi I_c \cos(\varphi)}$ is the Josephson inductance. As a consequence, the Hamiltonian of a circuit where a Josephson junction replaces the inductor can be written as:

$$\boldsymbol{H} = 4E_C\left(\boldsymbol{n} - n_0\right)^2 - E_J \cos(\boldsymbol{\varphi}) \tag{2.32}$$

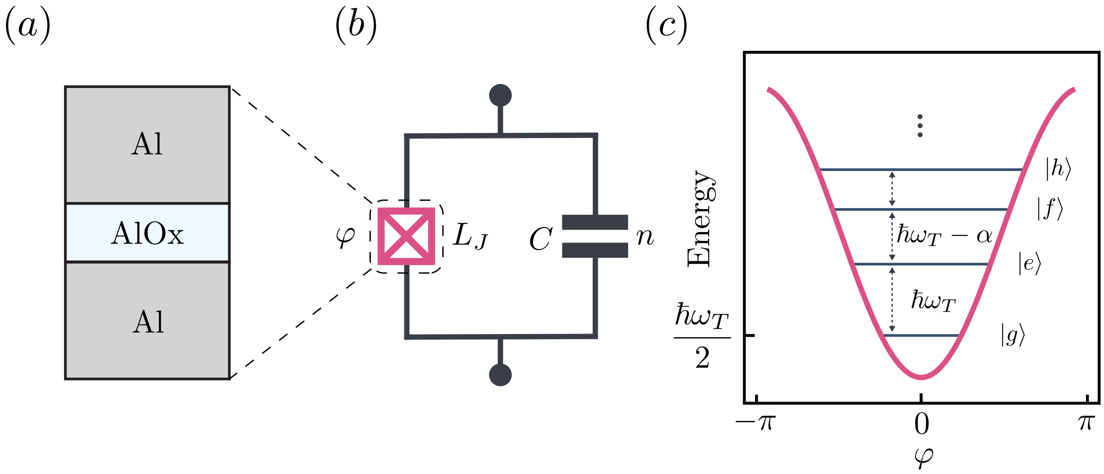

Figure 2.5: **Josephson junction, transmon circuit schematic and transmon spectrum.** (a) Physical structure of a Josephson junction consisting of two superconducting aluminum (Al) electrodes separated by a thin aluminum oxide (AlOx) tunnel barrier. Cooper pairs can tunnel through this insulating layer. The dynamics are described by the Josephson effect. (b) Circuit representation of a transmon, where a large capacitor shunts the Josephson junction. (c) Energy spectrum of the transmon showing the cosine potential as a function of phase $\varphi$. The energy levels are unevenly spaced, with the transition frequency between |g⟩ and |e⟩ being $\hbar\omega_T$. The anharmonicity $\alpha$ reduces higher transitions. This uneven spacing enables selective addressing of specific transitions, making the transmon function as a controllable two-level system or qubit.

where $E_C = \frac{e^2}{2C}$ is the capacitive energy across the junction and $E_J = \frac{\hbar I_c}{2e}$ is the inductive energy of the Josephson junction. $n_0$ catches the effects of any offset charge. The energetic landscape of this circuit depends on the particular design choice of $E_C$ and $E_J$.

The crucial insight that led to the conception of the transmon is that both charge sensitivity, a dominant decoherence factor in the earlier Cooper pair box design [34], and anharmonicity, the difference between the two energy levels, decrease with increasing $E_J/E_C$. Crucially, the charge sensitivity decreases exponentially, while the anharmonicity only decreases algebraically [37]. With $E_J/E_C \gtrsim 50$, the charge sensitivity becomes negligible while the anharmonicity is still sufficient for fast operations. In our system, we operate with $E_C \sim 200\text{-}300$ MHz and $E_J \sim 5\text{-}20$ GHz. Physically, this is achieved by having a junction connect two large capacitor pads that shunt the small intrinsic capacitance of the junction, effectively suppressing the effect of charge noise. The resulting circuit diagram is shown in Fig. 2.5 (b).

To simplify the Hamiltonian, it is instructive to pull the second-order term out of the cosine;

we also drop the offset charge. This allows us to write the Hamiltonian as the sum of two parts: a linear and a non-linear part.

$$\boldsymbol{H}_T = 4E_C\boldsymbol{n}^2 + \frac{E_J}{2}\boldsymbol{\varphi}^2 + \boldsymbol{H}_{4+}\left(\boldsymbol{\varphi}\right) \tag{2.33}$$

with $\boldsymbol{H}_{4+}\left(\boldsymbol{\varphi}\right) = -E_J\left(\cos(\boldsymbol{\varphi}) + \frac{\boldsymbol{\varphi}^2}{2}\right)$, the linear part takes the same form as for the previously discussed QHO. It is key to observe that $\boldsymbol{H}_{4+}$ depends on $\boldsymbol{\varphi}$, whose magnitude depends on the vacuum fluctuation $\varphi^{ZPF} = \left(\frac{2E_C}{E_J}\right)^{\frac{1}{4}} \lesssim 0.5$. Consequently, we can treat the non-linear part as a perturbation and diagonalize the linear part as done before for the QHO. The transmon Hamiltonian then follows as

$$\begin{aligned}\boldsymbol{H}_T &= \sqrt{8E_CE_J}\boldsymbol{q}^\dagger\boldsymbol{q} + \boldsymbol{H}_{4+}\left(\varphi^{ZPF}(\boldsymbol{q}+\boldsymbol{q}^\dagger)\right) && (2.34)\\ &\approx \sqrt{8E_CE_J}\boldsymbol{q}^\dagger\boldsymbol{q} - \frac{E_J}{24}\left(\varphi^{ZPF}\right)^4\left(\boldsymbol{q}+\boldsymbol{q}^\dagger\right)^4 && (2.35)\\ &\approx \hbar\omega_T\boldsymbol{q}^\dagger\boldsymbol{q} - \frac{\hbar\alpha}{2}\boldsymbol{q}^{\dagger 2}\boldsymbol{q}^2 && (2.36)\end{aligned}$$

where we use $\hbar\omega_T = \sqrt{8E_CE_J} - E_C$ and $\hbar\alpha = \frac{E_J}{2}\left(\varphi^{ZPF}\right)^4 = E_C$. In the last step, the rotating wave approximation was invoked to drop any terms that do not have the same number of $\boldsymbol{q}$ and $\boldsymbol{q}^\dagger$. Equation 2.36 is the Hamiltonian of an anharmonic oscillator with its spectrum shown in Fig. 2.5(c). The anharmonicity results in a reduction of the energy level spacing.

Next, we discuss how this anharmonicity allows us to operate a transmon as a qubit through an appropriate choice of drive parameters.

### 2.2.1 Driving a transmon

Transmons are coupled to external control electronics through the same mechanism as QHOs. A pin connected to a transmission line capacitively couples to the transmon's dipole moment, enabling control operations. Like storage elements, we operate transmons in the undercoupled regime where the coupling to external lines is much weaker than the intrinsic decay rates.

The full Hamiltonian for a driven transmon can be written as:

$$\frac{\boldsymbol{H}}{\hbar} = \omega_T\boldsymbol{q}^\dagger\boldsymbol{q} - \frac{\alpha}{2}\boldsymbol{q}^{\dagger 2}\boldsymbol{q}^2 + \Omega^*(t)e^{-i\omega_d t}\boldsymbol{q} + \Omega(t)e^{i\omega_d t}\boldsymbol{q}^\dagger \tag{2.37}$$

where $\Omega(t)$ represents the time-dependent drive amplitude at frequency $\omega_d$. Moving into the rotating frame of the transmon at $\omega_T$ and assuming that the drive is played on resonance with that transmon, $\omega_d = \omega_T$, this Hamiltonian takes the form:

$$\frac{\boldsymbol{H}}{\hbar} = -\frac{\alpha}{2}\boldsymbol{q}^{\dagger 2}\boldsymbol{q}^2 + \Omega^*(t)\boldsymbol{q} + \Omega(t)\boldsymbol{q}^\dagger \tag{2.38}$$

Here, the effect of the anharmonicity becomes apparent. If the qubit is in its ground state, the anharmonicity has no impact, and the drive acts in resonance. For subsequent energy levels, the anharmonicity shifts the frequency, resulting in the drive being off-resonant. As a consequence, the drive will only affect the transition if $\Omega(t)$ has Fourier components at these transition frequencies. Hence, the bandwidth of a drive pulse determines which transitions are addressed simultaneously. Assuming a Gaussian envelope, we can calculate the bandwidth of a pulse as $\sigma_f = 1/2\pi\sigma_t$, where $\sigma_t$ is the standard deviation of the Gaussian pulse duration. Hence, we can operate the transmon as a two-level system if our drives are sufficiently long. Typical anharmonicities of $\alpha = 180\text{-}300$ MHz set the limit for simple Gaussian pulses to tens of nanoseconds.

This spectral constraint has motivated the development of pulse-shaping techniques, such as DRAG [74], to shape transmon control pulses, to suppress the Fourier components at higher transition frequencies. These methods enable rapid operations of the transmon as an effective two-level system by carefully controlling the spectral content of drive pulses, ensuring that the population of higher energy levels remains negligible. Next, I will introduce the notion of a qubit and develop the corresponding mathematical concepts.

### 2.2.2 Operating the transmon as a qubit

The anharmonicity of the transmon affords the capability to operate it as a qubit. Suppose the bandwidth of our transmon pulses $\Omega(t)$ is smaller than $\alpha$. In that case, the induced dynamics are confined to the first two transmon levels, allowing us to truncate our Hamiltonian and effectively turn it into a qubit.

The states of a qubit are given by the two eigenstates $|0\rangle$ and $|1\rangle$, and any qubit state can be written as a superposition of these two states:

$$|\psi\rangle = \alpha\,|0\rangle + \beta\,|1\rangle \tag{2.39}$$

where $\alpha$ and $\beta$ are complex numbers and satisfy the normalization condition $|\alpha|^2 + |\beta|^2 = 1$. Alternatively, we can parameterize any qubit state using the Bloch sphere representation shown in Fig. 2.6:

$$|\psi\rangle = \cos(\theta/2)\,|0\rangle + e^{i\phi}\sin(\theta/2)\,|1\rangle \tag{2.40}$$

where $\phi$ and $\theta$ are the polar and azimuthal angles on the Bloch sphere, respectively. Qubit states and operations are described by the Pauli matrices, which form a complete basis for all

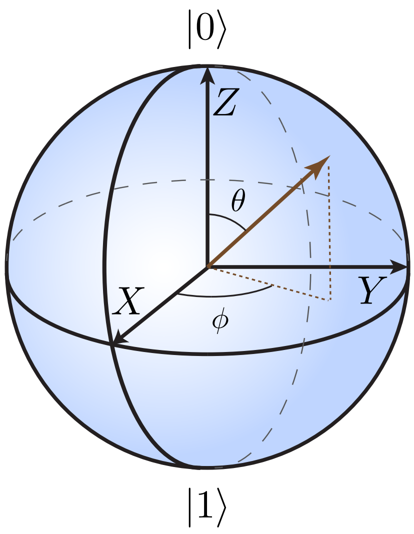

Figure 2.6: **Blochsphere representation.** The Blochsphere is a useful tool to visualize qubit states. Pure states live on the surface of the Bloch sphere and are fully characterized by the two angles $\phi$ and $\theta$. The poles are given by the states $|0\rangle$ and $|1\rangle$. Qubit gates take the form of rotations around different axes on the Blochsphere.

single-qubit operations:

$$\boldsymbol{\sigma}_x = |0\rangle\langle 1| + |1\rangle\langle 0| = \begin{pmatrix} 0 & 1 \\ 1 & 0 \end{pmatrix} \tag{2.41}$$

$$\boldsymbol{\sigma}_y = -i\,|0\rangle\langle 1| + i\,|1\rangle\langle 0| = \begin{pmatrix} 0 & -i \\ i & 0 \end{pmatrix} \tag{2.42}$$

$$\boldsymbol{\sigma}_z = |0\rangle\langle 0| - |1\rangle\langle 1| = \begin{pmatrix} 1 & 0 \\ 0 & -1 \end{pmatrix} \tag{2.43}$$

These operators represent rotations around the corresponding axes of the Bloch sphere.

Using the Pauli matrices, we write the qubit Hamiltonian as:

$$\boldsymbol{H}_q = \frac{\omega_q}{2}\boldsymbol{\sigma}_z \tag{2.44}$$

where $\omega_q$ is the qubit frequency. The qubit drive Hamiltonian takes the form:

$$\boldsymbol{H}_{\text{drive}} = |\Omega(t)|(\cos(\phi)\boldsymbol{\sigma}_x + \sin(\phi)\boldsymbol{\sigma}_y) \tag{2.45}$$

where $|\Omega(t)|$ is the absolute value of the drive amplitude and $\phi$ is the phase of the drive, which determines the rotation axis.

### 2.2.3 Decoherence channels

Transmons are vulnerable to environmental-induced decoherence that limits their quantum coherence. These interactions manifest through energy relaxation characterized by $T_1$ and pure dephasing characterized by $T_\phi$, with the total dephasing time $T_2$ related through the standard expression $1/T_2 = 1/2T_2 + 1/T_\phi$.

Energy relaxation in transmons arises from several mechanisms, with dielectric losses typically being dominant. Two-level systems (TLS) in the amorphous aluminum oxide barrier of Josephson junctions and at various material interfaces cause energy dissipation through their fluctuating electric dipole moments [75, 76]. Substrate losses, Purcell decay through coupling to transmission line modes, and recently identified quasiparticle-induced effects also contribute to $T_1$ limitations [77]. The relative impact of these mechanisms depends strongly on device geometry, materials, and fabrication processes.

Pure dephasing in fixed-frequency transmons primarily originates from charge noise coupling through residual charge sensitivity, critical current fluctuations in Josephson junctions, and low-frequency magnetic field noise. The absence of flux control lines eliminates the dominant flux noise channel that typically limits tunable transmon architectures. Additionally, TLS exhibits complex dynamics including spectral diffusion and environmental coupling that can modulate qubit frequencies [78, 79].

Recent materials research has demonstrated significant potential for coherence improvements. While aluminum remains widely used for Josephson junctions due to its reliable fabrication and well-understood properties, replacing the electrodes with tantalum or niobium has shown enhanced performance, with recent demonstrations achieving coherence times exceeding $1\ \mathrm{ms}$ [80, 81]. However, achieving such improvements requires careful optimization of fabrication processes and environmental control.

In practice, transmon coherence times vary significantly based on fabrication quality and environmental conditions. Typical $T_1$ times range from tens to hundreds of microseconds, with $T_{2e}$ often approaching $2T_1$ under dynamical decoupling. The ratio $T_\phi/T_1$ is generally favorable compared to flux-tunable devices, making fixed-frequency transmons a more attractive choice for state preparation and readout purposes.

The mathematical description of decoherence employs the Lindblad formalism, introduced in a previous section. Energy relaxation is described by the jump operator $\boldsymbol{L}_1 = \boldsymbol{\sigma}_- = |g\rangle\langle e|$ at rate $\gamma_1 = 1/T_1$, causing exponential decay from the excited state to the ground state. Pure dephasing uses the jump operator $\boldsymbol{L}_\phi = \boldsymbol{\sigma}_z = |e\rangle\langle e| - |g\rangle\langle g|$ at rate $\gamma_\phi = 1/T_\phi$, which preserves state populations while destroying phase coherence.

## 2.3 Coupling QHOs and transmons

The previous sections introduced the two main building blocks of bosonic cQED and discussed their individual control. We observed that driving a QHO can only generate trivial coherent states. To access the rich variety of non-Gaussian states essential for quantum information processing, we require a nonlinear element, the transmon. We can capacitively couple these two elements by placing them in physical proximity, such that the electric field of the resonator extends into the region occupied by the transmon, creating a shared capacitance between the two. The strength and nature of this interaction depend on their physical and spectral proximity.

I think about coupling through the lens of mode hybridization. The classical example is two pendulums coupled by a spring. When the pendulums oscillate independently, each has its characteristic frequency determined by its length and mass. However, once connected by a spring, the system's dynamics fundamentally change; the motion of one pendulum directly influences the other through their shared coupling element. The result is a transformation from individual oscillations to collective behavior. The system no longer supports the original (bare) uncoupled modes. Instead, it exhibits two new normal modes: a symmetric mode, where both pendulums swing in phase, and an antisymmetric mode, where they oscillate out of phase. The frequencies of these hybridized modes shift away from the original pendulum frequencies, with the magnitude of this shift determined by the strength of the spring's coupling. Strong coupling creates a large frequency splitting between the two normal modes, while weak coupling results in only minor deviations (dressed) from the original frequencies.

To derive the effective interaction of the QHO and transmon, we begin with several key assumptions. First, the geometric coupling strength $g$ must be much smaller than the mode detuning: $g \ll |\Delta| = |\omega_T - \omega_R|$. Second, the transmon anharmonicity should be weak compared to this detuning: $\alpha = E_C/\hbar \ll |\Delta|$. Finally, we invoke the rotating wave approximation where $|\Delta| \ll \omega_T + \omega_R$ allows us to neglect rapidly oscillating terms.

Under these conditions, the coupled system Hamiltonian takes the form:

$$\boldsymbol{H} = \hbar\omega_R \boldsymbol{a}^\dagger \boldsymbol{a} + \hbar\omega_T \boldsymbol{q}^\dagger \boldsymbol{q} + \boldsymbol{H}_{4+}(\boldsymbol{\varphi}) + \hbar g(\boldsymbol{a}\boldsymbol{q}^\dagger + \boldsymbol{a}^\dagger \boldsymbol{q}) \tag{2.46}$$

The strategy for finding the dispersive Hamiltonian involves two steps: First, we diagonalize the linear coupling term by transforming to dressed modes, then we re-express the nonlinear terms in this new basis to reveal the resulting dispersive interaction.

The transformation from bare to dressed modes occurs through a "rotation" that mixes the cavity and transmon operators [54]:

$$\tilde{\boldsymbol{a}} = \cos(\theta)\boldsymbol{a} + \sin(\theta)\boldsymbol{q} \approx \boldsymbol{a} + \frac{g}{\Delta}\boldsymbol{q} \tag{2.47}$$

$$\tilde{\boldsymbol{q}} = -\sin(\theta)\boldsymbol{a} + \cos(\theta)\boldsymbol{q} \approx -\frac{g}{\Delta}\boldsymbol{a} + \boldsymbol{q} \tag{2.48}$$

Here, the angle $\theta = \arctan(2g/\Delta)$ quantifies the mixing of the two modes. In the dispersive limit where $g \ll |\Delta|$, this mixing is small, justifying the linearized approximations shown. This transformation eliminates the linear coupling term and shifts the mode frequencies according to $\tilde{\omega}_R = \omega_R + g^2/\Delta$ and $\tilde{\omega}_T = \omega_T - g^2/\Delta$. These frequency shifts are known as Lamb shifts. An important consequence of mode hybridization is loss inheritance. The high-$Q$ mode acquires additional decay through its coupling to the lower-$Q$ mode, with the induced decay rate $\Gamma_P = 2(g/\Delta)^2\kappa$, where $\kappa$ is the decay rate of the low-$Q$ mode.

To find the effective nonlinear interactions, we now express the transmon's phase operator in terms of the dressed modes:

$$\varphi_T^{\mathrm{ZPF}}\left(\boldsymbol{q} + \boldsymbol{q}^\dagger\right) \approx \varphi_T^{\mathrm{ZPF}}\left(\tilde{\boldsymbol{q}} + \tilde{\boldsymbol{q}}^\dagger\right) + \varphi_T^{\mathrm{ZPF}}\frac{g}{\Delta}\left(\tilde{\boldsymbol{a}} + \tilde{\boldsymbol{a}}^\dagger\right) \tag{2.49}$$

Substituting this into $\boldsymbol{H}(\boldsymbol{\varphi})$ yields the Hamiltonian:

$$\boldsymbol{H} = \hbar\omega_R\tilde{\boldsymbol{a}}^\dagger\tilde{\boldsymbol{a}} + \hbar\omega_T\tilde{\boldsymbol{q}}^\dagger\tilde{\boldsymbol{q}} + \boldsymbol{H}_{4+}(\varphi_T^{\mathrm{ZPF}}\left(\tilde{\boldsymbol{q}} + \tilde{\boldsymbol{q}}^\dagger\right) + \varphi_T^{\mathrm{ZPF}}\frac{g}{\Delta}\left(\tilde{\boldsymbol{a}} + \tilde{\boldsymbol{a}}^\dagger\right)) \tag{2.50}$$

Expanding the nonlinear terms to fourth order and applying the rotating wave approximation yields the final dispersive Hamiltonian that we operate with. From this point on, I will treat the dressed modes as my default modes and drop the tildes to remove clutter:

$$\frac{\boldsymbol{H}_{\text{dispersive}}}{\hbar} = \omega_R\boldsymbol{a}^\dagger\boldsymbol{a} + \omega_T\boldsymbol{q}^\dagger\boldsymbol{q} - \frac{\alpha}{2}\boldsymbol{q}^{\dagger 2}\boldsymbol{q}^2 - \frac{K}{2}\boldsymbol{a}^{\dagger 2}\boldsymbol{a}^2 - \chi\boldsymbol{q}^\dagger\boldsymbol{q}\boldsymbol{a}^\dagger\boldsymbol{a} \tag{2.51}$$

This Hamiltonian has two new components, in addition to the transmon anharmonicity. First, as a consequence of hybridizing with a nonlinear element, the resonator inherits a self-Kerr nonlinearity with strength:

$$\hbar\frac{K}{2} = \frac{E_J}{2}\left(\varphi_T^{\mathrm{ZPF}}\right)^4\left(\frac{g}{\Delta}\right)^4 = E_C\left(\frac{g}{\Delta}\right)^4 \tag{2.52}$$

Second, the coupling between the transmon and the resonator manifests as a state-dependent frequency shift between the modes, characterized by the dispersive coupling strength:

$$\hbar\chi = E_J \left(\varphi_T^{\text{ZPF}}\right)^4 \left(\frac{g}{\Delta}\right)^2 = 2E_C \left(\frac{g}{\Delta}\right)^2 \tag{2.53}$$

This cross-Kerr interaction forms the foundation for quantum non-demolition measurements and conditional operations, enabling universal control in circuit QED systems. Assuming typical values such as $g/2\pi \sim 10\text{-}300\,\text{MHz}$, $\Delta/2\pi \sim 1\text{-}3\,\text{GHz}$, we find $\chi/2\pi \sim 30\,\text{kHz}–2\,\text{MHz}$ and $K/2\pi \sim 1\,\text{Hz}–100\,\text{kHz}$. Critically, $\chi$ and $K$ both depend on $g/\Delta$ and are thus dependent. Keeping $K$ small $\sim 1\,\text{Hz}$ is a major motivation to operate in the weak dispersive coupling regime with $\chi/2\pi \sim 30\text{-}100\,\text{kHz}$.

The dispersive Hamiltonian as written in eq. 2.51 rests on several assumptions. Crucially, based on the assumption that $g \ll \Delta$, we neglected higher-order terms. This is invalid for large photon numbers in the cavity. To illustrate this, we consider the sixth-order dispersive shift.

$$-\chi' \boldsymbol{a}^{\dagger 2}\boldsymbol{a}^2\boldsymbol{q}^\dagger\boldsymbol{q} \tag{2.54}$$

with $\chi' = 2E_C(\varphi_T^{ZPF})^2\left(\frac{g}{\Delta}\right)^4 \sim 0.1\,\text{Hz}–1\,\text{kHz}$, which is typically small enough such that neglecting these terms is justified. However, this term scales with $\boldsymbol{n}^2$ and will thus explode for larger photon numbers. The critical photon number provides a useful heuristic for determining when these higher-order terms become dominant.

$$n_{\text{crit}} = \frac{1}{2j+1}\left(\frac{|\Delta - jE_C/\hbar|^2}{4g^2} - j\right) \tag{2.55}$$

where $j = 0, 1, \ldots$ refers to the qubit state [55]. For the ground state, the critical photon number takes the form $n_{\text{crit}} = (\Delta/2g)^2$. Thus, to safely operate in the dispersive regime, we must ensure that $n \ll n_{\text{crit}}$.

## 2.4 Operating a bosonic cQED architecture

The dispersive interaction derived in the previous section affords both quantum non-demolition measurements and universal control of the storage cavity. Concretely, for readout, the cross-Kerr term $-\chi\boldsymbol{a}^\dagger\boldsymbol{a}\boldsymbol{q}^\dagger\boldsymbol{q}$ acts as a qubit state-dependent frequency shift that alters the response of the readout resonator to a probing tone, allowing the distinction of the two qubit states. For control, the dispersive Hamiltonian offers several distinct schemes. Most straightforward, the state-dependent frequency shift allows for the enactment of conditional phase gates between

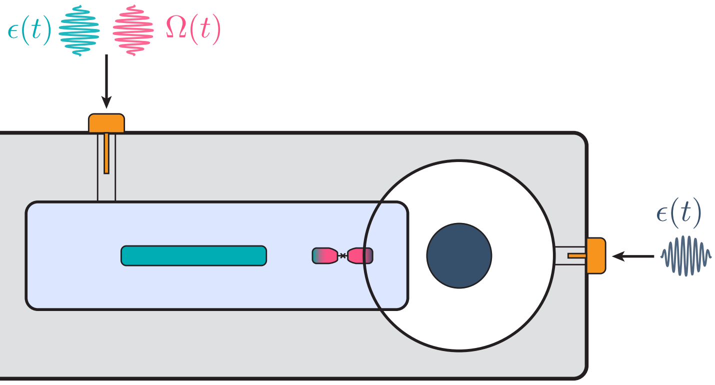

Figure 2.7: **Schematic of a standard bosonic cQED device.** A standard bosonic cQED device consists of a storage mode (dark blue), an ancilla transmon (pink) to control the storage mode, and a readout resonator (turquoise) to read out the qubit state. The spectral and spatial separation of the different modes is carefully chosen to achieve the desired Hamiltonian parameters. The modes are capacitively coupled to transmission lines over which pulses are sent to control the system.

the qubit and the storage. Furthermore, it enables pulses with narrow spectral selectivity to interact with the qubit/cavity conditioned on the state of the cavity/qubit. Beyond these direct applications of the dispersive Hamiltonian, the nonlinearity of the Josephson junction can also be utilized as a four-wave mixing element, resulting in parametric interactions when driven with appropriately detuned tones.

Fig. 2.7 shows the schematic of a standard bosonic cQED architecture. It consists of a high-$Q$ coaxial stubline storage cavity for information encoding (blue), an ancilla transmon (pink), and a stripline-resonator strongly coupled to a transmission line (turquoise). For the following discussion of non-demolition readout and control, we will limit ourselves to the corresponding subsystems readout-qubit and qubit-storage. A choice that is justified by designing the system such that readout storage crosstalk is negligible.

### 2.4.1 Dispersive readout

The dispersive interaction between the qubit and readout resonator enables quantum non-demolition measurement of the qubit state. This readout mechanism utilizes the state-dependent frequency shift of the resonator, where the excitation of a qubit shifts the resonator frequency.

By probing the resonator response near its eigenfrequency, we can infer the qubit state from the signal without directly probing the qubit itself.

The input-output formalism describes how an input pulse interacts with the system and, combined with the system's response, turns into the output field that we collect in our measurement apparatus. [55]

$$\boldsymbol{a}_{\text{out}} = \boldsymbol{a}_{\text{in}} + \sqrt{\kappa}\boldsymbol{a} \tag{2.56}$$

Here, $\boldsymbol{a}$ describes the field of the resonator, $\boldsymbol{a}_{\text{in}}$ the incoming control field, and $a_{\text{out}}$ the combined returning field. To find the response of the system, we consider the Hamiltonian in the rotating frame of the qubit and a resonator drive at $\omega_R - \chi/2$:

$$\frac{\boldsymbol{H}_{\text{int}}}{\hbar} = -\frac{\chi}{2}\boldsymbol{a}^\dagger\boldsymbol{a}\boldsymbol{\sigma}_z + \epsilon(t)\boldsymbol{a}^\dagger + \epsilon^*(t)\boldsymbol{a} \tag{2.57}$$

While this Hamiltonian governs the coherent evolution of the resonator, for readout, we must also account for the resonator's strong coupling to the transmission line, which introduces decay at a rate $\kappa$. When the qubit is projected into a definite state, we are only concerned with the trajectories of coherent states, and the system reduces to a damped, driven harmonic oscillator described by classical equations of motion.

$$\dot{\alpha}_g(t) = -\left(\frac{\kappa}{2} + i(\Delta + \frac{\chi}{2})\right)\alpha_g(t) - i\epsilon(t) \tag{2.58}$$

$$\dot{\alpha}_e(t) = -\left(\frac{\kappa}{2} + i(\Delta - \frac{\chi}{2})\right)\alpha_e(t) - i\epsilon(t) \tag{2.59}$$

$$\tag{2.60}$$

where $\Delta$ is detuning from the assumed drive frame. We can solve these equations to find the response of the resonator to a readout pulse $\epsilon(t)$.

To visualize the dynamics of these equations, we can interpret them as the interplay of three forces acting in phase space, as illustrated in Fig. 2.8 (a). The drive $\epsilon$ acts as a uniform force field, the decay $\kappa$ as a re-centering force toward the origin, while the dispersive shift $\chi$ results in a qubit state-dependent tangential force. Assuming a constant drive, the resonator is driven into a qubit state-dependent steady state [55]:

$$\alpha^s_{g/e} = \frac{-\epsilon}{(\Delta \pm \chi/2) - i\kappa/2} = \frac{2\epsilon}{\sqrt{(\kappa/2)^2 + (\Delta \pm \chi/2)^2}}e^{i\phi_\pm} \tag{2.61}$$

with $\phi_\pm = \arctan(\frac{\Delta\pm\chi/2}{\kappa/2})$. For $\Delta = 0$, the qubit state information is encoded in the phase of the steady-state response.

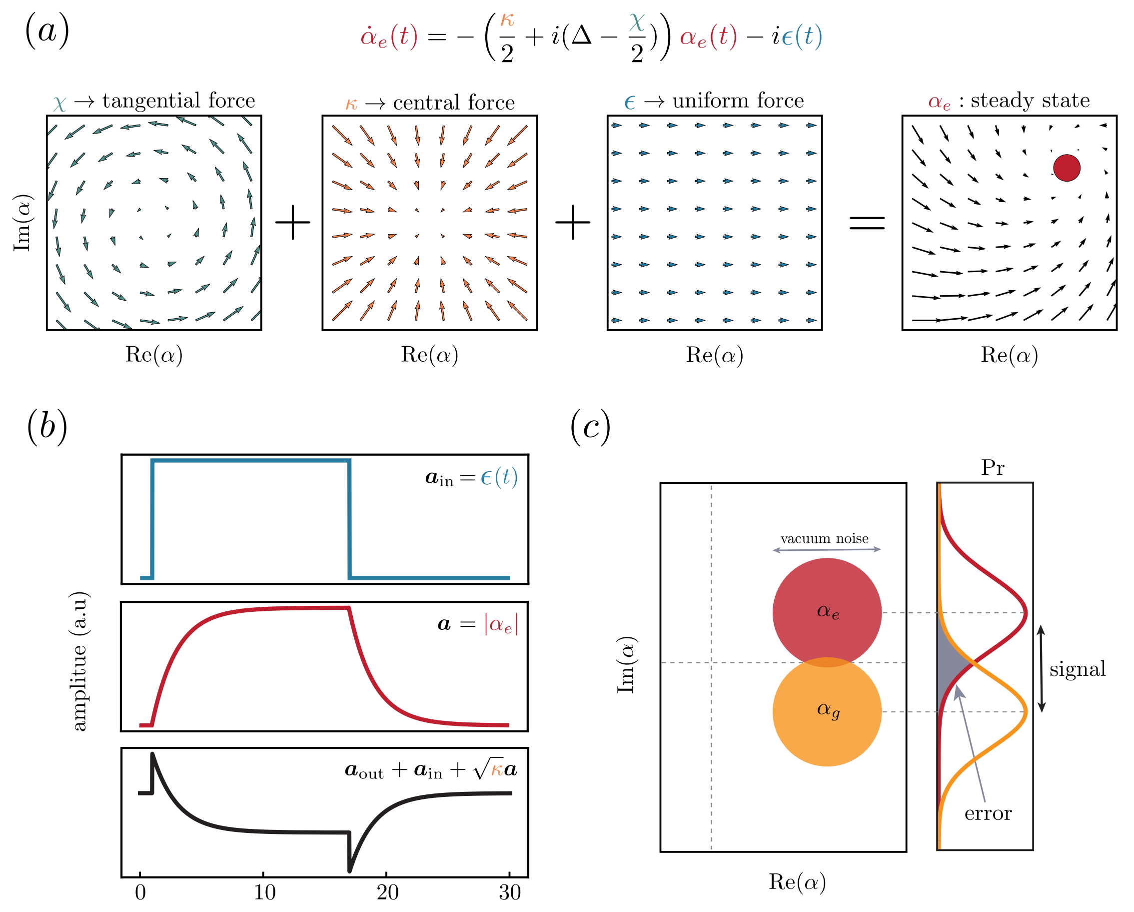

Figure 2.8: **Dispersive readout mechanism.** (a) Dynamics of the readout resonator during dispersive readout is an interplay of three forces. The uniform drive force pushes in one direction in phase space, the decay acting as a central force and a qubit state-dependent tangential force (here for $|e\rangle$). (b) Input field, cavity field, and output field as calculated through the Input-Output formalism for an input square pulse. (c) Integrating many trajectories leads to two Gaussian distributions for $|g\rangle$ and $|e\rangle$. The distance between these peaks is the signal, while the overlap gives the error. The width of the Gaussian is, by default, equal to the vacuum noise.

The interaction of the different fields as described by the input-output formalism, as shown in Fig. 2.8 (b). A traditional readout process consists of three distinct phases. Initially, the resonator field $\boldsymbol{a}$ rings up from vacuum to its steady-state value, then maintains constant amplitude during the drive pulse, and finally rings down when the drive is extinguished. The measured output field reflects both the reflected incident drive and the resonator's response.

After the returned readout signal is sampled, it is integrated using weights. These integration weights are chosen to increase the discrimination between qubit states by emphasizing periods with large state separation and weakening the contribution of periods with low separation. After the integration, we end up with a single phase-space point that we can use to infer the qubit state. Repeated measurements produce two Gaussian distributions as depicted in Fig. 2.8 (c). For single-shot readout, we establish a threshold between these distributions and use it to assign each measurement outcome to either $|g\rangle$ or $|e\rangle$.

What makes a good readout? We can quantify the quality of our readout in terms of two numbers, the fidelity $\mathcal{F}$ and the quantum non-demolitioness $\mathcal{Q}$. $\mathcal{F}$ quantifies the confidence that our threshold assignment is correct, while $\mathcal{Q}$ measures if the readout process disturbed the qubit state. Additionally, we would like our readout to be as fast as possible. These quantities can be inferred by performing the "butterfly measurement scheme" on the transmon, for more details, see Ref. [54].

The readout fidelity fundamentally depends on the signal-to-noise ratio, which is determined by the separation between the Gaussian distributions (signal) relative to their widths (noise). This relationship suggests that simply increasing pulse duration and amplitude should improve discrimination by enhancing the steady-state signal while maintaining constant vacuum noise levels. However, the underlying dynamics impose more nuanced constraints that limit this naive approach. Longer readout pulses increase the probability of spontaneous qubit decay during measurement, directly degrading the QND-ness and fidelity. Further, large photon populations in the readout resonator break the dispersive approximation and can reduce qubit coherence through ionization processes, where high-energy photons cause quasiparticle generation that dephases the superconducting qubit [82]. These competing effects create a fundamental trade-off between measurement strength, length, and quality. It is therefore essential to maximize the signal-to-noise ratio for a low enough photon number that does not disturb the qubit. Under the assumption that steady state is reached, this can be achieved by setting $\chi = \kappa$ [9].

The discussion above reveals the trade-offs governing the dispersive readout process. While the simple square pulse used in the debate provides a good baseline, the multidimensional optimization problem of maximizing assignment fidelity, achieving QNDness, and minimizing time suggests that significant improvements can be made by optimizing the waveform. Traditional approaches have postulated fixed alternative waveforms, such as CLEAR [83]; however, optimizing the entire parameter space has remained largely unexplored.

In a recent publication with Aniket Chatterjee, we demonstrated the efficacy of mode-free reinforcement learning for discovering optimal readout pulses [84]. This approach utilizes

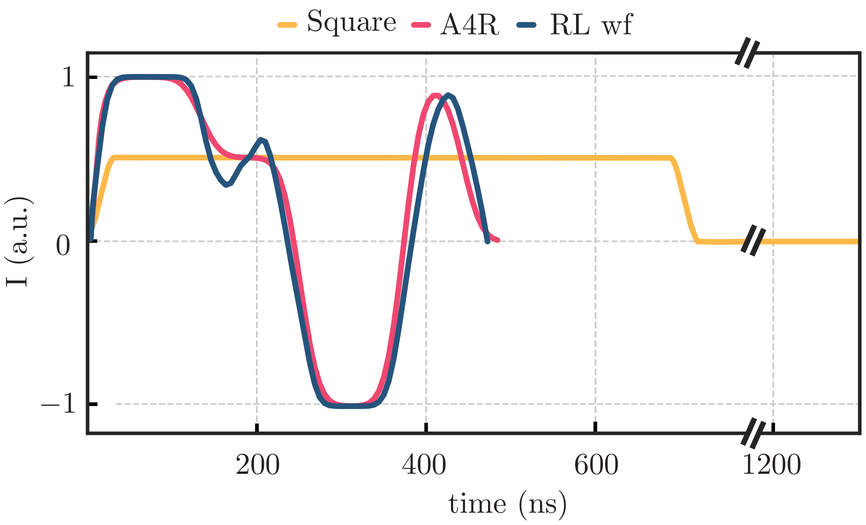

Figure 2.9: **Readout pulse comparison.** Comparison of a square (yellow), A4R (red), and RL (blue) waveform for the system with $\kappa = 10.4\,\text{MHz}$ and $\chi = 0.42\,\text{MHz}$. The waveforms include the reset time. For the same fidelity, the A4R and RL waveforms achieve a significant speedup compared to the default square pulse. For more details, see Ref. [84].

the proximal policy optimization (PPO) algorithm to optimize the high-dimensional readout waveform in terms of various performance metrics. The Reinforcement learning (RL) agent optimizes the pulse by interacting with a physically motivated training environment, utilizing the quasi-classical Langevin equations (see Equation 2.60) along with qubit decay.

Remarkably, the RL agent consistently converges to a physically intuitive, generalizable waveform structure across different parameter regimes, which we refer to as Active Four-tone Readout (A4R). A4R consists of four distinct segments. A high-amplitude ring-up tone that rapidly drives the resonator into steady state, a readout segment optimized for maximum state discrimination, and a two-tone reset sequence that rapidly depletes the resonator population. The A4R waveform, along with the actual RL-waveform and a square pulse for comparison, is shown in Fig. 2.9. The pulse form can achieve state-of-the-art fidelities while reducing the total readout and reset time by a factor of 2. Ref. [84] discusses the tune-up of A4R in detail.

Beyond pulse optimization, readout fidelity can be substantially improved by using quantum-limited amplifiers. They operate close to the fundamental quantum limit by adding minimal excess noise, making them the ideal candidate for the first part of the amplification chain. Two commonly used architectures are the Josephson parametric amplifier (JPA) [85] and the Josephson traveling-wave parametric amplifier (JTWPAs) [86].

JPAs utilize the nonlinear inductance of a single Josephson junction driven by a strong pump tone to create parametric gain, typically providing 15-20 dB of amplification within a narrow bandwidth around the resonant frequency. JTWPAs distribute this nonlinearity along a transmission line structure, enabling broadband amplification with reduced pump power requirements and improved dynamic range.

### 2.4.2 Dispersive control

The same Hamiltonian that is used for readout can also be utilized for cavity control. In the double rotating frame of cavity and qubit, and with cavity and qubit drive on resonance, it takes the form:

$$\frac{\boldsymbol{H}}{\hbar} = -\chi \boldsymbol{a}^\dagger \boldsymbol{a} \left| e \right\rangle \left\langle e \right| + \epsilon(t)\boldsymbol{a}^\dagger + \epsilon(t)\boldsymbol{a} + \Omega^*(t)\boldsymbol{\sigma}_- + \Omega(t)\boldsymbol{\sigma}_+ \tag{2.62}$$

This Hamiltonian provides universal control over the qubit cavity space. As such, for any wanted unitary $\boldsymbol{U}(t)$, there exists a set of drives $\epsilon(t)$ and $\Omega(t)$ that implements it. Optimal control theory schemes, such as Gradient Ascent Pulse Engineering (GRAPE) [87], utilize optimization algorithms to determine the desired drives. However, this approach becomes computationally expensive for a multi-oscillator system and is impractical to scale. It is therefore crucial to have a well-defined set of universal gates that we can use to decompose any unitary. The particular form of available gates also dictates which kind of operations and encoding schemes are most feasible. We will find that, depending on the magnitude of $\chi$, the fundamental control scheme is formed by different gate sets.

#### Conditional rotations

The first case to consider is the absence of external drives, where $\Omega(t) = \epsilon(t) = 0$. Importantly, the system does not remain static. Rather than implementing the identity operation one might intuitively expect, the dispersive interaction generates a conditional rotation:

$$\boldsymbol{C}_R(\theta) = e^{i\theta \boldsymbol{a}^\dagger \boldsymbol{a} \left| e \right\rangle \left\langle e \right|} \tag{2.63}$$

where $\theta = \chi t$ is the accumulated phase during the interaction time. This gate has two complementary interpretations. It either leads to an overall rotation of the cavity, depending on the qubit state, or to a photon number-dependent phase pickup on the qubit. This gate will entangle the qubit and the cavity, unless the qubit is in an eigenstate of $\boldsymbol{\sigma}_z$, the cavity is in vacuum, or $\theta$ is a multiple of $2\pi$. A particular important case is $t = \pi/\chi$, implementing the photon parity operator

$$\boldsymbol{\mathcal{P}} = e^{-i\pi \boldsymbol{a}^\dagger \boldsymbol{a}|e\rangle\langle e|} \tag{2.64}$$

This gate, in combination with qubit rotations, can be used to measure the cavity's photon number parity [88] and allows direct access to the Wigner function. It is also of importance for rotationally symmetric bosonic codes [89], such as the cat code, where bit-flip errors manifest as a parity change.

A crucial question for control is what the gate depends on and how quickly it operates. In this case, the answer is simple as the gate only consists of waiting for $\chi$ to induce a rotation/phase; as such, the gate time scales directly with $\chi$, $t_{\text{gate}} \propto 1/\chi$. As a consequence, any protocol that wants to use parity needs a large $\chi$, typically around $\chi/2\pi \sim 1$ MHz.

The gate set consisting of the controlled rotation gate, arbitrary qubit rotations, and cavity displacements $[\boldsymbol{C}_R(\theta), \boldsymbol{R}_\varphi(\theta), \boldsymbol{D}(\alpha)]$ affords universal control over the qubit cavity space[90].

### Photon-number preserving unitaries

Next, we consider gates that leave the photon-number distribution in the cavity untouched; no cavity pulse is played $\epsilon(t) = 0$. These gates consist of qubit pulses that leverage geometrical phases and the photon number-dependent frequency shift the qubit experiences to impart arbitrary phases onto the different Fock state components of the cavity state. These gates are called Selective-Number Arbitrary-Phase (SNAP) gates [91], and their general unitary can be written as:

$$\boldsymbol{U}_{\text{SNAP}} = \sum_{n=0}^{N} e^{i\theta_n} |n\rangle \langle n| \tag{2.65}$$

To clarify how this unitary is implemented, let's first consider the case of a single Fock state component $e^{i\phi_m} |m\rangle \langle m|$. The qubit frequency is shifted through the m-photons to $\omega_q - m\chi$. If we play a Gaussian $\pi$-Pulse at this frequency with a sufficiently narrow bandwidth $1/2\pi\sigma_t < \chi$, we will only flip the qubit associated with the cavity photon number state $|m\rangle$. This is what we refer to as a selective $\pi$ pulse. By playing two selective $\pi$-Pulses back-to-back with different phases, the qubit state will follow a closed trajectory on the Bloch sphere and pick up a Berry phase. $|g, m\rangle \to e^{i\theta} |g, m\rangle$. To implement Equation 2.65, we have to play multiple selective $\pi$-pulses with the frequencies $\omega_q - n\chi, n \in \mathcal{N}$ in parallel.

The duration of SNAP gates is determined by the required spectral selectivity of the conditional $\pi$-Pulses and is therefore dependent on $\chi$, $t_{\text{SNAP}} \propto 1/\chi$. The SNAP gate in combination

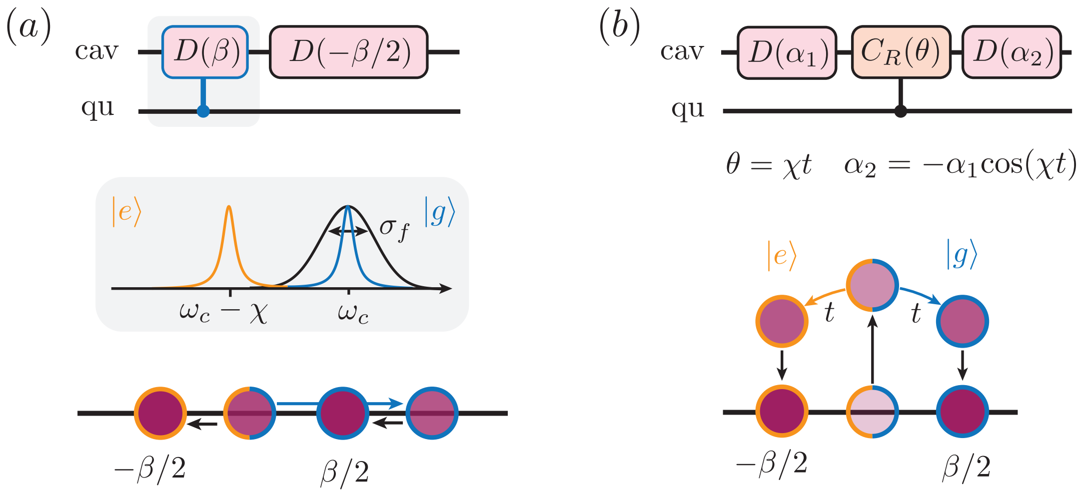

Figure 2.10: **Sequences to implement a conditional displacement** (a) Implementation of a conditional displacement gate using selective pulses. A selective displacement pulse with $\sigma_f > \chi$ (assuming a Gaussian pulse) is played in resonance with $\omega_c$, only displacing the cavity if the qubit is in $|g\rangle$. A second unselective displacement is used to kick it back. (b) Implementation of a conditional displacement utilizing the natural evolution of the oscillator. We first displace the cavity and then wait. Through the dispersive shift, the cavity for $|g\rangle$ and $|e\rangle$ evolves at different frequencies, resulting in a split. After the wait time, we proceed with another displacement to align the coherent states with a specific quadrature. The effective interaction strength scales with $\sim \chi|\alpha|$.

with displacements is a universal. [91].

### Conditional displacements

Assuming that our qubit does not start in an eigenstate of $\boldsymbol{\sigma}_z$, we can use a combination of cavity displacements $\boldsymbol{D}(\alpha)$ and the dispersive interaction to generate conditional displacement gates of the form:

$$\boldsymbol{CD}(\beta) = \boldsymbol{D}(\beta/2) \left|g\right\rangle \left\langle g\right| + \boldsymbol{D}(-\beta/2) \left|e\right\rangle \left\langle e\right| \tag{2.66}$$

There are two different methods to achieve this conditional displacements. The first approach utilizes spectral selectivity. We drive the cavity at a frequency $\omega_c$ (or $\omega_c - \chi$) with a sufficiently long pulse that will only displace the cavity if the qubit is in $|g\rangle$ (or $|e\rangle$). This scheme is shown in Fig. 2.10(a). If we choose $\beta$ as the displacement amplitude of the first pulse and follow up with an unconditional $\boldsymbol{D}(-\beta/2)$ displacement, we achieve $\boldsymbol{CD}(\beta)$. Once again, the gate time is imposed by the spectral selectivity and scales with $1/\chi$.

The second approach utilizes the qubit state-dependent rotation of cavity states to achieve separation, as shown in 2.10 (b). We first play a displacement, followed by a wait time, and another displacement. This gives an effective conditional displacement amplitude

$$\beta = i\alpha \sin(\chi t) \approx i\alpha\chi t \tag{2.67}$$

where the approximation is made for small $\chi t$. This reveals a key insight. For fixed $\beta$, we can trade off $\alpha$ and $t$, resulting in an effective interaction time

$$t_{cd} \propto \frac{1}{|\alpha|\chi} \tag{2.68}$$

This technique is also known as Hamiltonian amplification [90, 92]. It refers to the amplification of non-linear interactions through displacements or squeezing. To gain a better understanding, let us first consider how the displacement operator transforms $\boldsymbol{a}$:

$$\boldsymbol{D}^\dagger(\alpha)\boldsymbol{a}\boldsymbol{D}(\alpha) = \boldsymbol{a} + \alpha \tag{2.69}$$

$$\boldsymbol{D}^\dagger(\alpha)\boldsymbol{a}^\dagger\boldsymbol{D}(\alpha) = \boldsymbol{a}^\dagger + \alpha^* \tag{2.70}$$

With this, we can calculate how the dispersive Hamiltonian is affected when a displacement is applied before and after. Note that I omit the qubit/bosonic operator if it is the identity.

$$\boldsymbol{D}^\dagger(\alpha)\left(-\frac{\chi}{2}\boldsymbol{a}^\dagger\boldsymbol{a}\boldsymbol{\sigma}_z\right)\boldsymbol{D}(\alpha) = -\frac{\chi}{2}(\alpha\boldsymbol{a}^\dagger + \alpha^*\boldsymbol{a})\boldsymbol{\sigma}_z - \frac{\chi}{2}\boldsymbol{a}^\dagger\boldsymbol{a}\boldsymbol{\sigma}_z - \frac{\chi}{2}|\alpha(t)|^2\boldsymbol{\sigma}_z \tag{2.71}$$

The first term provides the desired conditional displacement term amplified by $\alpha$. The remaining terms represent an unwanted cavity rotation and qubit phase accumulation. These spurious effects can be suppressed using a combination of flipping the displacement signs throughout the sequence and playing a qubit $\pi$ pulse in the middle. The gate implementing this is known as Echo Conditional Displacement (ECD) [46, 90] and is heavily utilized in this thesis. It will be detailed in the following Chapter.

### Sideband drives

Another powerful tool in the cQED toolbox is the four-wave mixing capability of the Josephson junction unlocked by sideband drives. Among other things, it can be used to implement a two-mode squeezing or beam-splitter Hamiltonian. Although this type of interaction is not utilized in this thesis, it is too important to overlook. I recommend the PhD thesis of Steven

Touzard [93] for more details. The following discussion is a brief outline of the derivation given in his thesis.

We start with the Hamiltonian of a driven nonlinear mode $\boldsymbol{a}$ coupled to linear mode $\boldsymbol{b}$. In the derivation of the dispersive interaction, we already found (see 2.50) that we can write this Hamiltonian as

$$\frac{\boldsymbol{H}}{\hbar} = \omega_a \boldsymbol{a}^\dagger \boldsymbol{a} + \omega_b \boldsymbol{b}^\dagger \boldsymbol{b} + \epsilon(t)\boldsymbol{a}^\dagger + \epsilon^*(t)\boldsymbol{a} + \frac{\boldsymbol{H}_{4+}}{\hbar}(\varphi_a^{\mathrm{ZPF}}\left(\boldsymbol{a}+\boldsymbol{a}^\dagger\right) + \varphi_b^{\mathrm{ZPF}}\left(\boldsymbol{b}+\boldsymbol{b}^\dagger\right)) \tag{2.72}$$

with $\varphi_b^{\mathrm{ZPF}} = \varphi_a^{\mathrm{ZPF}}\frac{g}{\Delta}$. The key insight here is that through several smart frame transformations and approximations, we can effectively move the drive into the non-linear term. Note that we also moved into the rotation frame of a and b, warranting the transformation $\boldsymbol{a} \to \boldsymbol{a}e^{-i\omega_a t}$, $\boldsymbol{b} \to \boldsymbol{b}e^{-i\omega_b t}$. With this, the non-linear term can be written as

$$\boldsymbol{H}_{4+}\left(\varphi_a^{\mathrm{ZPF}}\left(\boldsymbol{a}e^{-i\omega_a t} + \boldsymbol{a}^\dagger e^{i\omega_a t}\right) + \varphi_a\left(\xi_0 e^{i\omega t} + \xi_0^* e^{-i\omega t}\right) + \varphi_b^{\mathrm{ZPF}}\left(\boldsymbol{b}e^{-i\omega_b t} + \boldsymbol{b}^\dagger e^{i\omega_b t}\right)\right) \tag{2.73}$$

with $\xi = \frac{\epsilon}{\Delta}$ and $\Delta = \omega_a - \omega$. In this form, it is easy to see that expanding this drive to fourth order gives rise to a multitude of new terms. Most of these terms will oscillate at an effective frequency that is large compared to the system's default dynamics and are removed under the RWA. It is, however, possible, through a smart choice of drive frequency, to unlock new interactions that were previously impossible.

Consider, for example, the case when $\omega = (\omega_a + \omega_b)$. In this case, a new Hamiltonian survives the RWA:

$$\begin{aligned} \frac{\boldsymbol{H}_{\mathrm{tms}}}{\hbar} =& \frac{E_J}{4!}\binom{4}{2}\binom{2}{1}\varphi_a^3\varphi_b(\xi_0^*(t)^2\boldsymbol{a}\boldsymbol{b} + \xi_0(t)^2\boldsymbol{a}^\dagger\boldsymbol{b}^\dagger) & (2.74) \\ =& \sqrt{2K_a\chi_{ab}}|\xi_0(t)|^2(e^{i2\phi_0(t)}\boldsymbol{a}\boldsymbol{b} + e^{-i2\phi_0(t)}\boldsymbol{a}^\dagger\boldsymbol{b}^\dagger) & (2.75) \end{aligned}$$

where I used $K/2 = E_J\phi_a^4$ and $\chi = E_J\phi_a^2\phi_b^2$ and $\xi_0(t) = |\xi_0(t)|e^{i\phi_0(t)}$. This Hamiltonian implements a two-mode squeezing operation.

Another prominent example is the beamsplitter Hamiltonian. It is implemented between two linear modes $\boldsymbol{b}, \boldsymbol{c}$ that are coupled to the same transmon mode $\boldsymbol{a}$. Applying two drives $\epsilon_1, \epsilon_2$ at the frequency matching condition $|\omega_1 - \omega_2| = |\omega_c - \omega_b|$ yields the Hamiltonian [94]:

$$\frac{\boldsymbol{H}_{bs}}{\hbar} = \sqrt{\chi_{ab}\chi_{ac}}\xi_1(t)\xi_2(t)(e^{i\varphi}\boldsymbol{b}\boldsymbol{c}^\dagger + e^{-i\varphi}\boldsymbol{b}^\dagger\boldsymbol{c}) \tag{2.76}$$

where $\varphi$ is determined by the relative phase of the two drives.

This brief discussion overlooks much of the complexity involved in designing a system to use parametric drives. While transmons can provide these interactions, they are far from ideal for this purpose. The mixing capabilities do not arise from a dedicated fourth-order nonlinearity, but rather from the indiscriminate cosine potential that generates mixing terms at all even orders. Besides leading to always-on terms like $\chi$ and inherited self-Kerr, many unwanted processes emerge at higher drive powers, fundamentally limiting both fidelity and achievable gate speeds. In Gao et. al. [94], the effective drive strengths to generate the beam splitter are $\xi_1, \xi_2 = 0.1$, limiting the speed of the interaction to $g_{bs} \approx 34\,\mathrm{kHz} \ll \chi \approx 1\,\mathrm{MHz}$.

Consequently, studying other hardware choices for parametric drive designs is an active field of research. Two prominent examples are the Superconducting Nonlinear Asymmetric Inductive Element (SNAIL) [95] and the Linear Inductive Coupler (LINC) [96]. Both elements are three-wave mixers where the third-order nonlinearity generates the desired mixing process. At the same time, the fourth-order term can be nulled, effectively suppressing AC Stark shifts and unwanted frequency collisions. While the SNAIL provides Kerr-free operation, the LINC emerged as a further advancement by combining this capability with engineered selection rules that make it essentially linear when idle. The LINC's balanced drive architecture and inherent symmetries enable clean parametric processes even at high drive strengths.

## 2.5 Summary

In this chapter, we introduced the fundamental building blocks of bosonic circuit QED: the QHO and the transmon. We explored their theoretical description, as well as their physical implementation, and how these elements can be coupled in the dispersive regime.

We then explored how the dispersive regime enables QND readout of the qubit state and examined a comprehensive suite of control techniques, ranging from simple qubit gates and displacements to conditional pulses, sideband drives, and Hamiltonian amplification methods. A common thread among these control techniques is that the duration of entangling gates scales directly with $\sim 1/\chi$. However, large $\chi$ values required for fast operations induce unwanted oscillator nonlinearity that degrades quantum states extending further out in phase space. States like squeezed states and cat states, which require precise nonlinear dynamics for their preparation and preservation, become increasingly sensitive to this inherited Kerr nonlinearity as they occupy larger regions of phase space.

To harness these states, a paradigm shift toward weak dispersive coupling is necessary, where $\chi$ is reduced by over an order of magnitude to minimize oscillator nonlinearity. Yet this regime presents formidable technical challenges. Traditional control and measurement techniques become impractically slow when $\sim 1/\chi$ approaches qubit decoherence rates, and standard calibration methods designed for stronger dispersive coupling fail. We identified one technique dubbed Hamiltonian amplification that helps to bridge this gap. Using large phase-space displacements $\alpha_0$, we showed that we can implement conditional displacement with an effective interaction rate $\sim \alpha_0\chi$

Chapter 3 addresses these challenges by discussing the weak-coupling dispersive architecture, which overcomes the limitations identified here. We discuss the Swiss army knife of this coupling regime, the echo-conditional displacement gate, and explain how it is utilized for control and to perform direct characteristic function tomography of the cavity state. These techniques form the foundation on which the main experiments of this thesis are built.

# Chapter 3

# Operating in the weak dispersive coupling regime

Experiments in bosonic circuit cQED have demonstrated a remarkable level of control over the qubit oscillator space, like the creation of two-mode entangled states [97], crossing the break-even point with bosonic codes [52, 53], and metrology applications [67]. However, most of these demonstrations relied on operating in the strong dispersive coupling regime, where the $\chi$ between qubit and oscillator is much larger than the oscillator's linewidth $\kappa$, usually of the order of $\sim 1\,\mathrm{MHz}$.

While the strong coupling regime offers certain advantages, such as a fast and rich set of operations, it also comes with fundamental limitations. Most critically, the oscillator inherits significant Kerr nonlinearity from coupling to the transmon. This inherited Kerr effect can be beneficial in certain applications [98], yet it severely restricts our ability to prepare and manipulate states that extend slightly further into phase space and are sensitive to anharmonicity, such as cat states and squeezed states. Moreover, strong coupling introduces other unwanted effects that limit system performance. The reverse Purcell effect reduces oscillator lifetimes by coupling the high-$Q$ storage mode to the lossy transmon. Furthermore, large photon populations in the oscillator can cause the transmon to Stark-shift into resonance with spurious two-level systems, thereby degrading coherence.

This motivates a shift toward the weak dispersive coupling regime [46, 53, 99, 100], where $\chi$ is reduced by more than an order of magnitude to approximately 30-100 kHz. The central challenge in weak coupling is that traditional control and measurement techniques become impractically slow as $\chi/2\pi$ becomes comparable to qubit decoherence rates. This challenge is addressed by Hamiltonian amplification, allowing the implementation of conditional displacements at an effective interaction rate $|\alpha|\chi$. This enables trading larger displacement amplitudes for shorter gate durations while benefiting from dramatically reduced nonlinearity and extended coherence.

This chapter develops the theoretical foundation and experimental implementation of the ECD gate, the main workhorse of the low-dispersive coupling regime. I will begin the discussion by assuming instantaneous gates and then proceed to incorporate finite-duration pulses, where numerical optimization becomes crucial to achieve high-fidelity ECD gates. With the theory established, I will proceed to discuss how we characterize the Hamiltonian in the low-dispersive coupling regime and how we tune up the ECD gate and measure the characteristic function, our primary tomography tool. Parts of this discussion will follow the comprehensive treatment found in Alec Eickbusch's PhD thesis [90].

## 3.1 Echo conditional displacement gate

The ECD gate is implemented through an interplay of the dispersive Hamiltonian and a cavity drive played at frequency $\omega_c - \chi/2$. The Hamiltonian in the rotating frame of the drive is given by:

$$\frac{\boldsymbol{H}_{\text{ECD}}}{\hbar} = -\frac{\chi}{2}\boldsymbol{a}^\dagger\boldsymbol{a}\boldsymbol{\sigma}_z + \varepsilon^*(t)\boldsymbol{a} + \varepsilon\boldsymbol{a}^\dagger \tag{3.1}$$

We saw in section 2.4.2 how this Hamiltonian can implement a conditional displacement. In particular, sandwiching the dispersive Hamiltonian between two displacements gives rise to a conditional displacement term, along with spurious cavity rotation and qubit phase accumulation, as shown in Equation 2.71. The ECD sequence, depicted in Fig.3.1 (a), is designed to cancel out these two spurious terms while keeping the conditional displacement.

The sequence cancels the spurious terms through the action of two echoing techniques. A phase-space echo via displacements with alternating signs, and a qubit echo via a $\pi$-pulse at the sequence midpoint. The desired conditional displacement term experiences both sign flips and survives, while the unwanted terms each experience only one echo and are thus canceled.

Fig.3.1 (b) visualizes the evolution of the first two gates in the ECD sequence. The first displacement pulse defines the length of the arm that the dispersive interaction rotates.

The phase-space trajectory of the ECD sequence, under the assumption of instantaneous gates, is depicted in Fig. 3.1 (c). The first displacements $\alpha_1$ bring us far out in phase space. The wait time $t_\text{w}$ entangles the qubit and cavity as the dispersive interaction leads to a qubit state-dependent phase pick-up. Next is the double echo sequence. Two displacements mirror the coherent states along $\text{Re}(\alpha)$ to the opposite side in phase space, while the qubit is flipped between the two displacements. Finally, after another wait time $t_\text{w}$, the coherent states are

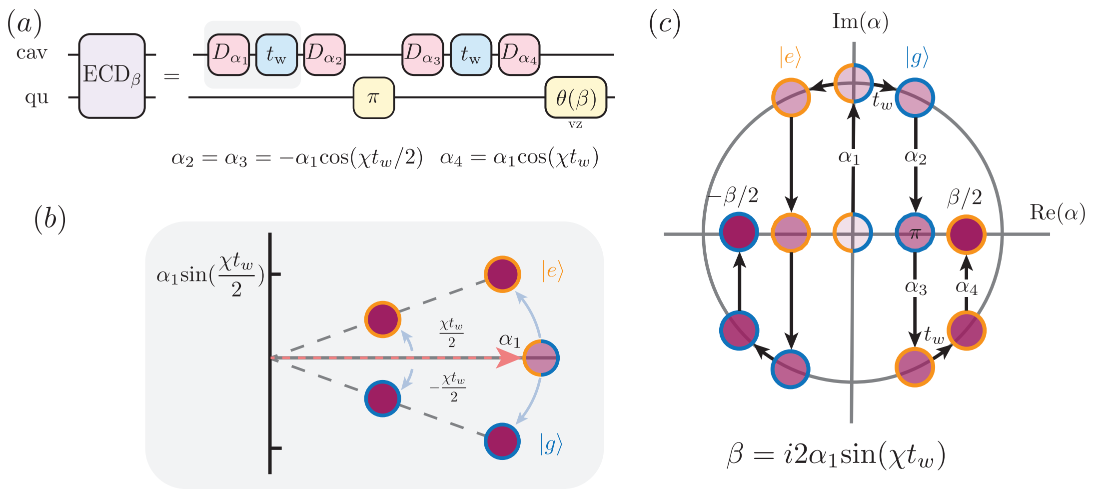

Figure 3.1: **Sequence to implement the ECD gate.** (a) The first displacement drives the resonator far out in phase space. The subsequent wait time then accumulates a qubit state-dependent phase. The next two displacements, along with the qubit $\pi$-pulse, flip the signs of the coherent states and time evolution. After another wait time, a last displacement achieves the conditional displacement. A final virtual z rotation counters the accumulated geometric phase on the qubit. (b) Displacements can be used as a lever in phase space to increase the angular velocity. A longer lever translates into a larger conditional displacement. (c) The phase space trajectory of an ECD gate, assuming instant gates. The amplitudes of the four displacement pulses are scaled to achieve a conditional displacement $\beta$ without any offset. A displacement amplitude $\alpha_1$ and a wait time of $t_\mathrm{w}$ yield a conditional displacement with $\beta = 2i\alpha_1 \sin(\chi t_w)$.

displaced back onto the $\mathrm{Re}(\alpha)$ axis. Through simple algebra, we can connect the achieved conditional displacement $\beta$ to $\alpha_1$ and $t_\mathrm{wait}$ as $\beta = i2\alpha_1 \sin(\chi t_w)$.

While this discussion accurately describes the phase space trajectory, it neglects a geometrical qubit phase $\theta$ that is acquired as a result of the phase space trajectory. Taking this into account, we can write the unitary of the ECD gate with instantaneous gates as:

$$\boldsymbol{U} = \boldsymbol{\sigma}_x e^{i\theta\boldsymbol{\sigma}_z} \boldsymbol{C}\boldsymbol{D}(\beta) \tag{3.2}$$

where $\sigma_x$ captures the qubit flip, $\theta$ is the acquired qubit phase and $\beta$ the achieved conditional displacement.

However, while the instantaneous gate analysis helps to build intuition, realistic implementations must take into account the finite duration of the pulses. As a result, the coherent states will also rotate during the four displacement gates, leading to distortions compared to the trajectory depicted in Figure. 3.1(c). These distortions will lead to a deviation from the targeted conditional displacement, as well as an overall unconditional displacement. Thus, we have to adjust Equation 3.2 to capture the whole process.

$$\boldsymbol{U} = \boldsymbol{\sigma}_x e^{i\theta' \boldsymbol{\sigma}_z} \boldsymbol{D}(\lambda) \boldsymbol{CD}(\beta) \tag{3.3}$$

where we introduced $D(\lambda)$ to capture the unconditional displacement and changed $\theta$ to $\theta'$ to account for the geometrical phase picked up between $\boldsymbol{D}(\lambda)$ and $\boldsymbol{CD}(\beta)$.

Given an ECD pulse $\varepsilon(t)$, we can find the parameters $\theta'$, $\lambda$, and $\beta$ by integrating the Schrödinger equation over the whole sequence length $T$. A detailed derivation of the following equations based on Ref. [99] can be found in Appendix A.

$$\theta(t) = -2 \int_0^t d\tau \, \mathrm{Re}[\varepsilon^*(\tau)\delta(\tau)] \tag{3.4}$$

$$\gamma(t) = -i \int_0^t d\tau \cos[\phi(\tau) - \phi(t)]\varepsilon(\tau) \tag{3.5}$$

$$\delta(t) = -\int_0^t d\tau \sin[\phi(\tau) - \phi(t)]\varepsilon(\tau) \tag{3.6}$$

$$\phi(t) = -\frac{\chi}{2} \int_0^t d\tau \, z(\tau) \tag{3.7}$$

From these equations, we find $\beta = 2\delta(T)$, $\lambda = \gamma(T)$, $\theta' = \theta(T) + 2\mathrm{Im}(\delta(T)\gamma(T))$. The additional parameter $\phi(t)$ corresponds to an overall cavity rotation and is canceled as a result of applying a $\pi$-pulse in the middle of the sequence.

To achieve high-fidelity ECD gates, we have to null the unwanted displacement $\lambda$, ensure that we achieve the wanted $\beta$, and correct the accumulated qubit phase through virtual $\boldsymbol{\sigma}_z$ rotations. Furthermore, higher-order Hamiltonian terms, such as the second-order dispersive shift $\chi'$ and the inherited oscillator nonlinearity $K$, can also affect gate performance at large displacement amplitudes, as their impact scales with the photon number squared.

The strategy to counter unwanted displacement, ensure the correct $\beta$, and account for higher-order Hamiltonian terms is to optimize the phase space trajectory [90]. To keep the number of optimization parameters manageable, we impose that $\varepsilon$ is of fixed form shown in the Figure. 3.1(a), where all gates either Gaussian or constant pulses with a cosine ramp up. The length of the pulses is system dependent, but the aim is to keep them as fast as possible. With this fixed form, we parametrize $\varepsilon$ in terms of a default pulse amplitude $\varepsilon_0$ and the ratio of the first to the second, third and fourth pulses, $r_2, r_3, r_4$, as well as the wait time $t_\mathrm{w}$.

For efficient optimization, we utilize the semiclassical trajectories that describe the phase space trajectory of the coherent state during the sequence. Note that these trajectories are derived in more detail in the next section, when discussing the displace frame transformation.

$$\partial_t \alpha_g(t) = -i\Delta\alpha_g(t) + 2iK|\alpha_g(t)|^2\alpha_g(t) - \frac{\kappa}{2}\alpha_g(t) - i\varepsilon(t) \tag{3.8}$$

$$\partial_t \alpha_e(t) = -i\Delta\alpha_e(t) + 2iK|\alpha_e(t)|^2\alpha_e(t) - \frac{\kappa}{2}\alpha_e(t) - i\varepsilon(t) + i(\chi + 2\chi'|\alpha_e(t)|^2)\alpha_e(t) \tag{3.9}$$

For a given pulse sequence $\varepsilon(t)$, we solve these trajectories and use a Nelder-Mead based optimizer to find the ideal set of values for $\{\varepsilon_0, r_2, r_3, r_4\, t_{\text{wait}}\}$ that achieves a target conditional displacement $\beta$ with intermediate phase space radius $\alpha_0$ in the shortest time $t_{\text{w}}$. Further details regarding the exact cost function and implementation can be found in Ref. [90].

In the first part of this chapter, we described how we can practically implement an ECD gate. However, before running experiments, we first want to simulate our sequence to test its feasibility or the impact of different decoherence mechanisms. The large displacements in the ECD sequence quickly become computationally too expensive to simulate, as they require a high cutoff frequency. As such, naive numerical simulations are doomed to failure. We address this challenge in the next section by introducing the displaced frame transformation, a crucial technique that allows efficient simulation of the ECD gate. The core idea is to move into a frame that follows the large unconditional displacements and focuses on the smaller conditional displacements, allowing a significant decrease in the required Hilbert space cutoff dimension.

## 3.2 Displaced frame transformation

The idea of a frame transformation is to change our perspective, focusing on the evolution of interest while disregarding the trivial part. In the context of quantum control involving large coherent state displacements, direct simulation and optimization in the laboratory frame can be computationally intractable due to the vast Hilbert space required for accurate truncation. The displaced frame addresses this by allowing for efficient simulation and optimization of operations involving large photon numbers. This is particularly crucial for systems operating in the low-dispersive coupling regime, where operations often rely on significant displacements to enhance effective interaction rates [99].

In the ECD sequence, for instance, we are primarily interested in the effective conditional displacements arising from the dispersive interaction, rather than the trivial unconditioned displacements enacted by the drive. This can be achieved by moving into a time-dependent displaced frame defined by the unitary transformation $\boldsymbol{U}(t) = \boldsymbol{D}(\alpha(t)) = e^{\alpha^*(t)\boldsymbol{a}-\alpha(t)\boldsymbol{a}^\dagger}$, which tracks the drive-induced evolution. The following derivation follows [90].

As a starting point, we consider the dispersive Hamiltonian, including the second-order dispersive shifts $\chi'$ and the inherited oscillator anharmonicity $K$. We work in the rotating frame of the qubit and ignore the qubit drive as it is unaffected by this frame transformation.

$$\frac{\boldsymbol{H}}{\hbar} = \Delta\boldsymbol{a}^\dagger\boldsymbol{a} - \chi\boldsymbol{a}^\dagger\boldsymbol{a}\boldsymbol{q}^\dagger\boldsymbol{q} - \chi'\boldsymbol{a}^{\dagger 2}\boldsymbol{a}^2\boldsymbol{q}^\dagger\boldsymbol{q} - K\boldsymbol{a}^{\dagger 2}\boldsymbol{a}^2 - \alpha\boldsymbol{q}^{\dagger 2}\boldsymbol{q}^2 + \epsilon(t)\boldsymbol{a}^\dagger + \epsilon^*(t)\boldsymbol{a} \tag{3.10}$$

where $\Delta$ is the detuning of the cavity drive frequency and the cavity's resonant frequency. For the ECD, usually chosen to be $\Delta = \frac{\chi}{2}$. To move into the displaced frame, we have to transform this Hamiltonian according to the rule

$$\tilde{\boldsymbol{H}} = \boldsymbol{U}\boldsymbol{H}\boldsymbol{U}^\dagger + (i\hbar)(\partial_t\boldsymbol{U})\boldsymbol{U}^\dagger = \boldsymbol{D}^\dagger(\alpha(t))\boldsymbol{H}\boldsymbol{D}(\alpha(t)) + (i\hbar)(\alpha\partial_t\alpha^*(t) - \alpha^\dagger\partial_t\alpha(t)) \tag{3.11}$$

The lengthy calculation for this transformation can be performed using standard techniques, such as the Baker-Campbell-Hausdorff formula and commutator relations, leading to a transformed Hamiltonian in the displaced frame.

$$\begin{aligned}\frac{\tilde{\boldsymbol{H}}}{\hbar} = {} & \Delta\boldsymbol{a}^\dagger\boldsymbol{a} - \left(\Delta\alpha^* - 2K|\alpha|^2\alpha^* + i(\partial_t\alpha^*) + i\frac{\kappa}{2}\alpha^* + \epsilon^*\right)\boldsymbol{a} + h.c. \\ & - (\chi + 4\chi'|\alpha|^2)\boldsymbol{a}^\dagger\boldsymbol{a}\boldsymbol{q}^\dagger\boldsymbol{q} - \chi'\boldsymbol{a}^{\dagger 2}\boldsymbol{a}^2\boldsymbol{q}^\dagger\boldsymbol{q} - K\boldsymbol{a}^{\dagger 2}\boldsymbol{a}^2 - K_q\boldsymbol{q}^{\dagger 2}\boldsymbol{q}^2 \\ & - (\chi + 2|\alpha|^2\chi')(\alpha^*\boldsymbol{a} + \alpha\boldsymbol{a}^\dagger)\boldsymbol{q}^\dagger\boldsymbol{q} \\ & - (\chi|\alpha|^2 + \chi'|\alpha|^4)\boldsymbol{q}^\dagger\boldsymbol{q} - 4K|\alpha|^2\boldsymbol{a}^\dagger\boldsymbol{a} + \\ & - K\left(2\alpha\boldsymbol{a}^{\dagger 2}\boldsymbol{a} + \alpha^2\boldsymbol{a}^{\dagger 2} + h.c.\right) - \chi'\left(2\alpha\boldsymbol{a}^{\dagger 2}\boldsymbol{a} + \alpha^2\boldsymbol{a}^{\dagger 2} + h.c.\right)\boldsymbol{q}^\dagger\boldsymbol{q}\end{aligned} \tag{3.12}$$

Note that we have included the deterministic decay of the cavity at the rate $\kappa$.

We have not yet specified the actual trajectory that our displaced frame $\alpha(t)$ follows. To cancel the unconditional trajectory of the oscillator, we look to cancel the terms only associated with $\boldsymbol{a}$. This is achieved by choosing our frame to track a trajectory that fulfills the classical Langevin equation:

$$\partial_t\alpha(t) = -i\Delta\alpha(t) + 2iK|\alpha(t)|^2\alpha(t) - \frac{\kappa}{2}\alpha(t) - i\epsilon(t) \tag{3.13}$$

This equation accounts for the trivial evolutions of the cavity mode, including the detuning from resonance $\Delta$, the impact of the inherited Kerr nonlinearity $K$, the deterministic re-centering due to photon loss $\kappa$, and the effect of the drive $\epsilon(t)$. If we start from vacuum, we set $\alpha(0) = 0$.

For simulation purposes, it is helpful to rewrite the Hamiltonian in terms of dependencies on the different orders of $\alpha$. Assuming that our frame fulfills the above equation, we arrive at the final form of the Hamiltonian that I use in this thesis for displaced frame simulations with the transmon truncated to the second level:

$$\begin{aligned}
\tilde{H} = {} & \Delta \boldsymbol{a}^\dagger \boldsymbol{a} - \chi_e \boldsymbol{a}^\dagger \boldsymbol{a} |e\rangle\langle e| - \chi_e' \boldsymbol{a}^{\dagger 2} \boldsymbol{a}^2 |e\rangle\langle e| - K \boldsymbol{a}^{\dagger 2} \boldsymbol{a}^2 \\
& + \left(-4 \boldsymbol{a}^\dagger \boldsymbol{a} \chi_e' |e\rangle\langle e| - \chi_e |e\rangle\langle e| - 4K \boldsymbol{a}^\dagger \boldsymbol{a}\right) |\alpha|^2 \\
& + \left(-\chi_e' |e\rangle\langle e|\right) |\alpha|^4 \\
& + \left(-2\chi_e' |e\rangle\langle e| \boldsymbol{a}^\dagger\right) |\alpha|^2 \alpha + h.c. \\
& + \left(-K \boldsymbol{a}^{\dagger 2} - \chi_e' |e\rangle\langle e| \boldsymbol{a}^{\dagger 2}\right) \alpha^2 + h.c. \\
& + \left(-\chi_e |e\rangle\langle e| \boldsymbol{a}^\dagger - 2K \boldsymbol{a}^{\dagger 2} \boldsymbol{a} - 2\chi_e' |e\rangle\langle e| \boldsymbol{a}^{\dagger 2} \boldsymbol{a}\right) \alpha + h.c.
\end{aligned}$$

Simulating in the displaced frame then follows these simple steps:

1. Given a cavity drive sequence $\varepsilon(t)$, calculate the displaced frame $\alpha(t)$ by solving Equation 3.13
2. Use $\alpha(t)$ and the Hamiltonian parameters to setup the displaced frame Hamiltonian
3. Run the simulation and move back into the labframe by applying $\boldsymbol{D}(-\alpha[-1])$ to the final state.

where $\boldsymbol{D}(\alpha[-1])$ refers to the final $\alpha$ value of the displaced frame.

Previously, when discussing the ECD, we concluded that we have to optimize the phase-space trajectories for finite gate times to achieve high-fidelity gates. For this, we have needed the phase-space trajectory of the oscillator for the qubit in $|g\rangle$ and $|e\rangle$, including the experienced conditional displacement. Assuming $\Omega(t) = 0$, we can project the qubit into $|g\rangle$ or $|e\rangle$. As a result, the third line in eq. 3.12 that generates the conditional displacement is now only dependent on $\boldsymbol{a}$. Like for the displaced frame, we can find the corresponding phase-space trajectories by solving the Langevin equations:

$$\partial_t \alpha_g(t) = -i\Delta\alpha_g(t) + 2iK|\alpha_g(t)|^2\alpha_g(t) - \frac{\kappa}{2}\alpha_g(t) - i\epsilon(t) \tag{3.14}$$

$$\partial_t \alpha_e(t) = -i\Delta\alpha_e(t) + 2iK_s|\alpha_e(t)|^2\alpha_e(t) - \frac{\kappa}{2}\alpha_e(t) - i\epsilon(t) + i(\chi + 2\chi'|\alpha_e(t)|^2)\alpha_e(t) \tag{3.15}$$

We utilize these trajectories to efficiently optimize the phase-space trajectory of the ECD pulse sequence, thereby achieving the desired conditional displacement $\beta$ while minimizing the spurious displacement $\lambda$.

Finally, it is essential to consider how loss changes when we move our simulation into the displaced frame. Neatly, photon loss is not amplified in the displaced frame. This is because our displaced frame $\alpha(t)$ is specifically chosen to incorporate the deterministic re-centering force $\frac{\kappa}{2}\alpha(t)$ that arises from photon loss in the displaced frame. With this choice of drive, the deterministic evolution is fully accounted for. Thus, relaxation in the displaced frame is not enhanced compared to relaxation at the origin of phase space.

However, dephasing noise is amplified and dominated by rates scaling as $2\kappa_\phi|\alpha(t)|^2$. This leads to diffusion-like terms in the master equation, resulting in an enhanced rate of dephasing that scales quadratically with the displacement amplitude $\alpha$. This amplification highlights a crucial trade-off between gate speed and enhanced dephasing. While larger displacements enable faster operations and reduce the impact of transmon errors and oscillator relaxation, they concurrently increase the effective dephasing rate of the oscillator. This trade-off is explicitly analysed for state preparation in Section 4.6.4 of Alec Eickbusch's PhD thesis [90].

## 3.3 System tune-up

Standard control techniques that rely on a $\chi$ induced phase pick up, or conditional rotations to probe the population of cavity Fock states, are unfeasible in the low dispersive coupling regime, where the dispersive shift $\chi$ is comparable to or smaller than the qubit decoherence rates. To address this, we leverage Hamiltonian amplification to effectively amplify the strength of small Hamiltonian terms, thereby enabling robust system characterization and the calibration of control pulses.

The tune-up process involves several key steps. I will first introduce the "out-and-back" method, a crucial tool to fine-tune the cavity frequency $\omega_c$ and accurately find small Hamiltonian parameters, such as the dispersive coupling $\chi$, the second-order dispersive shift $\chi'$, and the inherited Kerr nonlinearity $K$ [90]. With knowledge about the Hamiltonian, we can tune up ECD gates and measure the characteristic function, our primary tomography tool. Finally, I will present two novel experimental techniques developed in this work that utilize one-dimensional cuts of the characteristic function to measure coherent states and reliably determine the cavity $T_1$.

### 3.3.1 Measuring the Hamiltonian

System characterization in the low-dispersive coupling regime presents a difficult challenge. Most Hamiltonian parameters are small compared to qubit lifetimes. The out-and-back measurement solves this problem by utilizing large displacements to amplify the impact of these weak terms, allowing us to extract them.

The out-and-back sequence consists of four steps. First, a displacement creates a large coherent state in the cavity. Second, we wait for a time $t_\mathrm{w}$ during which the state accumulates a phase. We can predict this phase by only considering the rotation-inducing parts in the semi-classical trajectories see Equation 3.9):

$$\phi_g = \left(\Delta - 2K\alpha_0^2\right) t_\mathrm{w} \tag{3.16}$$

$$\phi_e = \left(\Delta - \chi - (2K + 2\chi')\alpha_0^2\right) t_\mathrm{w} \tag{3.17}$$

Third, we apply another displacement $\boldsymbol{D}(\alpha e^{i\phi})$, of which we sweep the phase $\phi$. This displacement will return the cavity to vacuum only if $\phi$ is opposite to the phase of the state in the cavity after the time evolution. Finally, a conditional $\pi$-pulse ($\sigma_t \approx 500\text{-}750$ ns) flips the qubit only if we returned the cavity to vacuum. We perform a post-selection measurement before playing the conditional $\pi$-pulse to remove data corrupted by transmon relaxation or heating.

Out-and-back comes in two different tastes. In the first variant, out and back amplitude, we fix the wait time $t_\mathrm{w}$ and sweep the amplitude $|\alpha|$ of both displacements and $\phi$ of the second displacement pulse as shown in Fig. 3.2 (a). Since $t_\mathrm{w}$ is constant, any measured slope in $\phi$ is caused by higher-order terms, as evident from Equation 3.17. Fig. 3.2 (b) shows exemplary results with $t_\mathrm{wait} = 1$ µs and the qubit initialized in $|e\rangle$.

This data exhibits the expected quadratic dispersion in $|\alpha|$, as predicted by the theoretical model. By performing this measurement twice, for qubit in $|g\rangle$ and $|e\rangle$, we can extract the four parameters $\Delta$, $\chi$, $K$ and $\chi'$. For each measurement, we fit Gaussians to the amplitude slices, thereby extracting two dispersion curves and then fitting these curves against Equation 3.17 [90].

For higher precision in $\Delta$ and $\chi$, we employ the out-and-back time sequence as shown in Fig. 3.2 (c). Instead of sweeping the amplitude $|\alpha|$ of our displacement pulses, we keep it small to render the contributions of $K$ and $\chi'$ negligible and isolate the contributions of $\Delta$ and $\chi$. We can extract them by sweeping the wait time $t_\mathrm{w}$. Exemplary data for the qubit starting in $|e\rangle$ is shown in Fig. 3.2 (d). Depending on the qubit state, it is straightforward to extract $\Delta$ ($|g\rangle$) and $\chi$ ($|e\rangle$) from the resulting linear dispersion curves. Together, these two approaches allow us

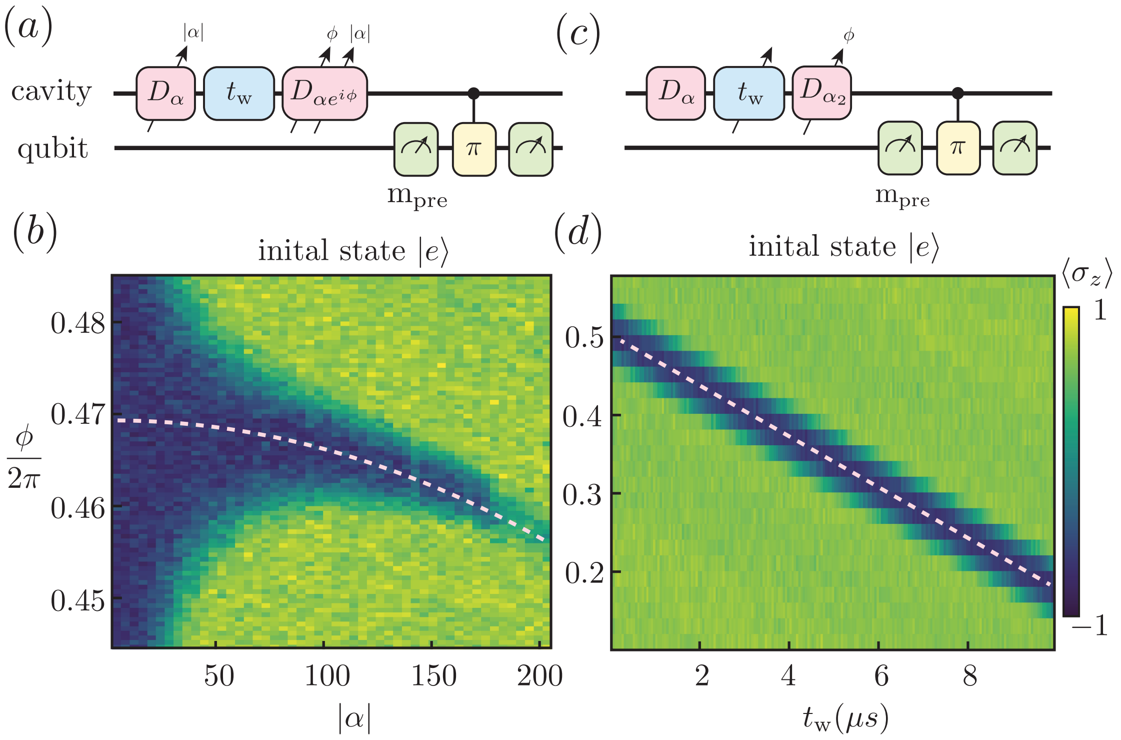

Figure 3.2: **Out and back experiments.** (a) Sequence of out and back amplitude sweep to find the Hamiltonian parameters. $\chi'$ and $K$ can be extracted by measuring and comparing the experiment for qubit in $|g\rangle$ and $|e\rangle$. (b) Measurement results of out-and-back amp for qubit in $|e\rangle$. The data follows a quadratic dispersion curve in $|\alpha|$ as expected from the theoretical model.(c) Sequence of out and back time. We use this measurement to fine-tune $\omega_c$ and $\chi$. (d) Measurement results for out-and-back time for qubit in $|e\rangle$. The data follows a linear slope from which we can extract $\chi$.

to fully characterize the dispersive Hamiltonian of the system, including $K$ and $\chi'$. In practice, we find that $K$ and $\chi'$ are mostly negligible in the $\alpha$ regimes we operate in.

At the beginning of this chapter, we introduced the sequence to implement the ECD gate and established that we have to optimize the ECD pulse sequence to achieve high-fidelity ECD gates. In the optimization, we require the Hamiltonian parameters, which we have a good understanding of after performing the out-and-back experiments. In the next section, we will discuss how we tune up ECD gates and measure the characteristic function.

### 3.3.2 Calibrating the ECD gate and characteristic function tomography

With knowledge of the Hamiltonian parameters, we can construct and optimize a pulse sequence that implements a desired ECD gate. In practice, we set the target unconditional displacement amplitude $\alpha_1$ and conditional displacement amplitude $\beta$, then run the optimizer [99] to yield the control parameters $\{\varepsilon_0, r_2, r_3, r_4, t_{\text{wait}}\}$. $\varepsilon_0$ is the amplitude of the pulse that implements $\alpha_1$, while $r_2$, $r_3$, $r_4$ are the amplitudes of the second, third and fourth displacement pulse relative to $\varepsilon_0$, and $t_{\text{wait}}$ is the wait time. The last missing piece to find is $\varepsilon_0$ in terms of the DAC amplitude. Conveniently, we can find this translation in the process of tuning up our primary tomography tool, the characteristic function. In fact, tuning up the characteristic function is synonymous with calibrating the ECD amplitude.

The characteristic function is defined as the expectation value of the displacement operators:

$$\mathcal{C}(\beta) = \langle \boldsymbol{D}(\beta) \rangle \tag{3.18}$$

The protocol we use to measure the characteristic function, illustrated in 3.3(a), consists of an ECD gate with amplitude $\beta$ inside a qubit Ramsey sequence. This sequence, up to the last $\pi/2$-pulse, essentially maps the expectation value of the displacement operator on the qubit $\langle \boldsymbol{\sigma}_x - i\boldsymbol{\sigma}_y \rangle = \langle \boldsymbol{D}(\beta) \rangle$. Thus, by varying the phase of the last $\pi/2$-pulse and measuring the qubit, we gain direct access to the real or imaginary part of $\mathcal{C}(\beta)$. Appendix B provides the corresponding derivation.

To minimize any spurious effects in the tomography sequence, we optimize an ECD gate with a target conditional displacement amplitude of $\beta = 3$ using a relatively modest displacement of $\alpha_1 = 6$. This parameter choice reflects two considerations: maintaining the displacements sufficiently small to minimize contributions from higher-order Hamiltonian terms, while ensuring $\beta$ remains large enough to provide adequate phase-space resolution for state characterization and reliable fitting, e.g., capturing Gaussian tails. Part of these considerations stem from the control electronics used, which, in our case, only allow a dynamical scale of a base DAC pulse from $0$ to $2$. Thus, with $\boldsymbol{ECD}(3)$ as our base gate, we can measure $\mathcal{C}(\beta)$ up to $|\beta| = 6$.

Tuning up the characteristic function consists of two parts. We need to establish the $\alpha_1$ and thus $\beta$ in terms of the DAC amplitude and find and correct the geometric phase the qubit acquires during the ECD sequence.

To find the DAC amplitude corresponding to $\varepsilon_0$, we measure the characteristic function of

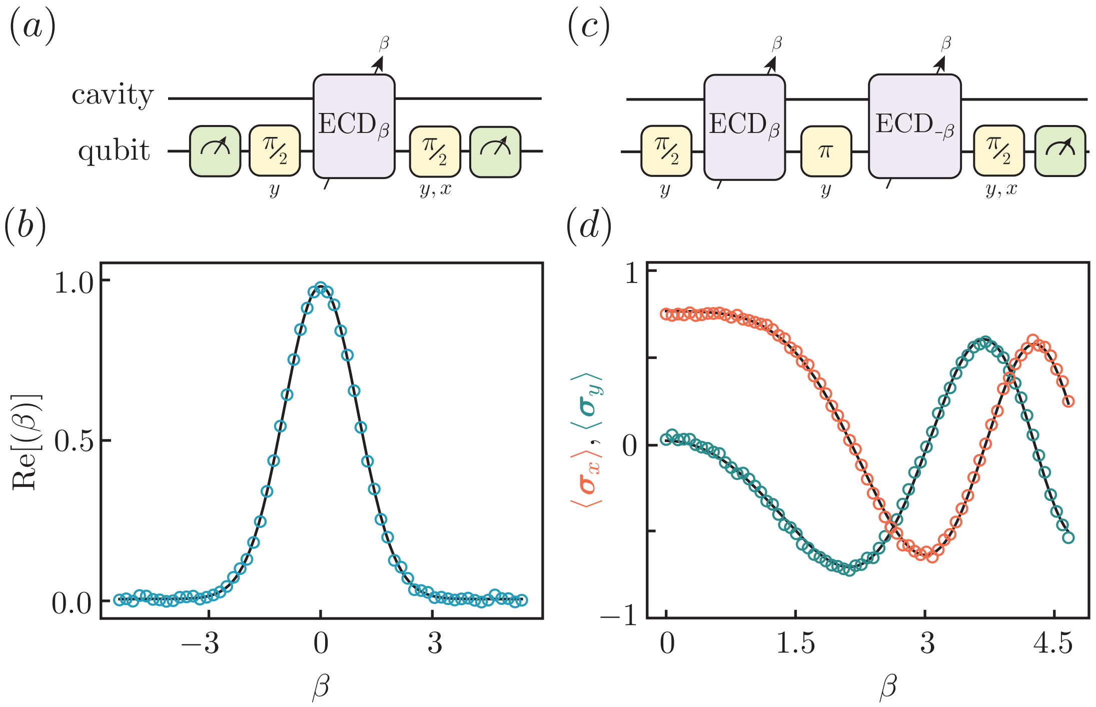

Figure 3.3: **ECD and characteristic function tune up experiments.** (a) Sequence to measure the characteristic function $\mathcal{C}(\beta)$. The phase of the final $\frac{\pi}{2}$ pulse determines if we measure the real or imaginary part of $\mathcal{C}(\beta)$. (b) Experimental data showing Re[$\mathcal{C}(\beta)$] of $|0\rangle$. We use this measurement to calibrate the conditional displacement amplitude. (c) Sequence of the cat and back measurement, used to measure the geometric phase-pick up during an ECD sequence. (d) Experimental data showing the result of a cat-and-back experiment. We use this experiment to calibrate the phase picked up by the qubit during the ECD sequence $e^{i\theta_0|\beta|^2}$.

vacuum, whose functional form is a Gaussian with $\sigma = 1$:

$$\mathcal{C}_{|0\rangle}(\beta) = e^{-\frac{|\beta|^2}{2}} \tag{3.19}$$

We start with an appropriate DAC amplitude (inferred from out-and-back amp measurements) and dynamically scale this amplitude from $0-2$. If our base DAC amplitude matches $\varepsilon_0$, we implement an ECD with $\beta = 3$ for a scaling factor of 1, resulting in a Gaussian with $\sigma = 1/3$. If we measure a different $\sigma$, we scale the base DAC amplitude accordingly. Once we measure $\sigma = 1/3$, we successfully tuned the scale of our characteristic function tomography, as well as $\beta$ and $\alpha_1$ in the process.

Next, we need to correct the geometric phase $\theta$ acquired during the ECD sequence. This phase results from the phase space trajectory of the oscillator and scales with the conditional displacement amplitude as $\theta = \theta_0|\beta|^2$ [99], where $\theta_0$ is the phase for $|\beta| = 1$. We measure this phase by employing the cat-and-back sequence shown in 3.3(c) [100]. The core of this sequence consists of an ECD gate that reaches out in phase-space, a $\pi$ flip, and another ECD gate that returns the cavity states to vacuum, essentially implementing the operation $\boldsymbol{\sigma}_x e^{i\theta_0|\beta|^2\boldsymbol{\sigma}_z}$.

We measure this phase by first initializing the qubit in a superposition, then playing

$$\boldsymbol{ECD}(\beta) - \boldsymbol{\pi} - \boldsymbol{ECD}(-\beta) \tag{3.20}$$

and finally measuring the expectation values of $\boldsymbol{\sigma}_y$ and $\boldsymbol{\sigma}_x$. We repeat this measurement while sweeping $\beta$ and fit the resulting curves against

$$\langle\boldsymbol{\sigma}_y\rangle = \sin(2\theta_0|\beta|^2)e^{-\eta\beta^2} \tag{3.21}$$

$$\langle\boldsymbol{\sigma}_x\rangle = \cos(2\theta_0|\beta|^2)e^{-\eta\beta^2} \tag{3.22}$$

to find $\theta_0$. The additional exponential factor $e^{-\eta\beta^2}$ models loss of qubit purity during the sequence as a contraction of the Bloch vector [100]. Measurement results along with the fit are shown in Fig. 3.3(d).

After calibration, we incorporate this phase in our tomography by adjusting the final qubit rotation axis in the characteristic measurement sequence in real-time.

### 3.3.3 Tracking coherent states and measuring cavity decay

Many experiments in this thesis, particularly those involving W-state generation in chapter 5, require precise creation and tracking of coherent states in phase space. To address this need, we developed the crosshair measurement technique, which enables a complete and efficient characterization of arbitrary coherent states through two orthogonal cuts in the complex plane of the characteristic function. The foundation of this approach lies in the analytic form of the characteristic function of a coherent state. For a coherent state $|\alpha\rangle$, the characteristic function is given by:

$$\mathcal{C}_{|\alpha\rangle}(\beta) = \langle\alpha|\,\boldsymbol{D}(\beta)\,|\alpha\rangle = e^{-\frac{|\beta|^2}{2}}e^{\alpha^*\beta-\beta^*\alpha} \tag{3.23}$$

Expressing the complex amplitudes as $\alpha = a_1 + ia_2$ and $\beta = b_1 + ib_2$, this becomes:

$$\mathcal{C}_{|\alpha\rangle}(\beta) = e^{-\frac{|\beta|^2}{2}}\left[\cos(2(a_1b_2 - a_2b_1)) + i\sin(2(a_1b_2 - a_2b_1))\right] \tag{3.24}$$

As we can see, the real component of $\alpha$, $a_1$, determines the oscillation frequency along the imaginary axis $b_2$, while the imaginary component of $\alpha$, $a_2$, determines the oscillation frequency

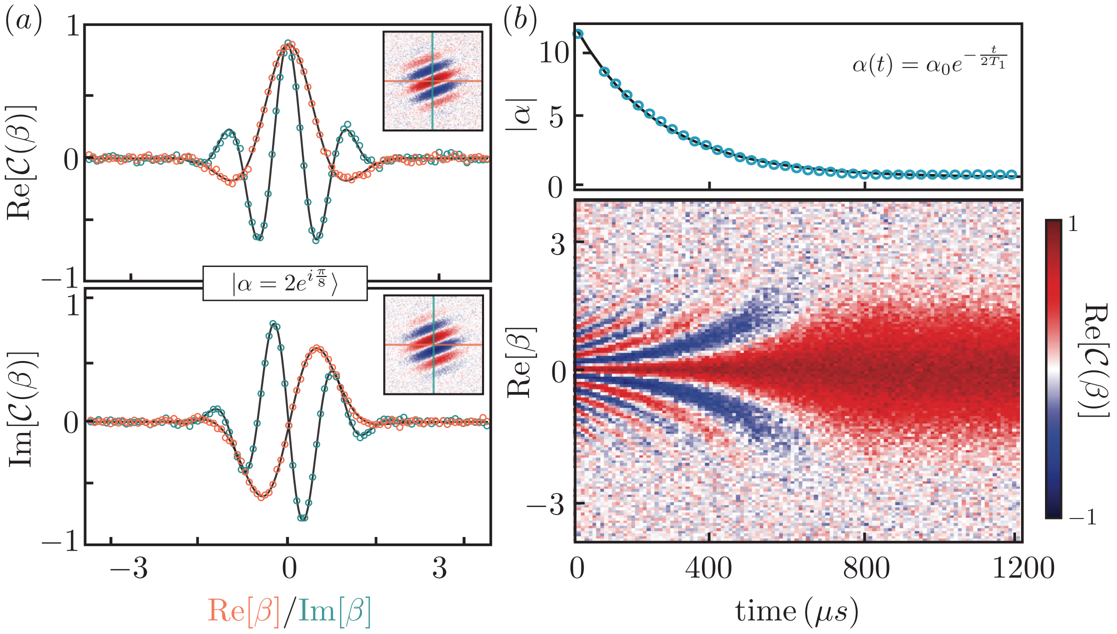

Figure 3.4: **Crosshair and cavity $T_1$ measurements.** (a) Crosshair measurement of the $\mathrm{Re}[\mathcal{C}(\beta)]$ and $\mathrm{Im}[\mathcal{C}(\beta)]$. By measuring and fitting the slices of the characteristic function along $\mathrm{Re}[\beta]$ and $\mathrm{Im}[\beta]$, we can extract $\mathrm{Im}[\alpha]$ and $\mathrm{Re}[\alpha]$. (b) We find the cavity $T_1$ by measuring characteristic function slices that cut through the oscillations, giving access to the $|\alpha|$. We repeat this measurement against time and fit the amplitude decay to extract $T_1$.

along the real axis $b_1$. Thus, we find $a_1$ and $a_2$ by taking two cuts, one along $b_2$ with $b_1 = 0$ and the other along $b_1$ with $b_2 = 0$. We fit them against Equation 3.24 to find $\alpha$. Note that we have to fit the imaginary part of the characteristic function that goes with a sinus to obtain the full phase information of $|\alpha\rangle$. The real part, which goes with a cosine, cannot distinguish between $\pm\alpha$.

Figure 3.4(a) shows a crosshair measurement for the state $|\alpha = 2e^{i\frac{\pi}{8}}\rangle$. The orthogonal cuts through the characteristic function, one along the real axis (orange) and one along the imaginary axis (green), provide complete information about the state's location in phase space. The black lines indicate the fits. The corresponding characteristic function is shown in the insets.

Beyond state characterization, the crosshair measurement serves as an effective tool for determining cavity lifetime ($T_1$). The protocol begins by creating a large coherent state. After characterizing this state via crosshair measurement, we adjust the measurement frame to null any phase drift, ensuring the interference fringes align vertically with one quadrature. The $T_1$

measurement then consists of: (1) preparing the coherent state, (2) introducing a variable wait time, and (3) measuring the characteristic function along the predetermined cut. Note that we measure the characteristic function at frequency $\omega_c$ to avoid relative phase pickup between the cavity and the tomography frame during the wait time.

Figure 3.4(c) presents the results of such a measurement. Prior precise calibration of $\omega_c$ is essential, as the fitting cannot distinguish between decay and rotation of the state. To extract $T_1$, we fit each cut to determine the coherent state amplitude as a function of time and fit the results against a decaying exponential $e^{-t/(2T_1)}$, where the factor of two accounts for the fact that we are fitting amplitude decay, not energy decay.

# Chapter 4

# Protecting quantum interference through phase-space engineering

The boundary between the classical and quantum world remains one of physics's most profound mysteries. While quantum mechanics governs microscopic systems through superposition and entanglement, our macroscopic reality appears deterministic. Schrödinger's famous thought experiment of a cat simultaneously dead and alive [101] highlights this puzzle, yet the answer lies in decoherence. As systems grow larger and environmental interactions increase, quantum interference collapses and coherence vanishes. Engineering quantum systems thus requires a delicate balance between control and preservation of the quantum features.

Cat states, the superposition of macroscopically distinguishable coherent states $|\alpha\rangle \pm |-\alpha\rangle$, are among our best ways to operate at the quantum-classical boundary. In the lab, cat states comprising more than 1000 photons have been realized [102]. Apart from being a gateway to study the boundary, their sub-Planck phase-space structures [103] and non-Gaussian interference features [104–106] make them excellent candidates for quantum metrology [107–110] and quantum teleportation and cryptography [108–111]. Furthermore, their distinct photon number parity renders them a promising quantum error correction code in a hardware-efficient manner [47, 52, 98, 112–117].

To harvest their rich potential, it is vital to protect their quantum non-Gaussian features. To achieve this, we adopted a unique approach. Through understanding the limitations of the hardware, we propose a strategy to engineer cat states that are intrinsically more robust against photon loss. Our approach rests on two key insights: First, the non-Gaussian interference features of cat states manifest as high-frequency components in the characteristic function. Second, photon loss acts in the characteristic function as a point-wise scaling and multiplication with a Gaussian low-pass filter. We can thus achieve protection of the interference features by deterministically compressing the phase-space distribution, effectively reshaping the cat state in such a way that these non-Gaussian features fit under the Gaussian filter imposed by photon loss.

While compressed cat states have previously been realized in optical devices [118, 119] and in ion traps [120, 121], their time dynamics have only been studied through a parametric process [122]. This limitation arises from the difficulty of implementing fast nonlinear control without introducing excessive nonlinearity into the storage cavity.

We overcome this challenge by demonstrating deterministic protection of cat state interference features through engineered phase-space compression. Using only native conditional displacement gates, accessible in a regime with minimal nonlinearity, we reshape quantum states to achieve five-fold enhanced resilience against photon loss—the dominant error channel in superconducting cavities. Our framework provides a versatile platform for creating robust bosonic quantum states with direct applications to fault-tolerant quantum computing [123–126] and quantum metrology.

Experimentally, we directly measure the characteristic function at the centers of the Gaussian interference blobs, which we use as our primary metric for quantum coherence. However, as compression increases, these Gaussian features become highly squeezed. Thus, while their centers remain well-preserved, the surrounding structure may decay. To capture a more holistic picture of the quantum state's robustness, we also post-process our data to infer the Wigner negativity and the sub-Planck structures of the marginal distributions [127].

This chapter is structured as follows: We begin by establishing the theoretical framework connecting phase-space compression to enhanced decoherence protection in Section 4.1. Section 4.2 describes our experimental apparatus and control electronics. We then present our deterministic methods for generating compressed vacuum states in Section 4.3 and subsequently compressed cat states in Section 4.4. Our experimental results, which demonstrate the protection of quantum interference features through multiple metrics, are presented in Section 4.5. Section 4.6 provides an error analysis to contextualize our state creation fidelities.

## 4.1 Cats and photon loss in the characteristic function

Our primary concern in this section is to establish the theoretical foundation for protecting cat states against decoherence through phase-space engineering. While I introduced the characteristic function qualitatively in Fig. 2.3, here we develop a quantitative framework that demonstrates why certain features are vulnerable and how compression can protect them.

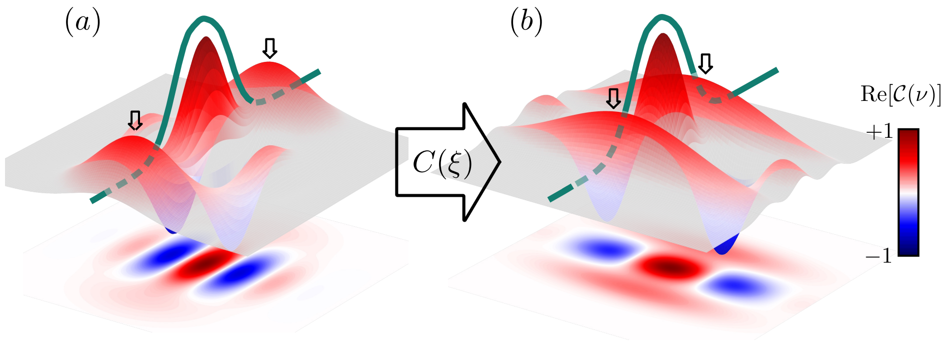

Figure 4.1: **Protection of interference features against photon loss.** (a) Photon loss manifests as a Gaussian low-pass filter (green curve) with variance $1/\kappa t$ in characteristic function. A cat's interference features, the blobs indicated by the arrows, vanish rapidly under the filter as they correspond to high-frequency components. (b) The protection of these features can be achieved through phase-space compression, as symbolized by the white arrow with the compression coefficient $\xi$. The blobs are pushed closer to the origin, making them less susceptible to the Gaussian filter.

The key insight emerges from examining cat states in reciprocal phase space, where the interference features are high-frequency components and how they are affected by photon loss, acting as a Gaussian low-pass filter. We start by deriving the functional form of a cat in that phase space. We then analyze how photon loss acts in reciprocal phase space and then demonstrate quantitatively of compression can protect the interference features.

## Interference features in reciprocal phase space

We begin by deriving the characteristic function of a general cat state with relative phase $\phi$, using the coherent state and displacement operator identities shown in Section 2.1.2:

$$\begin{aligned}\mathcal{C}_{cat}(\nu) &= \frac{1}{2}\Big(\langle\alpha| + e^{-i\phi}\langle-\alpha|\Big)\,\boldsymbol{D}(\nu)\,\Big(|\alpha\rangle + e^{i\phi}|-\alpha\rangle\Big)\\ &= \frac{1}{2}(\langle\alpha|\boldsymbol{D}(\nu)|\alpha\rangle + \langle-\alpha|\boldsymbol{D}(\nu)|-\alpha\rangle\\ &\quad + e^{i\phi}\langle\alpha|\boldsymbol{D}(\nu)|-\alpha\rangle + e^{-i\phi}\langle-\alpha|\boldsymbol{D}(\nu)|\alpha\rangle)\\ &= \underbrace{e^{-\frac{|\nu|^2}{2}}\cos(2\mathrm{Im}[\alpha^*\nu])}_{\text{coherent state fringes}} + \underbrace{e^{-\frac{|\nu|^2}{2}-2|\alpha|^2}\left(e^{i\phi}e^{2\mathrm{Re}[\alpha^*\nu]} + e^{-i\phi}e^{-2\mathrm{Re}[\alpha^*\nu]}\right)}_{\text{interference blobs}}\end{aligned} \tag{4.1}$$

The first term corresponds to the components $\langle\alpha|\alpha\rangle$, $\langle-\alpha|-\alpha\rangle$ and is equivalent to Re[$\mathcal{C}(\nu)$] of a coherent state. The second term arises from the interference terms $\langle\alpha|-\alpha\rangle$, $\langle-\alpha|\alpha\rangle$

and produces two Gaussian blobs located at $\pm 2|\alpha|$ in reciprocal phase space. These Gaussian blobs are the features we seek to protect. The phase of the cat states determines if these non-Gaussian interference blobs appear in the real or imaginary part of $\mathcal{C}(\nu)$. We refer to them as high-frequency components due to their position far out in reciprocal phase space. Having identified the interference features, we now examine how decoherence affects them.

## Photon loss as a Gaussian filter

Photon loss is the dominant loss mechanism in our cavities. In the characteristic function representation, photon loss manifests as a rescaling of the axis and a point-wise multiplication with a Gaussian [128]. We can write the transformation of the characteristic function of a general state as follows:

$$\mathcal{C}(\nu, t) = \mathcal{C}(\nu e^{-\kappa t/2}) e^{(e^{-\kappa t}-1)\frac{|\nu|^2}{2}} \overset{\kappa t \ll 1}{\approx} \mathcal{C}(\nu(1-\kappa t/2)) e^{-\kappa t \frac{|\nu|^2}{2}}. \tag{4.2}$$

where $\kappa$ is the photon decay rate of the cavity and $t$ the passed time. For short times $\kappa t \ll 1$, we can consider the action of photon loss in the characteristic function as a point-wise multiplication with a Gaussian low-pass filter with variance $1/\kappa t$. Concretely, the blobs of our cat states with amplitude $|\alpha_0|$ are located at $\nu = \pm 2|\alpha_0|$ and are thus suppressed by a factor $\mathrm{S} = e^{-\kappa t 2|\alpha|^2}$.

This reveals the crucial problem, the interference features of cat states decay exponentially faster with their size $|\alpha|$. However, it also shows a strategy; if we can move the interference blobs closer to the origin, we can protect them. We can achieve this through phase space compression [122, 129–134].

## Compression protection mechanism

Through phase space compression, we can move the center of the interference blobs from $\nu = 2|\alpha| \rightarrow s2|\alpha|$ with a compression factor $s < 1$. The new suppression factor thus becomes:

$$S_{\text{compressed}} = e^{-\kappa t 2 s^2 |\alpha|^2} \tag{4.3}$$

This formulation allows for a straightforward interpretation: the center of the coherence blobs decays with a reduced decay constant $\kappa_{eff} = 1/T_{1,eff} = \kappa s^2$.

Figure 4.1 visualizes this protection mechanism. The green curve depicts the Gaussian filter with variance $1/\kappa t$. The interference features of the uncompressed cat state in panel (a) are outside of the envelope and are thus strongly affected by the filter. However, applying a compression operation moves these features under the envelope, protecting them as visualized in panel (b).

However, the blob center alone does not capture the full story. As compression increases, the blobs elongate in the anti-squeezed (position) quadrature and eventually extend beyond the protected envelope. This effect is particularly important for observables like photon number parity, which require integration over the full characteristic function. With the choice $s = |\alpha|^{-1}$, we can symmetrize the contours of the Wigner and characteristic functions, ensuring equal spatial extension in both quadratures. For this particular choice, the suppression factor becomes independent of $\alpha$ and $s$.

## 4.2 Experimental setup

Our experimental setup is a standard bosonic cQED architecture, consisting of a coaxial stubline-cavity, an ancilla transmon, and a readout resonator. The device, with a coin for scale, along with a device schematic, is shown in Figure 4.2. The device is designed using a 3D CAD software and then machined in-house.

Our device employs a coaxial stubline resonator machined from a single piece of high-purity aluminum (4N) as the storage mode. The aluminum transmon and readout patterns are deposited on a sapphire chip using double-angle evaporation, with the chip secured by an aluminum clamp and positioned. Hence, the transmon protrudes into the coaxial cavity to establish capacitive coupling between modes. Critical to our compression protocol is a weak dispersive coupling $\chi \approx 40\,\text{kHz}$, enabling ECD control and minimizing the inherited storage non-linearity. We accomplish this through careful optimization of both spatial separation and frequency detuning between the transmon and cavity. All device dimensions and frequencies are designed using Ansys High Frequency Simulation Software (HFSS) to meet the target frequencies and couplings while maintaining high individual mode quality factors for the transmon and storage.

Table 4.1 shows the Hamiltonian parameters of our experimental device. We extract $\chi$ by creating a coherent state in a cavity and then preparing the qubit in $|e\rangle$. We measure $\text{Re}[\mathcal{C}(\nu)]$ for different wait times and extract the induced rotation angle $\phi = \chi t$ by fitting the characteristic function.

The coherence times of our system are shown in Table 4.2. The storage cavity has the longest

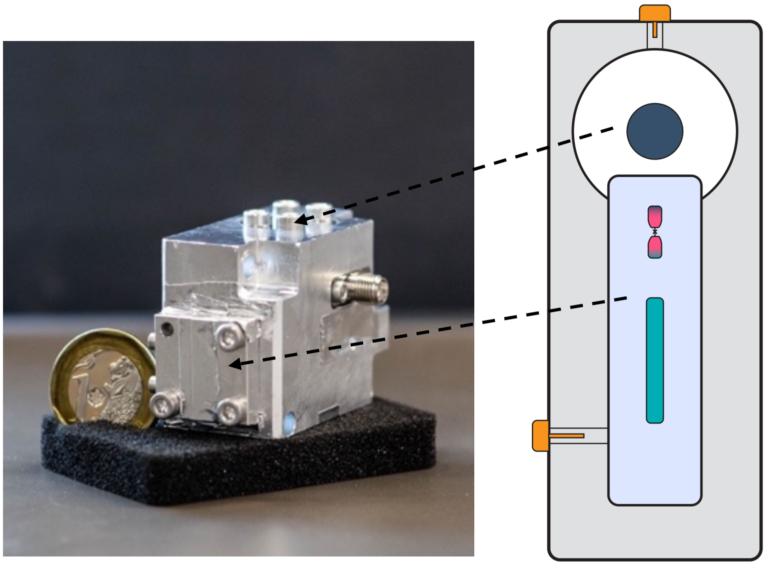

Figure 4.2: **Compressed cat hardware.** Photograph of the used device machined out of high-purity (4N) aluminum with a 1 SGD coin for scale. The device consists of a storage cavity (blue), an ancilla transmon (pink), and a readout resonator (turquoise).

| | Frequency (GHz) | $\chi$ to Transmon | $\chi$ to Cav | $\chi$ to RO |
|---|---|---|---|---|
| Transmon | 5.1461 | 205.4 MHz | 40 kHz | 1 MHz |
| Cav | 6.5428 | 40 kHz | $\sim$10 Hz | $\cdots$ |
| RO | 7.4418 | 1 MHz | $\cdots$ | $\cdots$ |

Table 4.1: **Hamiltonian parameters.** Frequencies and couplings of our experimental setup. All frequencies and coupling are in good accordance with our simulations. The cavity self-kerr is below our measurement precision and is taken from HFSS simulations, indicated by $\sim$.

lifetime with $T_1^c \approx 260\,\mu\mathrm{s}$. This value is artificially limited through the coupling pin, as we are interested in studying the decay dynamics due to the $T_1^c$ mechanism, photon loss. The dephasing rate of the cavity is, as expected, very large with $\geq 5000\,\mu\mathrm{s}$. We are limited by the transmon coherences with $T_1^q = 20\,\mu\mathrm{s}$ and $T_2^q = 18\,\mu\mathrm{s}$.

We measure the cavity $T_1^c$ using a selective $\pi$-pulse ($\sigma > 750\,\mathrm{ns}$) that probes the vacuum population of the cavity as a coherent state decays. Ideally, we would use a much longer pulse; however, our transmon limits the selectivity we can achieve. We use simulation to verify that

| | $T_1$ ($\mu$s) | $T_\phi$ ($\mu$s) | $T_2$ ($\mu$s) | $T_{2e}$ ($\mu$s) |
|---|---|---|---|---|
| Transmon | 20 | $\cdots$ | 18 | 20 |
| Cavity | 260 | $\geq$5000 | $\cdots$ | $\cdots$ |

Table 4.2: **Coherence parameters.** Summary of the coherence parameters of our system. Our system performance is limited by the transmon $T_2$.

our method still gives a good lower bound. To obtain $T^c_\phi$, we measure the real part of the 2D characteristic function for different decay times and compare to simulations with different $T^c\phi$ values. We obtain a value of $T^c_\phi \geq 5$ ms, limited by the residual thermal photon population of the transmon at $\sim 1.5\%$. The transmon coherence are extracted by standard measurements.

To operate a bosonic cQED system in a coherent and stable manner, we must carefully engineer the environment and carefully attenuate and filter the control electronic lines. A schematic of our wiring setup is shown in Fig. 4.3. The device is mounted at the bottom of a copper bracket and placed inside of a cryoperm-shield to filter stray magnetic fields. The top of the copper bracket is then mounted onto the base plate of a Bluefors dilution refrigerator.

We use a field-programmable gate array from Quantum Machines to control the cavity, qubit, and readout. The digital-to-analog (DAC) ports provide signals with a bandwidth of 250 MHz. These signals are fed into an IQ mixer and upconverted through a local oscillator (LO) to the GHz range. Before reaching the device, the signals are attenuated and filtered at the different stages of the cryogenic environment.

The reflected readout signal is amplified at the base stage via a dimer Josephson-junction-array amplifier (DJJAA) [135], followed by a high-electron-mobility-transistor (HEMT) at the 4 K stage. After another amplification and downconversion at 300 K, the signal is fed back into the FPGA and digitized through an analog-to-digital converter (ADC). The digitized signal is then demodulated and integrated using optimized integration weights [136] to condense the information of one readout pulse into a single point in the IQ plane. For each measurement, the value is compared against a threshold value and assigned a value of either 0 or 1.

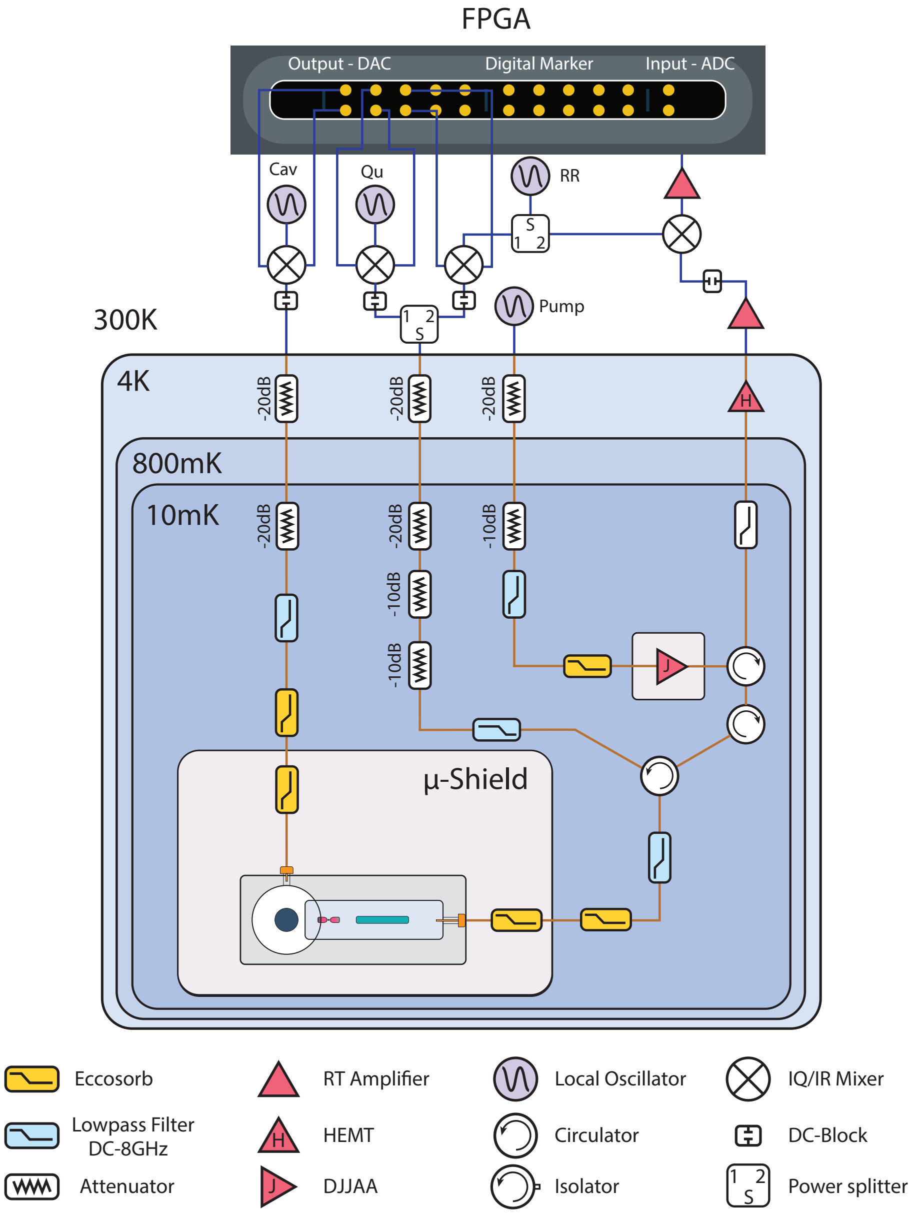

Figure 4.3: **Wiring diagram.** Our FPGA is a Quantum Machines OPX, which we use in conjunction with local oscillators to generate arbitrary pulses in the 4-8 GHz range. Our wiring includes a standard set of attenuators and filters, including low-pass filters and Eccosorb. The readout signal is amplified in four stages: a DJJAA quantum-limited amplifier at base temperature, HEMT amplifiers at 4 K, and two sets of RT amplifiers.

## 4.3 Creating a compressed vacuum state

To achieve deterministic compression, we follow the proposal outlined in [137]. This scheme relies on the repeated action of the two unitaries:

$$\boldsymbol{U}_k = e^{iu_k \boldsymbol{P}\boldsymbol{\sigma}_x}, \boldsymbol{V}_k = e^{iv_k \boldsymbol{X}\boldsymbol{\sigma}_y} \tag{4.4}$$

$\boldsymbol{U}_k$ $(\boldsymbol{V}_k)$ creates a conditional displacement along the position (momentum) quadrature dependent on the qubit state decomposed into eigenstates of $\boldsymbol{\sigma}_x$ $(\boldsymbol{\sigma}_y)$.

When we applied $\boldsymbol{U}_k\boldsymbol{V}_k$ subsequently on the joint qubit cavity state $|g\rangle\,|0\rangle$, with carefully chosen parameters $u_k, v_k$, their action can effectively be summarized as follows. $\boldsymbol{U}_k$ creates a superposition of coherent state with opposite phases with the qubit, while $\boldsymbol{V}_k$ effectively disentangles qubit and cavity. Applying these two unitaries $n$ times is therefore able to create a superposition of $2^n$ coherent states, leaving the qubit in its ground state.

To understand how we can exploit this to make a compressed state, a good approximation of a squeezed state, we decompose the squeezed state in the coherent state eigenbasis. We can write the discretized form as [137]:

$$|\text{sqvac}\rangle_\Delta \propto \sum_{\alpha_s \in L} \exp\left(-\frac{\alpha_s^2}{\Delta^{-2} - 1}\right) |\alpha_s\rangle \tag{4.5}$$

where $L$ is a lattice on the real line and $\Delta$ quantifies the degree of squeezing. This form reveals that a squeezed state can be thought of as the superposition of coherent states with Gaussian envelope. Thus, by fixing the number of repetitions and choosing appropriate parameters for $u_k, v_k$, we can create a compressed vacuum state.

To implement these unitaries in our architecture, we decompose them into single-qubit rotations and ECD gates:

$$\boldsymbol{U}_k = \boldsymbol{R}_y\left(-\frac{\pi}{2}\right)\boldsymbol{ECD}_-(u_k)\boldsymbol{R}_y\left(-\frac{\pi}{2}\right), \tag{4.6}$$

$$\boldsymbol{V}_k = \boldsymbol{R}_x\left(\frac{\pi}{2}\right)\boldsymbol{ECD}_+(iv_k)\boldsymbol{R}_x\left(\frac{\pi}{2}\right). \tag{4.7}$$

Generating compressed vacuum states requires a delicate balance between the number of $\boldsymbol{UV}$ repetitions with optimized parameters $u_k, v_k$ and the dominant decoherence time in the system. While more repetitions lead to increased compression, about 3-4 dB, per additional repetition, eventually the decoherence mechanisms will take over and negate any possible gain. In our system, we are limited by the transmon decoherence of $T_{2e} \approx 20$ µs. With this in mind, we chose three iterations, which each iteration taking about $\sim 1.37$ μs. This is limited by the time it takes to implement one ECD gate, which is approximately 600 ns.

To find the parameters $u_k, v_k$, we use a gradient-based optimization method to maximize the overlap with the target squeezed state. During the optimization, we bound the parameters to the range $(-2, 2)$. This keeps the unconditional displacements in the ECD gates moderate. In simulation, we find an overlap fidelity of $\mathcal{F} > 0.99$ with the target states. Table 4.3 shows optimized coefficients for $-3$ dB, $-5$ dB, $-6$ dB and $-7$ dB.

| | $u_1$ | $v_1$ | $u_2$ | $v_2$ | $u_3$ | $v_3$ |
|---|---|---|---|---|---|---|
| $-3$ dB | 1.39 | $-0.51$ | $-0.2$ | 0.46 | $-0.32$ | 0.65 |
| $-5$ dB | $-0.48$ | $-0.51$ | $-1.85$ | 0.31 | 0.56 | $-0.91$ |
| $-6$ dB | 1.6 | $-0.39$ | $-0.48$ | 1.04 | $-1.11$ | $-0.32$ |
| $-7$ dB | $-0.83$ | $-0.56$ | 1.3 | 0.56 | $-1.26$ | $-0.39$ |

Table 4.3: **Optimized compression coefficients.** Optimize $u, v$ parameters for three $\boldsymbol{UV}$ steps to create vacuum with $-3$ dB,$-5$ dB, $-6$ dB and $-7$ dB compression.

Using this decomposition, we create three compressed vacuum states with $-3$ dB, $-6.7$ dB and $-7.6$ dB through three $\boldsymbol{UV}$ iterations. To characterize the compressed states, we measure $\mathrm{Re}[C(\nu)]$ of the generated states, using the protocol introduced in Chapter 3. The measurement results are shown in Fig.4.4.

We measure the compression values by fitting 1D Gaussian cuts along each quadrature and calculate the compression in dB as $20\log_{10}(\sigma/\sigma_{\mathrm{vac}})$. The corresponding values for simulation and experimental data are shown in Table. 4.4.

| | Theory | | Experiment | |
|---|---|---|---|---|
| | $\langle \boldsymbol{P}^2 \rangle$ | $\langle \boldsymbol{X}^2 \rangle$ | Compression in $\boldsymbol{P}$ | Compression in $\boldsymbol{X}$ |
| $-3$ dB | 2.96 | $-2.98$ | 2.6 | $-3$ |
| $-6$ dB | 5.71 | $-5.93$ | 5.4 | $-6.7$ |
| $-7$ dB | 5.9 | $-7.24$ | 6.4 | $-7.6$ |

Table 4.4: **Achieved compression comparison simulation and experiment.** The achieved compression closely matches the target for smaller values. It starts to deviate for larger values as we approach saturation of the achievable squeezing in three steps.

In simulation, the protocol generates genuine squeezing, as quantified by the variance of the quadrature operators. The achieved squeezing also closely matches the target. For larger squeezing values, we start to saturate the achievable squeezing using three repetitions, leading to

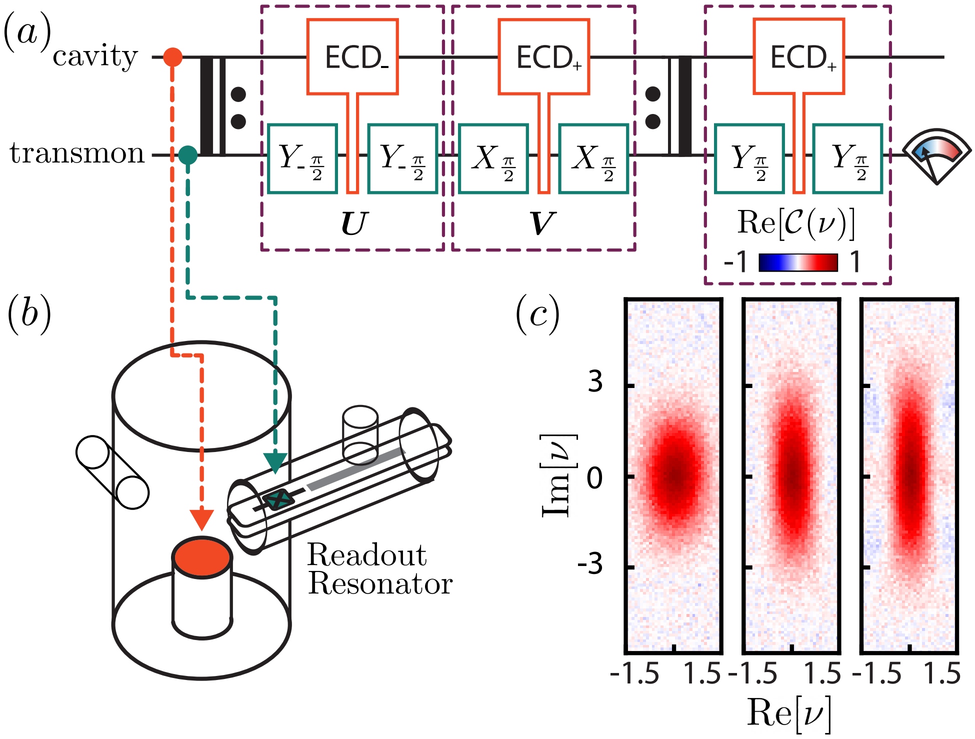

Figure 4.4: **Deterministic phase space compression.** (a) Protocol that deterministically creates a compressed vacuum state from vacuum through the repeated application of $\boldsymbol{U}_k \boldsymbol{V}_k$. The operations are each deconstructed into qubit rotations and ECD gates. Finally, we measure the real part of the characteristic function. (b) Device schematic that is used to generate the states, consisting of a storage cavity, a transmon and a readout resonator. (c) Measured data of the real part of the characteristic function of compressed vacuum state. Each state is implemented by applying three $\boldsymbol{U}\boldsymbol{V}$ repetitions with optimized parameters. We achieve a phase-space compression of $-3$ dB, $-6.7$ dB and $-7.6$ dB along $[Re][\nu]$, respectively.

larger deviations from the target. In the experiment, the resulting states are only approximately squeezed, with some smaller outlying features in phase space. Hence, we distinguish our states from genuinely squeezed states by calling them compressed states. We quantify the compression in terms of the Gaussian's standard deviation.

Furthermore, the optimization protocol does not account for the hardware's noise model. The noise of the system, dominated by transmon decoherence $T_{2e}$, leads to deviations from the ideal target states, introducing side features that reduce the amount of real squeezing along one cut, as shown in Fig. 4.5. Nevertheless, the resulting states are effectively compressed along one quadrature. The undesired features are no hindrance, as the protection arises through the compression, not genuine squeezing.

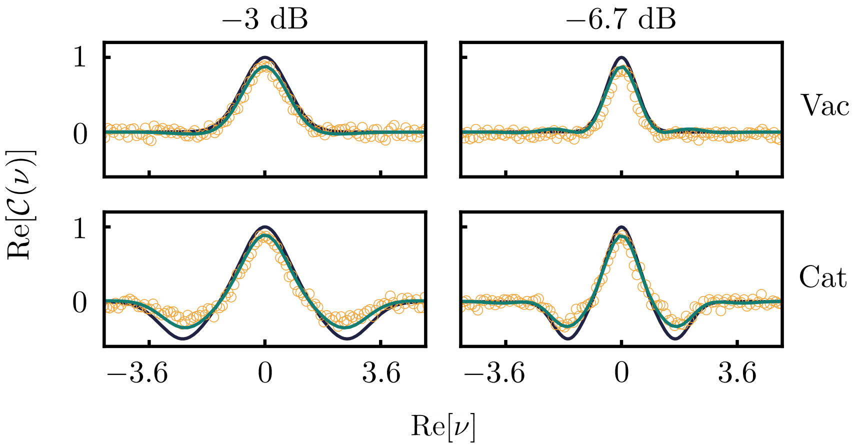

Figure 4.5: **Simulation of compressed vacuum under qubit decoherence.** Comparison of characteristic function cuts without loss (black), with qubit decoherence $T_{2e}$, and experimental data (golden circles). The simulated data with loss is scaled with the contrast of the origin. Decoherence leads to the appearance of sideloops that are apparent in the $-6.7$ dB compression simulation and data.

In this section, we successfully demonstrate our capability to deterministically create compressed vacuum states with compression levels up to $-7.6$ dB using a protocol based on ECD gates and qubit rotations, without the need for parametric control. We showed good agreement between theory and experiment, with simulation closely matching experimental values across multiple compression levels. By balancing repetitions with optimized parameters against decoherence, we established a robust and scalable framework to reshape phase-space distributions on demand. This represents a significant advancement for quantum information tasks that require bosonic mode control.

In the next section, we will explore how to use compressed vacuum states as input to create compressed cat states. We will measure the decay of the non-Gaussian features of default and compressed cat states to demonstrate that compression protects these features against photon loss.

## 4.4 Creating a compressed cat state

Having demonstrated deterministic compression, we now turn our attention to creating compressed cat states, the main ingredient of our experiment.

We start with cat state creation. Our protocol is shown in Fig. 4.6. Starting from the joint ground state $|g\rangle\,|0\rangle$, we apply a single $\boldsymbol{V}$ operation. The action of $\boldsymbol{V}$ leaves the qubit and cavity in an entangled state. $|g\rangle$ is entangled to an even cat state while $|e\rangle$ is entangled to an odd cat state. A post-selection measurement then collapses the qubit and the corresponding cavity state, leaving us with an even or odd cat state in the cavity. We can easily extend this protocol to create a compressed cat state by first initializing the cavity in a compressed vacuum state.

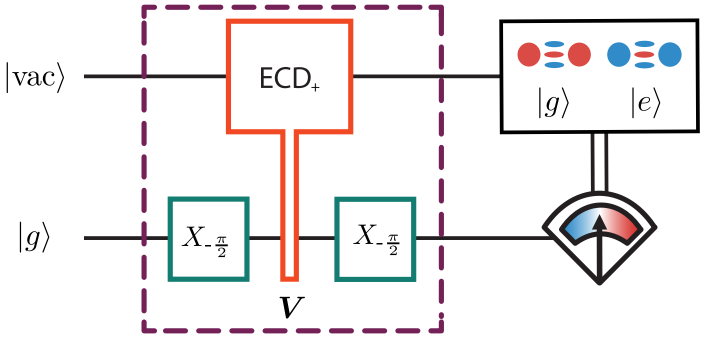

Figure 4.6: **Protocol to create a cat state.** Acting with $\boldsymbol{V}$ on $|g\rangle\,|0\rangle$, leaves us in an entangled state with $|g\rangle$ entangled to an even cat state and $|e\rangle$ entangled with an odd cat state. Following up with a post-selection measurement collapses the cavity into a cat state. We can create a compressed cat by first initializing the cavity in a compressed vacuum state.

Our technique is flexible and also allows for the reverse approach, where we first create a cat state and then compress it. We verified this in simulation for three $\boldsymbol{UV}$ repetitions for $-3$ dB, $-5$ dB, $-6$ dB and $-7$ dB. We find fidelities of $\mathcal{F} > 0.99$ for each. However, creating the compressed cat from a compressed vacuum is advantageous when considering the system's coherence parameters. The time it takes to compress is the majority of our state creation protocol. If we start with a cat state, this time will be spent further out in phase space, rendering it more susceptible to decoherence. Furthermore, the required conditional displacement to create the cat is larger, a fact that becomes apparent when we consider the commutator of the displacement operator $\boldsymbol{D}(\alpha)$ and squeezing operator $\boldsymbol{S}(z)$.

$$\boldsymbol{D}(\alpha)\boldsymbol{S}(z) = \boldsymbol{S}(z)\boldsymbol{S}^{\dagger}(z)\boldsymbol{D}(\alpha)\boldsymbol{S}(z) = \boldsymbol{S}(z)\boldsymbol{D}(\gamma), \tag{4.8}$$

with $\gamma = \alpha\cosh r + \alpha^{*}e^{i\theta}$ where $r$ is the degree of squeezing and $\theta$ the angle. For consistency between the two approaches, we take this into account when creating the compressed cat states.

Fig. 4.7 shows the measured real part of the characteristic function for a default cat state (top) and a compressed cat state (bottom) for $|\alpha| = 1.8$ and compression $\gamma = -6.7\,\mathrm{dB}$. We create an even cat state (red blobs) and an odd cat state (blue blobs). The effect of compression on the interference features is visible, as the interference blobs are elongated and pushed toward the origin.

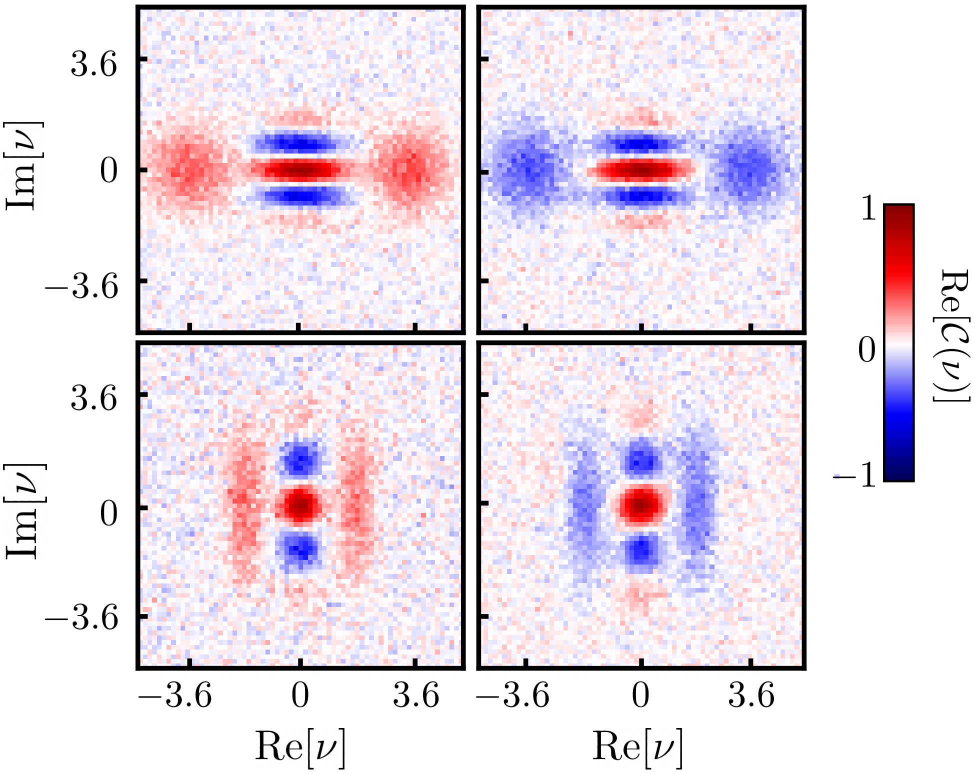

Figure 4.7: **Characteristic function of compressed cat states.** Experimental data show the real part of the characteristic function of an even and odd cat state (top) and an even and odd compressed cat state (bottom) for $|\alpha| = 1.8$ and $\xi = -6.7\,\mathrm{dB}$. For the default cat state, the interference blobs appear at $\pm 2|\alpha|$. The effect of compression on these coherence blobs is that they are elongated and pushed closer to the origin.

## 4.5 Protecting a cat's interference features

To demonstrate the protection of a cat's quantum interference features against photon loss, we must carefully select the measured features that we correlate with quantum interference.

Based on Equation 4.1, we established that the interference blobs of the characteristic function at $\pm 2|\alpha|$ correspond to the quantum interference terms $\langle\alpha| - \alpha\rangle$ , $\langle -\alpha|\alpha\rangle$. They represent high-frequency components in reciprocal phase space and constitute non-Gaussian features that cannot be reproduced through a mixed state. The fact that we can directly measure these features makes them our ideal metric to quantify the protection of quantum coherence.

We quantify the protection of phase-space compression against photon loss by monitoring the decay of the blob amplitude for an odd cat state with different degrees of compression over a time span similar to the cavity's $T_1 = 260$ µs. We extract the amplitude by directly measuring 1D cuts of the real part of the characteristic function along $\mathrm{Re}[\nu]$. The results of these measurements for compression values of $0$ dB $-3$ dB, $-6.7$ dB and $-7.6$ dB are shown in Fig 4.8 (a). The measured amplitudes (open circles) closely match master-equation simulations (solid lines) that include photon loss.

To further quantify the decay of the coherence blobs, we derive a theoretical model that describes the dynamics of the coherence blob maxima (see Appendix C). As we are interested in the decay of the blobs, we consider the ratio of the interference blob amplitude after decay $\tau$ to that of the undamped cat with the same compression factor $s$; we dub this the fidelity $F_{s,\tau}$. For short times, $\tau \ll T_1^c$, takes the form

$$F_{\pm,s,\tau} \approx \exp\left(-\frac{\tau}{2T_{\text{eff}}}|\alpha_0|^2\right) \tag{4.9}$$

where $T_{eff} = T_1^c/s^2$ is the effective decay constant of the compressed cat state. Using this model, we extract the measured effective decay constants. For the uncompressed cat state, we find $(273 \pm 1)$ µs, which is in good accordance with the intrinsic decay constant of the cavity of $\approx 260$ µs. For $-3$ dB, $-6.7$ dB and $-7.6$ dB, we find a significant increase in the effective lifetimes to $(516 \pm 32)$ µs, $(1247 \pm 132)$ µs and $(1439 \pm 172)$ µs, respectively. This is a more than fivefold increase in lifetime for the $-7.6$ dB compression and matches closely with the predicted value of $5.75$ in Section 4.1.

Fig. 4.8 (b) shows snapshots of characteristic functions for a default ($0$ dB) and a compressed cat state ($-6.7$ dB) at $20$ µs, $50$ µs and $100$ µs. While the interference blobs of the uncompressed cat state vanish around $100$ µs, the interference blobs of the compressed cat state are still clearly visible. Furthermore, the cat states retain their shape over a timespan of $100$ µs, showing no signs of distortion. This is crucial for the use of cat states in quantum information processing tasks and highlights the importance of our chosen operating regime, which features small inherited storage anharmonicity.

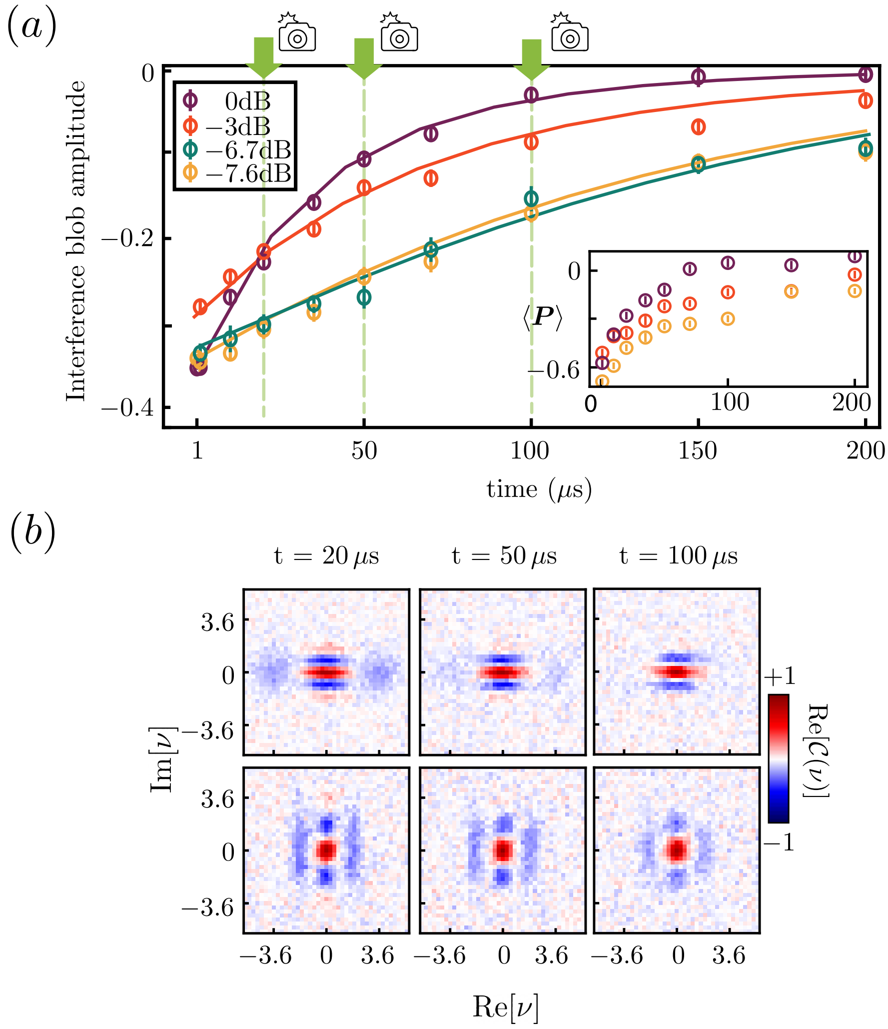

Figure 4.8: **Compression protects interference features against photon loss.** (a) Decay dynamics of the interference blobs in the real part of the characteristic function of cat states with different degrees of compression. Experimental data (open circles) and master equation simulation (solid lines) show good agreement. The error bars are extracted using standard bootstrapping techniques. The blob amplitude follows an exponential, with the corresponding time constant increasing with the degree of compression. The inset shows the parity decay, obtained by integrating the entire characteristic function. The data demonstrates that compressed cat states are more resilient against photon loss. (b) Experimentally measured Characteristic function snapshots at different times, showing the protection of interference features through compression.

Additionally, by integrating over the entire characteristic function, we can determine the origin of the Wigner function $W(0,0)$, see 2.13, which corresponds to the parity of our states.

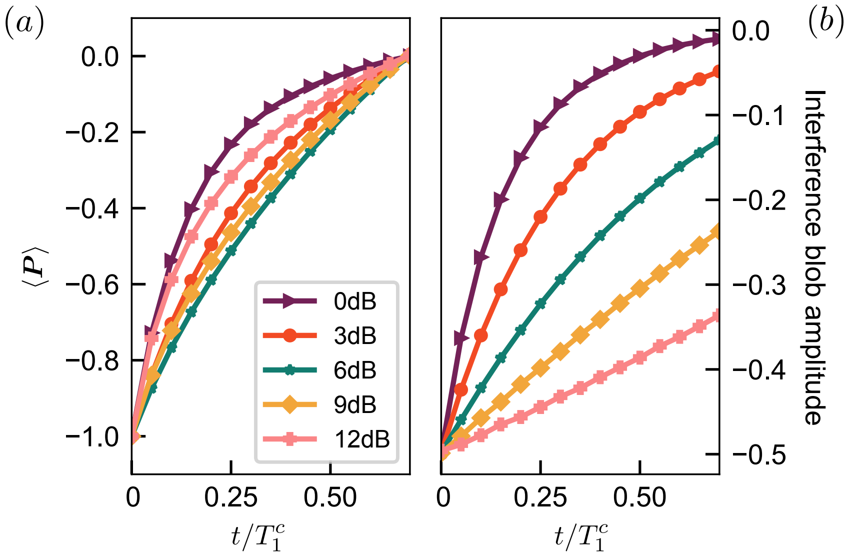

Figure 4.9: **Comparison of parity and interference blob decay.** Simulation of the (a) decay of the photon number parity $\langle \mathcal{P} \rangle$ and the (b) decay of the interference blob amplitude for different levels of compression. While the protection of the interference blobs continuously increases with compression, there is an ideal compression point for photon number parity.

$\langle \mathcal{P} \rangle$. The corresponding data is shown in the inset of Fig. 4.8 (a). Like the interference blobs, the parity shows an exponential decay that is slowed with compression.

However, a quick consideration reveals that we generally do not expect the center of the interference blobs in the characteristic function and photon number parity to exhibit the same behavior under a given compression, see discussion in Appendix C. While stronger compression protects the center of the interference blobs, eventually the anti-squeezed quadrature will elongate beyond the protection envelope. For photon number parity, we must focus on the entire blob as we integrate over the whole characteristic function. If the compression is too large, the elongation in the opposite quadrature will cause the cat state to exceed the range of the Gaussian filter. We investigated this behavior by simulating the decay of the interference blobs and photon number parity under different compression levels, as shown in Fig. 4.9. The simulations demonstrate that while the protection of the interference blobs continuously increases with compression, an optimal compression level exists, dependent on the decay rate of the cavity and the size of the cat state.

Furthermore, we consider the behavior of sub-Planck structures in phase space, another intrinsically non-Gaussian attribute and witness for quantum coherence [103]. We obtain these distributions by calculating the 1D Fourier transform of the characteristic function along $\mathrm{Im}[\nu] = 0$, which yields the marginal distribution of the Wigner function along $\mathrm{Im}(\alpha)$. The decay dynamics of these features for a default cat (0 dB) and a compressed cat state (−7.6 dB) are shown in Fig. 4.10. At 100 µs, the sub-Planck structures are still clearly visible in the compressed cat. However, for the cat state, these features entirely vanished at 100 µs.

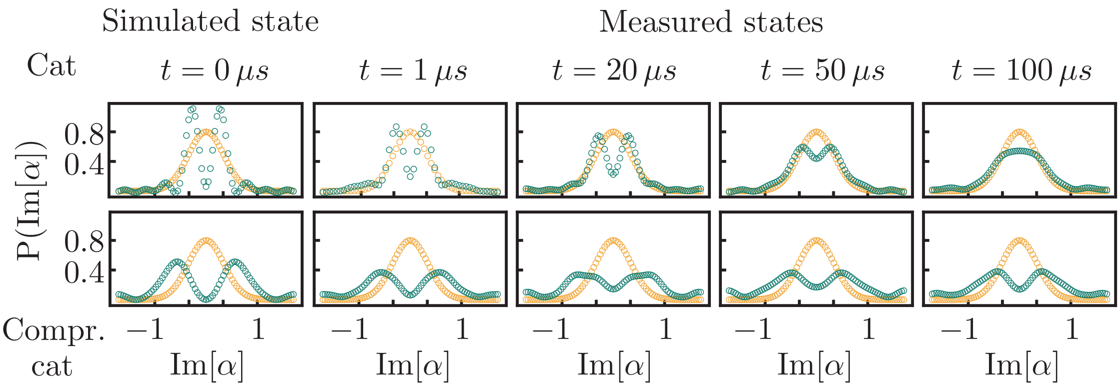

Figure 4.10: **Decay of sub-Planck structures.** Comparison of the decay of the sub-Planck structures in a Cat state (top) and compressed cat state with −7.6 dB (bottom). The marginal distributions along $\mathrm{Im}[\alpha]$ are obtained by calculating the $1 - D$ Fourier transform of the characteristic function along $\mathrm{Im}[\nu] = 0$. In each plot, we compare the cats' features (green) with the width of an ideal vacuum state (golden).

Finally, we use two different methods to calculate the overlap of the ideal uncompressed and compressed cat state −7.6 dB against the corresponding measured states after decay times of 1 µs, 20 µs, 50 µs, and 100 µs. For this, we measure the real part of the characteristic function with 1000 averages and experimentally verify that the imaginary part is negligible. As a first method, we employ convex optimization [138] to reconstruct the density matrices, as we expect a maximum photon number of $\bar{n} \approx 4$ for the compressed cat with $|\alpha| = 1.8$ and $s =$−7.6 dB, we chose a Hilbert space size of 20. This size ensures that we capture more than 99.9% of the photon number distribution.

The corresponding fidelities $\mathcal{F}_{\text{cat, rec}}$ and $\mathcal{F}_{\text{ccat, rec}}$ are shown in the second and third columns of Table 4.5. Once again, we see that the uncompressed cat state decays more rapidly, with a rapid drop of fidelity from 75% to 55% between 1 µs to 20 µs. In contrast, the fidelity of the compressed cat state decreases only from 61% to 56%. As a second method, we calculate the overlap by directly integrating the characteristic function over phase space, using the equation:

$$\mathcal{F}_{\text{int}} = \frac{1}{\pi} \int C_{\text{ideal}}(\nu) C_{\text{exp}}(\nu)^* d^2\nu \tag{4.10}$$

The corresponding fidelities of the cat $\mathcal{F}_{\text{cat,int}}$ and compressed cat $\mathcal{F}_{\text{ccat,int}}$ are shown in the last two columns of Table 4.5. The behavior is consistent with what we observed in the density matrix reconstruction.

| State | $\mathcal{F}_{\text{cat,rec}}$ (%) | $\mathcal{F}_{\text{cat,int}}$ (%) | $\mathcal{F}_{\text{ccat,rec}}$ (%) | $\mathcal{F}_{\text{ccat,int}}$ (%) |
|---|---|---|---|---|
| 1 µs | $75(\pm0.5)$ | $74.8(\pm0.6)$ | $61(\pm0.7)$ | $67.1(\pm0.7)$ |
| 20 µs | $55(\pm0.6)$ | $61.5(\pm0.8)$ | $56(\pm0.5)$ | $60.4(\pm0.7)$ |
| 50 µs | $45(\pm0.7)$ | $47.9(\pm0.7)$ | $50(\pm0.6)$ | $53.9(\pm0.6)$ |
| 100 µs | $40(\pm0.7)$ | $41.2(\pm0.7)$ | $43(\pm0.5)$ | $46.4(\pm0.7)$ |

Table 4.5: **Fidelities against time.** Overlap fidelities found by reconstructing the density matrices $\mathcal{F}_{rec}$ and directly integrating the characteristic function $\mathcal{F}_{int}$.

## 4.6 Error budget

The fidelities of our compressed cat states are generally in the range of $65(\pm5)\%$, limited by the decoherence timescales in our hardware. We analyze the imperfections by considering a single $\boldsymbol{U}$ gate as the elementary operation, since our state creation process consists essentially of $\boldsymbol{U}$ or $\boldsymbol{V}$ operations sandwiched between single transmon rotations. The fidelities are calculated as the overlap between the ideal state and the state subject to a single decoherence mechanism, $F = \langle\psi_{\text{ideal}}|\rho_{\text{loss}}|\psi_{\text{ideal}}\rangle$. Table 4.6 presents the simulated infidelities resulting from various error sources in our device, calculated using master equation simulations that incorporate only the respective decoherence mechanism.

To validate this error budget, we compare it with experimentally observed imperfections in our characteristic function measurements. Our measured vacuum state exhibits a maximum contrast of approximately $88.4\%$. Since this measurement requires a single $\boldsymbol{U}$-type gate and transmon readout, we can sum the individual contributions: the $\boldsymbol{U}$ operation introduces approximately $7\%$ infidelity. In contrast, the readout contributes $(P_{ee}+P_{gg})/2 \approx 3.2\%$ infidelity. This yields an overall measurement fidelity limit of approximately $90\%$, consistent with our observed vacuum state contrast. We use this as a normalization factor for subsequent cat and compressed cat state data to isolate state preparation errors from measurement imperfections.

| Error channel | Estimated infidelity (%) |
|---|---|
| Ancilla dephasing | $4$ |
| Ancilla decay | $2$ |
| Cavity dephasing | $1$ |
| Cavity decay | $0.01$ |
| $\boldsymbol{U}$ | $\approx 7$ |
| Readout $\lvert g\rangle \to \lvert g\rangle$ | $1.4$ |
| Readout $\lvert e\rangle \to \lvert e\rangle$ | $5$ |

Table 4.6: **Error budget.** Estimated errors due to decoherence and SPAM (state preparation and measurement) of the prepared cats and compressed cats. The leading errors are ancilla dephasing and decay, as well as readout.

For the compressed vacuum and cat states presented in the main results, state creation involves three sets of $\boldsymbol{U}\boldsymbol{V}$ operations followed by a measurement to project the transmon state. The post-selection process effectively removes the contribution of transmon $T_1^q$, reducing the infidelity of each $\boldsymbol{U}$ or $\boldsymbol{V}$ gate to approximately $5\%$. Using our simulated error budget, we expect these states to suffer from approximately $33\%$ infidelity, which aligns well with our experimental observations.

While decoherence represents the dominant limitation, other mechanisms such as the Kerr effect, calibration inaccuracies, and residual imaginary components in the characteristic functions could introduce additional imperfections. However, these contributions are small compared to decoherence errors and remain below our current resolution for detailed analysis. As this protocol is applied to systems with improved coherence parameters, investigating and minimizing these secondary error sources will become increasingly crucial for achieving higher-fidelity compressed cat states.

## 4.7 Discussion

In this chapter, we have demonstrated that phase-space compression provides a powerful and versatile framework for protecting the quantum non-Gaussian interference features of cat states against photon loss, the dominant decoherence mechanism in superconducting cavities. Through our deterministic compression protocol, based on ECD gates, we achieved a five-fold enhancement in the effective lifetimes of interference features for a compression level of $-7.6$ dB. These results provide direct experimental validation of this protection mechanism across multiple quantum coherence metrics.

Our approach exemplifies a broader paradigm of hardware-aware quantum state engineering, where theoretical ideas and experimental hardware are co-developed to optimize performance against the dominant error channels. Rather than simply implementing an ideal theoretical codeword in our hardware, we have tailored our state to the hardware by utilizing our compression techniques to give the state better intrinsic resilience. Specifically, our compressed cat states have well-defined and better-protected parity, making them natural candidates for efficient quantum error correction in bosonic modes where parity is often used as an error syndrome. This is underlined by recent proposals [139, 140] and validated by an impressive experimental demonstration of a squeezed cat code with a bit flip rate 160 times larger compared to previous cat qubit implementations. [126]. This co-design philosophy will be crucial to reduce the overhead required for quantum error correction.

Beyond error correction, the ability to deterministically reshape phase-space distributions opens new avenues for tailoring quantum resources for specific applications. In continuous-variable quantum metrology [108–110, 141], where sub-Planck structures play a crucial role, our enhanced protection directly enables more robust sensing protocols, thereby increasing precision. Our technique utilizes only native gates and is therefore readily integrable into current hardware. Moreover, our framework extends beyond cat states. It provides a systematic approach to engineer other non-Gaussian states to improve their resilience against limiting decoherence mechanisms, potentially opening the door to the creation of novel bosonic error correction codes.

# Chapter 5

# Creating tripartite entangled states in bosonic cQED

The extension from bipartite to multipartite entangled quantum systems reveals fundamentally new phenomena that cannot be understood through generalizing bipartite correlations. While previous demonstrations of two-mode cat states established the feasibility of distributing macroscopic quantum coherence across multiple harmonic oscillators [97], the transition to three or more modes introduces entirely new classes of entanglement. In particular, Dür, Vidal, and Cirac showed that there exist two classes of genuine tripartite entanglement that are inequivalent, the Greenberger-Horne-Zeilinger (GHZ) states and W-states [142]. These states have strikingly different properties. GHZ states display maximal tripartite entanglement without any bipartite correlations, while W-states maintain maximal bipartite entanglement between any two pairs, even if the third party is lost. These properties make W-states attractive for various quantum information processing tasks [143–145].

Experimental demonstrations of multipartite entangled states have progressed steadily across platforms, including ion traps [146], superconducting systems [147, 148], and optical systems [149], yet remain confined to discrete variable systems. In continuous variable systems, there has been much progress in the implementation of highly entangled cluster states [150–152]. However, the combination of multipartite entanglement and coherent state superpositions has remained unexplored due to its challenging implementation. Such states offer insights into many-body quantum correlations and offer practical advantages for distributed quantum sensing and error-corrected quantum computation [44, 153].

In this chapter, I will present preliminary data demonstrating the generation of a GHZ-cat state and a W-cat state. These experiments represent the first realization of multipartite entangled cat states beyond two modes and establish a versatile testbed to explore the rich physics of multipartite macroscopic entanglement. We implement our states by utilizing the excellent multimode capabilities of the ECD gate and do full tomography over the entangled states by measuring specific points in the high-dimensional joint characteristic function.

This chapter is structured as follows: I begin in Section 5.1 by discussing our choice of coupling architecture and demonstrating how this enables efficient multimode control through ECD gates. Section 5.2 introduces the protocols for creating bosonic GHZ-cat and W-cat states, while Section 5.3 develops an efficient characterization method that maps characteristic function points to Pauli operator expectation values. I then present our experimental implementation in Section 5.4, including the preliminary setup, followed by our first results on the creation of the GHZ-cat and W-cat state in Section 5.5. Section 5.6 identifies the limitations of our current hardware through simulations, and I conclude in Section 5.7 with a summary of results and a roadmap of the next steps.

## 5.1 One-to-all coupling architecture

The creation of multimode entangled states in bosonic cQED requires careful selection of the underlying coupling architecture. Two primary approaches present distinct trade-offs: linear coupling, where bosonic modes are arranged in a chain with non-linear elements coupling adjacent modes, and one-to-all coupling, where a single non-linear element mediates the interaction between all bosonic modes simultaneously. While linear coupling offers a modular and simpler design, it imposes significant hardware overhead, longer protocols, as entanglement must be spread, and correlation of single-mode measurements for joint state characterization. Conversely, one-to-all coupling, despite increased constraints in physical and frequency space, enables parallelized state preparation across multiple modes and direct in situ joint measurements by mapping multimode information onto a transmon.

Fig. 5.1 (a) depicts our target architecture: three quantum harmonic oscillators (Alice, Bob, Charlie), each weakly dispersively coupled to a shared transmon. In the rotation frame of the cavities at frequencies $\omega_i - \chi_{qi}/2$ for $i \in \{a, b, c\}$, the effective coupling Hamiltonian with the transmon truncated to its first two levels becomes:

$$\frac{\boldsymbol{H}}{\hbar} = -\frac{\chi_{qa}}{2}\boldsymbol{a}^\dagger\boldsymbol{a}\boldsymbol{\sigma}_z - \frac{\chi_{qb}}{2}\boldsymbol{b}^\dagger\boldsymbol{b}\boldsymbol{\sigma}_z - \frac{\chi_{qc}}{2}\boldsymbol{c}^\dagger\boldsymbol{c}\boldsymbol{\sigma}_z \tag{5.1}$$

where $\boldsymbol{a}$, $\boldsymbol{b}$, and $\boldsymbol{c}$ are the ladder operators of Alice, Bob, and Charlie, respectively.

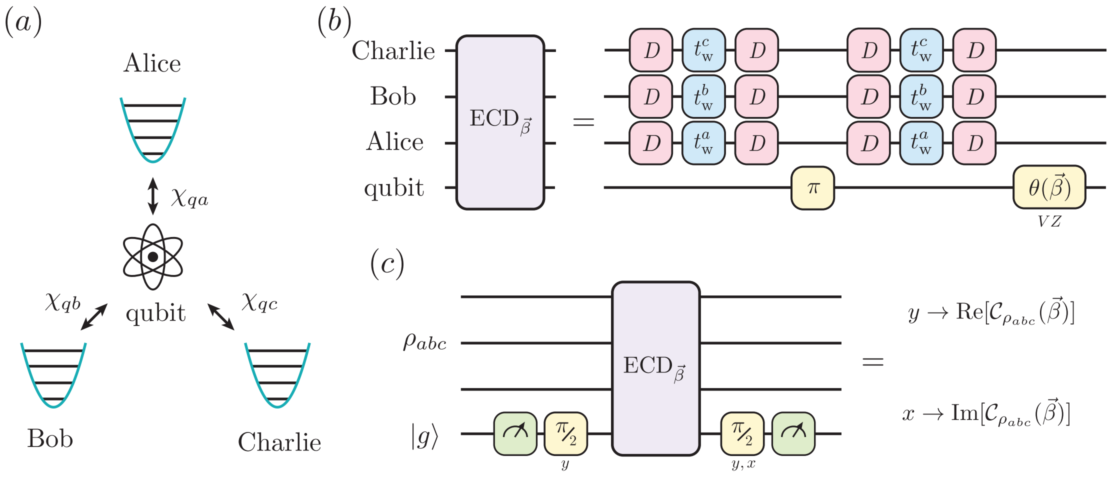

Figure 5.1: **Utility of ECD in one-to-all coupling architecture.** (a) Schematic of a one-to-all coupling architecture. Three QHOs are coupled to the same qubit with negligible coupling between them. We utilize this architecture to distribute entanglement between the QHO through the qubit. (b) Multimode ECD gate implementation in a one-to-all coupling architecture. The single-mode ECD gates are played in parallel, centered around the transmon echo pulse. The length of a multimode ECD gate is therefore the same as that of a single-mode ECD gate. (c) Utilizing the multimode ECD gate enables direct measurement of the multimode characteristic function without introducing additional complexity.

This Hamiltonian affords a natural extension of the ECD gate to a multimode architecture. We play a three-mode ECD gate by optimizing the individual ECD sequences and play them in parallel, centered around the qubit echo pulse. Fig. 5.1 (b) shows the corresponding circuit diagram. After the sequence, a virtual z rotation is applied to counter the accumulated geometrical phase on the qubit, as determined by running a three-mode cat-and-back experiment.

A key strength of multimode ECD gates is the ability to balance the effective coupling strengths across the modes through the appropriate selection of the displacement amplitudes within the ECD sequences. We can thus offset hardware mismatches in $\chi_{qa}$, $\chi_{qb}$, $\chi_{qc}$ and still achieve a uniform gate duration.

Critically, multimode tomography via joint characteristic function measurement, see Fig. 5.1 (c), does not add any complexity compared to the single mode case, a stark contrast to prior multimode architectures relying on joint parity measurements [149]. This remarkable multimode capacity of the ECD gate, retaining simple tune-up and the same gate time as single-mode operations, makes bosonic cQED architectures a particularly attractive platform for scalable multimode bosonic quantum error correction [154–156].

Following, we will demonstrate how to use the multimode ECD gate to implement a GHZ-cat and a W-cat state.

## 5.2 Protocols to create a GHZ-cat and W-cat

The goal of this experiment is the creation of tripartite entangled states of the microwave fields of superconducting cavities. Our first state of interest is the GHZ-cat state, which we define as:

$$|GHZ_{\text{cat}}\rangle \approx ete\,|0\rangle_a\,|0\rangle_b\,|0\rangle_c$$

, followed by a three-mode ECD gate that entangles all cavities to the qubit in a single step

$$\approx \frac{1}{\sqrt{2}}\left(|g\rangle\,|\alpha\rangle_a\,|\alpha\rangle_b\,|\alpha\rangle_c + |e\rangle\,|-\alpha\rangle_a\,|-\alpha\rangle_b\,|-\alpha\rangle_c\right). \tag{5.3}$$

At this point, we distributed the components of the multimode GHZ-cat state onto the qubit states. Then, we use a $\pi/2$ rotation to collect the components on $|g\rangle$ and finally collapse the qubit on $|g\rangle$ through a post-selection measurement, giving rise to the GHZ-cat state in the cavities.

The W-cat state has a fundamentally different entanglement structure compared to the GHZ-cat state. Rather than a two-component superposition, the W-state consists of three components.

$$|W_{\text{cat}}\rangle \approx \frac{1}{\sqrt{3}}\left(|\alpha\rangle_a\,|-\alpha\rangle_b\,|-\alpha\rangle_c + |-\alpha\rangle_a\,|\alpha\rangle_b\,|-\alpha\rangle_c + |-\alpha\rangle_a\,|-\alpha\rangle_b\,|\alpha\rangle_c\right) \tag{5.4}$$

To create this state using the distribution and collection strategy, we face an immediate challenge. Three components require three qubit states to store them. Consequently, we need to incorporate the third qubit level $|f\rangle$ into the state creation sequence. However, the action of the ECD gate is confined to the g-e subspace, prompting us to develop the Uneven Echo Conditional Displacement (UECD) transfer. The UECD transfer extends our toolkit by enabling us to create displacements on the cavity conditioned on the qubit being in the $|g\rangle$ or $|f\rangle$ state, while leaving the component on $|e\rangle$ untouched. This provides the additional degree of freedom required to create the W-cat state.

The effective action of the UECD transfer for our W-cat state creation protocol can be summarized as:

$$\boldsymbol{UECD}(\beta,\alpha_0) = \boldsymbol{D}(\beta/2)\,|f\rangle\,\langle g| + \boldsymbol{I}\,|e\rangle\,\langle e| + \boldsymbol{D}(-\beta/2)\,|g\rangle\,\langle f| \tag{5.5}$$

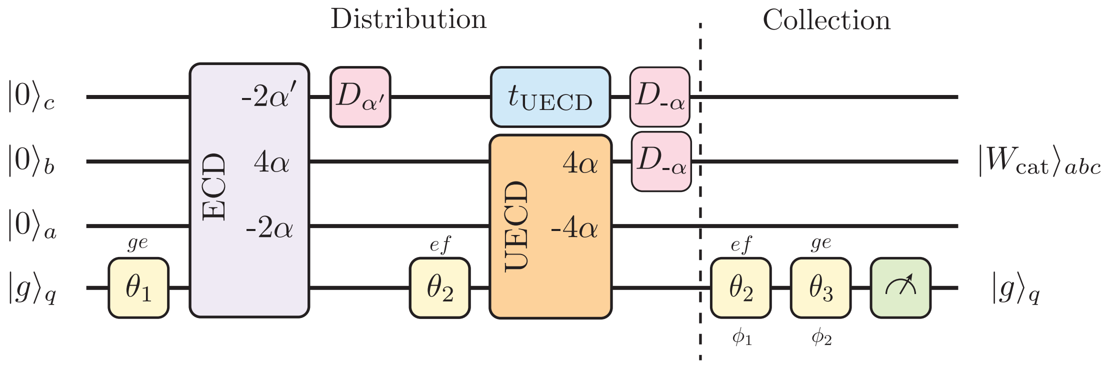

Figure 5.2: **W-cat state creation protocol.** The W-cat state protocol consists of two steps: distribution and collection. During distribution, a three-mode ECD and a UECD map the three W-cat state components onto the qubit states $|g\rangle$, $|e\rangle$, and $|f\rangle$. In the collection step, two transmon rotations transfer the three W-cat state components to $|g\rangle$ followed by a post-selection measurement to create the W-cat. We calibrate the rotation axis of the transmon pulses through cat-and-back experiments to null the accumulated geometric phase during the ECD and UECD sequence. Simulations of this sequence achieve fidelities $> 99\,\%$ with respect to the target state.

where $\alpha_0$ indicates that this is a state transfer and thus an initial state-dependent process.

The complete W-state protocol, shown in Fig. 5.2, leverages the UECD in a carefully orchestrated sequence. Starting from the in qubit ground state and vacuum in all cavities, we first bring the qubit into the state $\sqrt{\frac{2}{3}}\,|g\rangle + \sqrt{\frac{1}{3}}\,|e\rangle$. These amplitudes are with the correct probability amplitude ratios for the W-state in mind. We then play a three-mode ECD gate along with an unconditional displacement on Charlie, leaving us in the state:

$$\approx \sqrt{\frac{1}{3}}\,|g\rangle\,|\alpha\rangle_a\,|-2\alpha\rangle_b\,|2\alpha'\rangle_c + \sqrt{\frac{2}{3}}\,|e\rangle\,|-\alpha\rangle_a\,|2\alpha\rangle_b\,|0\rangle_c \tag{5.6}$$

where we chose $\alpha' = \alpha e^{i\chi_{ge}t_{\text{UECD}}/2}$ to counter the natural evolution the mode will undergo while the UECD is applied to the other two. Now we involve the third qubit level through a $\pi/2$-ef pulse followed by a UECD gate acting on Alice and Bob. After two more unconditional displacements on Bob and Charlie, we find the three desired W-cat components mapped onto the three qubit levels.

$$\approx \sqrt{\frac{1}{3}}\left(|g\rangle\,|\alpha\rangle_a\,|-\alpha\rangle_b\,|-\alpha\rangle_c + |e\rangle\,|-\alpha\rangle_a\,|\alpha\rangle_b\,|-\alpha\rangle_c + |f\rangle\,|-\alpha\rangle_a\,|-\alpha\rangle_b\,|\alpha\rangle_c\right). \tag{5.7}$$

The final stage employs carefully calibrated qubit rotations to map all three cavity components onto $|g\rangle$, followed by a post-selection measurement that collapses the system into the W-cat

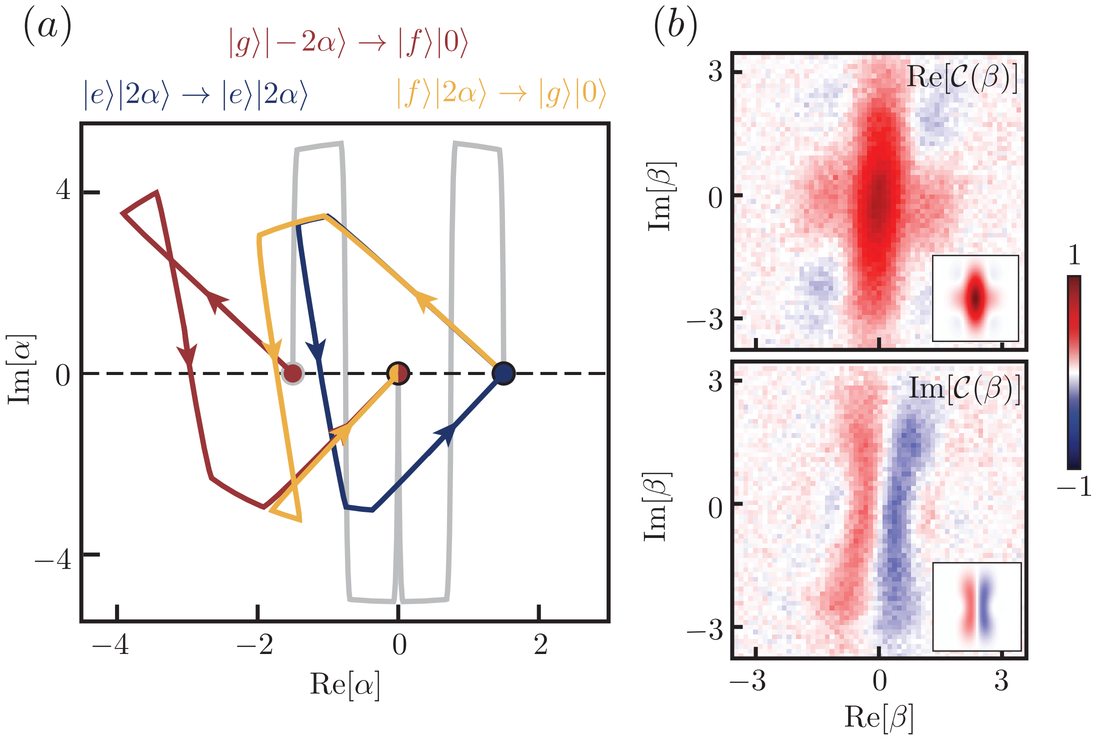

Figure 5.3: **Demonstration of ECD-UECD sequence** (a) Depiction of the phase space trajectory of mode A during the ECD-UECD sequence. An ECD gate (grey) displaces the cavity conditioned on $|g\rangle$ and $|e\rangle$. The UECD gate then returns the cavity component starting with qubit in $|g\rangle$ (red) and $|f\rangle$ (yellow) back to vacuum. The $|e\rangle$ component (blue) returns to its starting point. (b) Comparison between measured characteristic functions and theoretically generated characteristic functions (insets) of the state $|\psi\rangle \approx \sqrt{\frac{1}{3}}\,|0\rangle + \sqrt{\frac{2}{3}}\,|\alpha = 1.5\rangle$, created by the ECD-UECD sequence. The close agreement demonstrates the precise three-level control necessary for creating the W-cat state.

state. The rotation axes of the final qubit pulses are chosen to account for the geometrical phases accumulated during the ECD and UECD operation. With the sequence established, the remaining question is how to implement the UECD transfer.

Implementing the UECD gate presents a challenging task. The ECD gate employs a balanced frequency shift $\chi/2, -\chi/2$ for $|g\rangle$ and $|e\rangle$ respectively, leading to a symmetric phase space trajectory. Involving $|f\rangle$ breaks this balance. The three-level Hamiltonian can be written as:

$$\frac{\boldsymbol{H}_{UECD}}{\hbar} = \frac{\chi^{ge}}{2}\boldsymbol{a}^\dagger\boldsymbol{a}\,|g\rangle\langle g| - \frac{\chi^{ge}}{2}\boldsymbol{a}^\dagger\boldsymbol{a}\,|e\rangle\langle e| - (\chi^{gf} - \frac{\chi^{ge}}{2})\boldsymbol{a}^\dagger\boldsymbol{a}\,|f\rangle\langle f| \tag{5.8}$$

The challenge arises from the fact that $\chi^{gf} > \chi^{ge}$, causing the cavity states entangled to $|f\rangle$ to rotate faster than the states entangled to $|g\rangle$ or $|e\rangle$. This uneven evolution, after which the gate is named, would destroy the well-balanced phase space evolution upon which the ECD gate is built, if uncompensated.

To achieve the desired UECD operation despite the uneven dynamics, we employ optimization of the phase space trajectories. We start by imposing a pulse structure that mimics the default ECD gate. The sequences consist of four displacements, two wait times, and a $\pi$ pulse in the middle. The length of the pulses and the wait time $t_\mathrm{w}$ are fixed. We parametrize the problem in terms of six optimization variables. A global amplitude and phase $\varepsilon_0, \phi_0$ that is multiplied by all pulses, an amplitude and phase that is applied to the second and third pulse $\varepsilon_{23}, \phi_{23}$, and another amplitude and phase for the final displacement $\varepsilon_4, \phi_4$

Based on this parameterization, we use a Nelder-Mead optimization method to find the set of values $\{\varepsilon_0, \phi_0, \varepsilon_{23}, \phi_{23}, \varepsilon_4, \phi_4\}$ that minimize the cost function

$$C = |\alpha_g(T) - (\alpha_g(0) + \frac{\beta}{2})|^2 + |\alpha_e(T) - \alpha_e(0)|^2 + |\alpha_f(T) - (\alpha_f(0) - \frac{\beta}{2})|^2 \tag{5.9}$$

where $\alpha_{g,e,f}(T)$ represents the final cavity state for each qubit state and $\alpha_{g,e,f}(0)$ the initial state. This cost function enforces the wanted conditional displacements $+\frac{\beta}{2}$ for the trajectory starting in $|g\rangle$ and $-\frac{\beta}{2}$ for the trajectory starting in $|f\rangle$, with no displacement on $|e\rangle$. The trajectories are found through the integration of the semi-classical trajectories, expanded to the third qubit level. Using this cost function, we find the pulse sequence $\varepsilon_\mathrm{UECD}(t)$ that implements the gate specified in Equation 5.5. As with the ECD gate, we must be careful to predict and correct the accumulated geometric phases. We find them by solving the integral:

$$\theta_{g,e,f} = \int_0^T \mathrm{Im}[-i\varepsilon_\mathrm{UECD}\alpha^*_{g,e,f}(t)]dt \tag{5.10}$$

A derivation of this equation is given in Appendix D.

Fig. 5.3 provides experimental validation of the UECD gates performance. Panel (a) shows the phase space trajectories of the ECD-UECD sequence as played in the W-cat state protocol on Bob. First, an ECD gate (grey trajectory) followed by a $\pi/2$-ef pulse creates the state $\sqrt{\frac{1}{3}}\,(|g\rangle\,|-2\alpha\rangle + |e\rangle\,|2\alpha\rangle + |f\rangle\,|2\alpha\rangle)$. The following UECD gate then returns the cavity components that started with the qubit in $|g\rangle$ (red trajectory) and $|f\rangle$ (yellow trajectory) to vacuum, while the cavity components of $|e\rangle$ (blue trajectory) remain unchanged. Panel (b) presents experimental data of a characteristic function measurement after the whole sequence is played, including the last two qubit rotations and post-selection measurement. The measured data (main plot) shows excellent agreement with the ideal data (insets).

To validate the complete W-cat creation protocol, we perform a full pulse-level Hamiltonian simulation using the displaced frame technique introduced in section 3.2. The simulated W-cat state achieves a fidelity exceeding $99\%$, compared to the ideal target state shown in Equation 5.4. This clearly demonstrates the validity of our protocol to create a W-cat state.

Having established protocols to implement both a GHZ-cat state and a W-cat state, we now turn to the next challenging problem. How can we efficiently characterize states distributed across three bosonic modes, living in an 8D phase space?

## 5.3 Efficient tomography of multimode entangled cats

Tomography of bosonic systems is a challenging task that quickly becomes intractable as the system size increases exponentially with the number of modes. For a single mode, we need to measure $d = N_{\text{cutoff}}^2$ phase space points to reconstruct the density matrix, where $N_{\text{cutoff}}$ is our chosen Hilbert space in which the state is well contained, e.g., with $\leq 0.1\%$ of photons cut off. For a coherent state of size $|\alpha| = 1.8$, this requires $N_{\text{cutoff}} = 10$ for a single mode and consequently $N_{\text{cutoff}} = 10^3 \rightarrow d = 10^6$ measurements of the 8D three-mode characteristic function

$$\mathcal{C}(\beta_a, \beta_b, \beta_c) = \langle \boldsymbol{D}_a, \boldsymbol{D}_b, \boldsymbol{D}_c \rangle \tag{5.11}$$

$$= \text{tr}\left(\boldsymbol{D}_a, \boldsymbol{D}_b, \boldsymbol{D}_c \rho\right) \tag{5.12}$$

Using this brute-force method with our current capabilities will take between hours and days, during which we are vulnerable to parameter drifts, lowering fidelity.

We circumvent this problem by exploiting the de facto orthogonality of coherent states with $|\alpha| \geq 1.5 \rightarrow \langle -\alpha | \alpha \rangle \leq 0.01.$. This allows us to treat the $|\alpha\rangle$ and $|-\alpha\rangle$ as logical states forming a 2-dimensional subspace. Consequently, this significantly brings down the tomography requirements from $10^6$ phase space points for three bosonic modes to $64$ Pauli operators for the three-qubit state. A similar approach based on the Wigner function has been used in Ref. [97].

Under this encoding, we can write the Pauli operators as:

$$\boldsymbol{I} \approx |-\alpha\rangle\langle-\alpha| + |\alpha\rangle\langle\alpha| \tag{5.13}$$

$$\boldsymbol{X} \approx |\alpha\rangle\langle-\alpha| + |-\alpha\rangle\langle\alpha| \tag{5.14}$$

$$\boldsymbol{Y} \approx i|\alpha\rangle\langle-\alpha| - i|-\alpha\rangle\langle\alpha| \tag{5.15}$$

$$\boldsymbol{Z} \approx |-\alpha\rangle\langle-\alpha| - |\alpha\rangle\langle\alpha| \tag{5.16}$$

Following, I will go through one example that demonstrates how to find the mapping between these operators and the corresponding points in the characteristic function for $\langle\boldsymbol{X}\rangle$. $\boldsymbol{X}$ transforms $|\alpha\rangle$ to $|-\alpha\rangle$. This is the action of the displacement operator $\boldsymbol{D}_{-2\alpha}$. The key is to realize that while the construction $\boldsymbol{D}_{2\alpha} + \boldsymbol{D}_{-2\alpha}$ does not equal $\boldsymbol{X}$, as it also maps codewords out of the codespace, it yields the same expectation value. We can thus write $\langle\boldsymbol{X}\rangle = \langle\boldsymbol{D}_{2\alpha} + \boldsymbol{D}_{-2\alpha}\rangle = 2\mathrm{Re}[\mathcal{C}(2\alpha)]$. Following similar arguments, we find the mappings for each Pauli expectation value and the characteristic function points as:

$$\langle\boldsymbol{I}\rangle \approx \frac{1}{2}\langle\boldsymbol{D}_0 + \boldsymbol{D}_0^\dagger\rangle = \mathrm{Re}[\langle\boldsymbol{D}_0\rangle] = \mathrm{Re}[\mathcal{C}(0))] \tag{5.17}$$

$$\langle\boldsymbol{X}\rangle \approx \langle\boldsymbol{D}_{2\alpha} + \boldsymbol{D}_{-2\alpha}\rangle = 2\mathrm{Re}[\langle\boldsymbol{D}_{2\alpha}\rangle] = 2\mathrm{Re}[\mathcal{C}(2\alpha))] \tag{5.18}$$

$$\langle\boldsymbol{Y}\rangle \approx i\langle\boldsymbol{D}_{-2\alpha} - \boldsymbol{D}_{2\alpha}\rangle = 2\mathrm{Im}[\langle\boldsymbol{D}_{-2\alpha}\rangle]) = 2\mathrm{Im}[\mathcal{C}(-2\alpha)] \tag{5.19}$$

$$\langle\boldsymbol{Z}\rangle \approx s * i\langle\boldsymbol{D}_{-\frac{i\pi}{4\alpha}} - \boldsymbol{D}_{\frac{i\pi}{4\alpha}}\rangle = s * \mathrm{Im}[\langle\boldsymbol{D}_{-\frac{i\pi}{4\alpha}}\rangle] \tag{5.20}$$

where $s = \frac{1}{2}e^{-\left(\frac{\pi}{4\alpha}\right)^2/2}$ is a scaling factor to ensure that the expectation value is in the range $\pm 1$. We are thus able to measure the entire Pauli set $\{\boldsymbol{I}, \boldsymbol{X}, \boldsymbol{Y}, \boldsymbol{Z}\}$ by probing different points in the characteristic function.

A visual example for the state $|\psi\rangle = \mathcal{N}\left(|\alpha\rangle + i\,|-\alpha\rangle\right)$ is shown in Fig. 5.4. $\langle\boldsymbol{I}\rangle$ is simply the origin of the real part of the characteristic function, which by definition is the overlap of a state with itself and always $1$. $\langle\boldsymbol{X}\rangle$ and $\langle\boldsymbol{Y}\rangle$ are found by probing the center points of the cats' interference blobs. Depending on the phase of the cat state, these blobs will either appear in the real or imaginary part of the characteristic function. Finally, $\langle\boldsymbol{Z}\rangle$ distinguishes between $|\alpha\rangle$ and $|-\alpha\rangle$ by probing the sine that appears in the imaginary part of the characteristic function.

To characterize a three-mode state with this strategy, we have to break each three-mode Pauli operator into multiple characteristic function points. Instead of calculating this in a brute-force manner, we utilize the underlying structure of these operators and then generalize it. For one mode, each Pauli operator corresponds to one point in the characteristic function. The

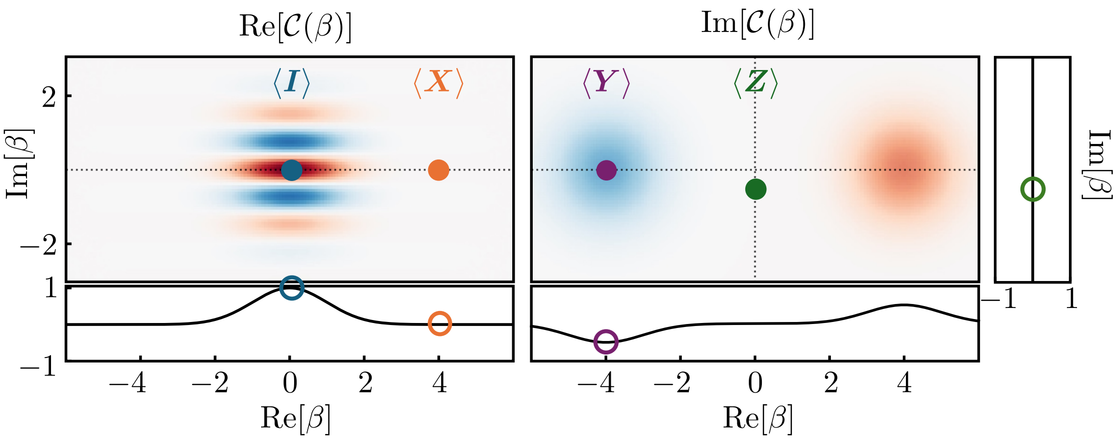

Figure 5.4: **Mapping Pauli operators onto characteristic function points.** For efficient tomography, we map points in the characteristic function to Pauli expectation values defined in the subspace $\{|\alpha\rangle, |-\alpha\rangle\}$. This allows us to characterize the full state using only four measurements. The depicted state is $\mathcal{N}(|\alpha\rangle + i|-\alpha\rangle)$, an eigenstate of $\boldsymbol{Y}$. As expected, $\langle\boldsymbol{X}\rangle$ and $\langle\boldsymbol{Z}\rangle$ give zero while $\langle\boldsymbol{Y}\rangle$ gives -1.

expectation value of different Pauli operators corresponds to different displacement values and whether the point is in the real or imaginary part of the characteristic function. We condense this into a single expression shown in the equation below

$$\langle\Sigma\rangle \approx s * i^k[\langle\boldsymbol{D}_\gamma + (-1)^k\boldsymbol{D}_{-\gamma}\rangle] \tag{5.21}$$

Here, $\Sigma$ represents the Pauli operator, $s$ is the corresponding scaling factor, $k$ encodes whether the point is in the real or imaginary characteristic function, and $\gamma$ encodes the location of the point. A mapping between the Pauli operators and the corresponding $\{s, k, \gamma\}$ set is shown in Table. 5.1.

| $\Sigma$ | $s$ | $k$ | $\gamma$ |
|---|---|---|---|
| $I$ | $1/2$ | 0 | 0 |
| $X$ | 1 | 0 | $2\alpha$ |
| $Y$ | 1 | 1 | $-2\alpha$ |
| $Z$ | $(1/2)\,e^{\left(\frac{\pi}{4\alpha}\right)^2/2}$ | 1 | $-i\pi/4\alpha$ |

Table 5.1: **Mapping parameters.** We map each Pauli expectation value to one point in the characteristic function. This table provides the mapping parameters that specify the scaling $s$, whether to measure the real or imaginary part of the characteristic function $k$, and the location of the point $\gamma$.

Considering that operators on different cavities commute, we can generalize Equation 5.21 to three modes

$$\begin{aligned}
\langle \Sigma_1 \Sigma_2 \Sigma_3 \rangle =& s_1 i^{k_1} [\langle \boldsymbol{D}_{\gamma_1} + (-1)^{k_1} \boldsymbol{D}_{-\gamma_1} \rangle] \\
& * s_2 i^{k_2} [\langle \boldsymbol{D}_{\gamma_2} + (-1)^{k_2} \boldsymbol{D}_{-\gamma_2} \rangle] \\
& * s_3 i^{k_3} [\langle \boldsymbol{D}_{\gamma_3} + (-1)^{k_3} \boldsymbol{D}_{-\gamma_3} \rangle] \\
=& s_{123} i^{k_{123}} (\langle \boldsymbol{D}_{\gamma_1 \gamma_2 \gamma_3} \rangle + (-1)^{k_{123}} \langle \boldsymbol{D}_{-\gamma_1 - \gamma_2 - \gamma_3} \rangle \\
& + (-1)^{k_1} \langle \boldsymbol{D}_{-\gamma_1 \gamma_2 \gamma_3} \rangle + (-1)^{k_{23}} \langle \boldsymbol{D}_{\gamma_1 - \gamma_2 - \gamma_3} \rangle \\
& + (-1)^{k_2} \langle \boldsymbol{D}_{\gamma_1 - \gamma_2 \gamma_3} \rangle + (-1)^{k_{13}} \langle \boldsymbol{D}_{-\gamma_1 \gamma_2 - \gamma_3} \rangle \\
& + (-1)^{k_3} \langle \boldsymbol{D}_{\gamma_1 \gamma_2 - \gamma_3} \rangle + (-1)^{k_{12}} \langle \boldsymbol{D}_{-\gamma_1 - \gamma_2 \gamma_3} \rangle)
\end{aligned} \tag{5.22}$$

where $s_{123} = s_1 * s_2 * s_3$, $k_{123} = k_1 + k_2 + k_3$ and $\boldsymbol{D}_{\gamma_1 \gamma_2 \gamma_3} = \boldsymbol{D}_{\gamma_1} \boldsymbol{D}_{\gamma_2} \boldsymbol{D}_{\gamma_3}$. Importantly, the displacement operators are paired in a way that, depending on $\vec{k}$, will yield either the real or imaginary part of $\boldsymbol{D}$. It is therefore apparent that every three-mode Pauli expectation value is mapped to four points in the 8D characteristic function. To simulate or measure any given three-mode Pauli operator, we use the last expression in Equation 5.22 combined with the parameter mapping found in Table 5.1 to determine the displacement points, scaling factors, and how to sum the points.

Up to this point, I have demonstrated how we can utilize a one-to-all coupling architecture to generate a GHZ-cat and a W-cat state, and I have shown a method to perform tomography on these states efficiently. In the next section, I will introduce the device we will use to implement and measure these three-mode entangled states.

## 5.4 Experimental setup

Our experimental setup implements a one-to-all coupling architecture where three bosonic modes are weakly dispersively coupled to a single transmon. Fig. 5.5 (a) shows the chip arrangement while (b) and (c) provide a top-down and an isometric view of the package design.

The bosonic modes are realized using compact on-chip tantalum hairpin resonators, which have demonstrated lifetimes of up to milliseconds [157]. Furthermore, their fundamental mode is primarily located between the arms of the hairpin, which limits unwanted coupling to other modes and minimizes inter-cavity coupling. The following paragraph on the chip fabrication is contributed by my team member, May Chee Loke, who fabricated the hairpin chips.

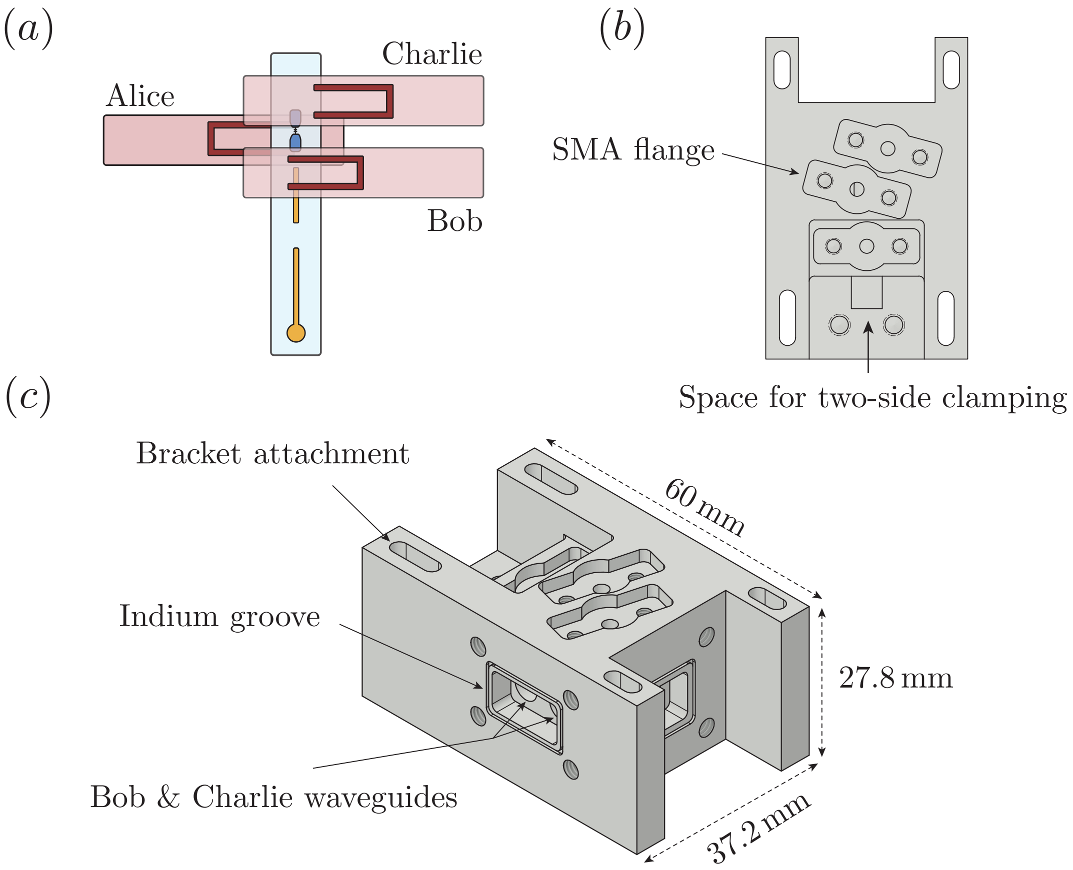

Figure 5.5: **Multimode package.** (a) Three on-chip tantalum hairpin resonators (red) are coupled to the same transmon (blue). Two hairpin chips are above, and one is below the transmon chip. (b) Top-down and (c) isometric view of the package. It hosts four waveguides, each with its own chips and SMA connectors for coupling. The chips are vertically clamped at one end. The clamp is then mounted onto the device with screws and made light-tight with indium. To suppress vibrations of the long transmon chip, we extend the chip onto an open plateau and secure it there with indium before sealing the enclosure.

To ensure consistent access to $\alpha$-phase tantalum, we use purchased 200 nm tantalum film deposited on HEMEX wafers from STAR Cryoelectronics. This allows us to eliminate the uncontrollable factor of deposition conditions in a shared facility. Before photolithography, the wafer is spin-coated with photoresist AZ1512 and baked at 100 °C for 1 minute. The film is then patterned with DMO Microwriter ML3 Pro, followed by development in MF319 for 40 s and DI water for 1 minute. Then comes the most crucial part of the fabrication process of the tantalum hairpin, that is the dry etching of the tantalum that is not covered by the mask with inductively coupled reactive ion etching using the Oxford ICP-RIE. We used the chlorine-based dry etch, following the recipe outlined in Ref. [158], to ensure a sharp and clean edge on the hairpin resonator. The film is etched with the following condition: chlorine and argon flow of 5 sccm each, ICP and HF power of 500 W and 50 W respectively, and background pressure of 5.4 mTorr at 10 °C. After dry etching, the resist is stripped off with NMP at 80 °C for 2 hours, followed by cleaning in acetone and methanol. A final thorough chemical processing with piranha is then performed again for the same duration mentioned earlier to remove fabrication residue.

We achieve one-to-all coupling through a stacked geometry, positioning hairpin chips above and below the transmon chip, with the open ends, where the hairpin field is strongest, oriented towards the transmon to achieve the required capacitive coupling. We use Ansys HFSS to simulate the fields and extract the Hamiltonian parameters using an energy participation method [159]. We optimize the frequencies and geometries until we achieve the desired couplings.

The transmon is capacitively coupled to an aluminum stripline resonator, which in turn is coupled to an aluminum Purcell filter. This configuration enables both transmon control and readout through a single port while preserving the transmon's coherence. Each hairpin is individually addressable through a dedicated 50 Ω terminated transmission line that is directly coupled to our room temperature control electronics, not shown in the chip arrangement.

The chips are fixed between two 6061 aluminum clamps, which are bolted together through screws. Additionally, Indium is used to ensure that the chips are held in place. The clamps are then mounted onto the device using screws and indium to make it light-tight. The long transmon chip raises concerns about mechanical stability, as vibrations of the chip lead to dephasing. To prevent this, we extend the transmon chip onto an open plateau, see the bottom of Fig. 5.5 (b), and secure it with indium before sealing the closure. Initially, attempts using Teflon cylinders and beryllium copper springs for mechanical clamping led to thermalization issues, prompting the use of indium wire instead.

Fig. 5.6 shows the wiring diagram of our experimental setup. The main challenge of the experimental setup is the synchronous control of five modes, each requiring its own dedicated control line. For this, we use a field-programmable gate array (FPGA) from Quantum Machines. The FPGA comes with five IQ port pairs, which use Digital-to-Analog converters to create pulses with a 350 MHz bandwidth. The control pulses are generated by mixing the intermediate frequency IQ pairs with a local oscillator (LO) in the GHz range. Before reaching the device, the signals are filtered and attenuated at the different temperature stages in our cryogenic environment.

The reflected measurement signal is first amplified at the 4 K stage through a HEMT and then further amplified at room temperature. The signal is then down-converted through an IR-Mixer with the same LO used for up-conversion. Finally, the down-converted signal is sampled through the Analog-to-Digital converter of the FPGA. The digitized signal is then demodulated and integrated using integration weights, and the information is condensed into a single point in the IQ plane. This value is compared against a threshold value and assigned a value of either 0 or 1, carrying the information of the qubit state.

The device itself is mounted on a specially designed copper bracket and placed inside a Cryoperm shield to protect it from electromagnetic noise. This setup is then mounted at the base plate of a dilution refrigerator. To further improve the thermalization of the device, we attach OFHC copper braids to it and anchor them at the base plate.

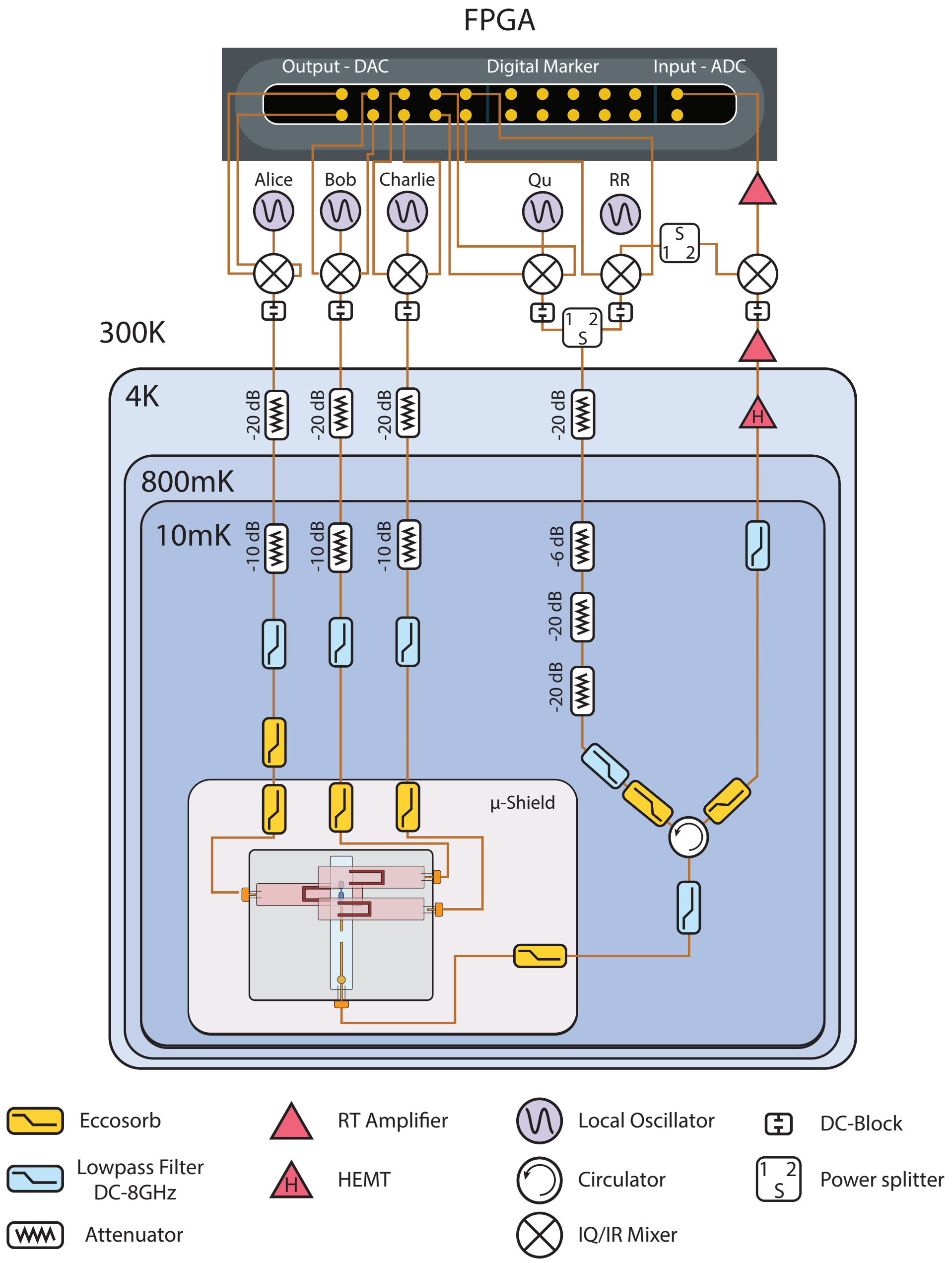

Figure 5.6: **Wiring diagram.** Wiring diagram of our preliminary experimental setup. All reported Hamiltonian and coherence parameters are measured using this setup.

The measured Hamiltonian parameters of our current setup are summarized in Table 5.2. The transmon and readout frequencies are measured using standard spectroscopy, while the cavity frequencies, $\chi$'s, and cavity self-Kerr's are found through out-and-back measurements as detailed in Chapter 3. Cavity-readout crosstalk is estimated by monitoring the readout shift induced by large cavity displacements. The spurious cavity-cavity coupling is inferred from HFSS simulations that show good correspondence with the measured Hamiltonian parameters.

| | Frequency (GHz) | Nonlinear interactions (kHz) | | | |
|---|---|---|---|---|---|
| | Frequency | Alice | Bob | Charlie | RO |
| g-e | 5.32205 | 61 | 33 | 87 | 880 |
| e-f | 5.14035 | 104 | 47 | 145 | $\cdots$ |
| Alice | 6.49738 | $6.3 \times 10^{-3}$ | $\sim 2 \times 10^{-3}$ | $\sim 4 \times 10^{-3}$ | $\sim 1$ |
| Bob | 6.06904 | $\sim 2 \times 10^{-3}$ | $0.78 \times 10^{-3}$ | $\sim 2 \times 10^{-3}$ | $\sim 0.1$ |
| Charlie | 6.15605 | $\sim 4 \times 10^{-3}$ | $\sim 2 \times 10^{-3}$ | $12 \times 10^{-3}$ | 0.1 |
| RO | 7.78181 | $\sim 1$ | $\sim 0.1$ | $\sim 0.1$ | $\cdots$ |

Table 5.2: **Hamiltonian Parameters.** Measured Hamiltonian parameters of our one-to-all coupling architecture. The measured parameters are in good agreement with HFSS simulations. The dispersive shifts between qubit and cavities are all in the weak-dispersive coupling regime, resulting in negligible cavity self-Kerr values. Values with a tilde are below our measurement precision and taken from HFSS simulations.

The coherence properties of this system are summarized in Table 5.4. The transmon coherences are measured using standard experiments, while the cavity relaxation time is measured through the crosshair $T_1$ method introduced in section 3.3.3. While the Hamiltonian parameters and transmon coherences are suitable for the experiment, the cavity coherence properties present challenges. In particular, the cavity lifetimes measured in this setup are limited to approximately 100 μs, significantly below the demonstrated lifetimes for hairpin resonators in literature [69, 157] and also lower than previous iterations that reached lifetimes $\sim$ 300 μs.

| | $T_1$ (μs) | $T_2$ (μs) | $T_{2e}$ (μs) |
|---|---|---|---|
| g-e | 60 | 40 | 55 |
| e-f | 42 | 26 | 35 |
| Alice | 95 | $\cdots$ | $\cdots$ |
| Bob | 140 | $\cdots$ | $\cdots$ |
| Charlie | 113 | $\cdots$ | $\cdots$ |
| RO | 0.5 | $\cdots$ | $\cdots$ |

Table 5.3: **Coherence properties.** Coherence times of the current setup. While the transmon shows good coherence, the relatively low lifetimes of the cavities, $\sim$ 100-150 μs, require further optimization.

## 5.5 Preliminary results

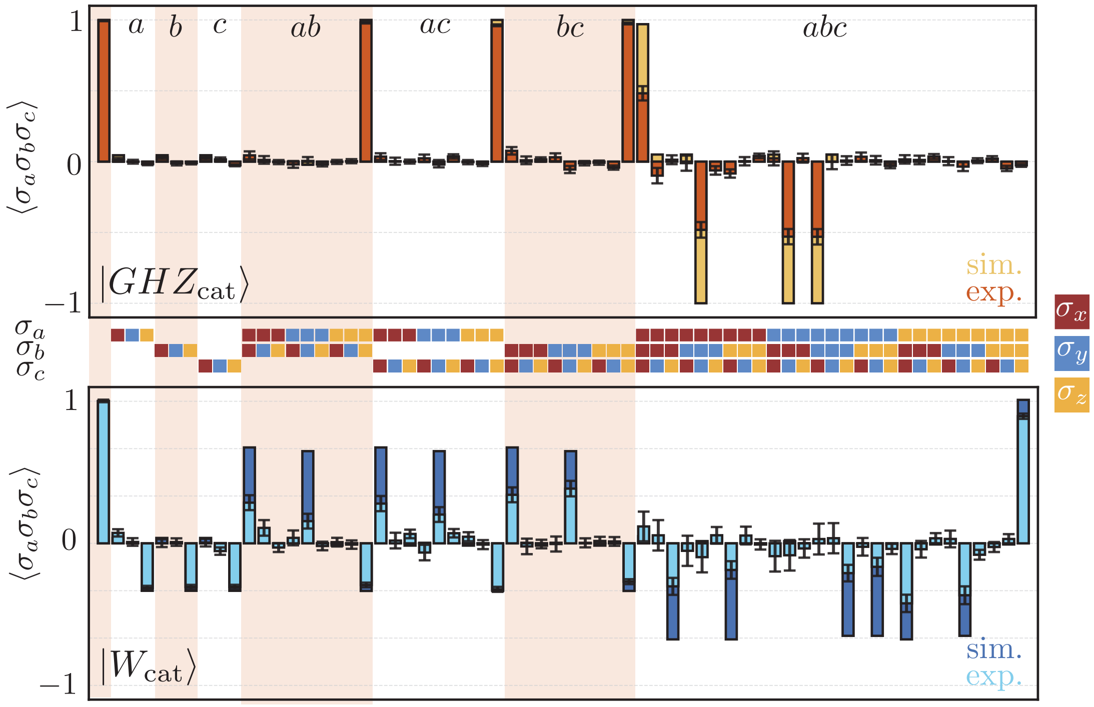

Figure 5.7: **Pauli expectation values of GHZ-cat and W-cat states for** $|\alpha| = 1.5$ Bars show pulse-level lossless simulations (orange, dark blue) and experimentally measured values (yellow, light blue) for all 64 three-qubit Pauli operators. Operators are grouped by the number of participating modes, as indicated by the orange/white regions. The distinct entanglement signatures of the two states are clearly visible. The GHZ-cat state exhibits only three-mode correlations with trivial two-mode correlators, while the W-cat state shows both significant two-mode and three-mode correlations. This difference reflects the robustness of W-cat entanglement; tracing out any single mode leaves the GHZ-cat in a completely mixed state, while the W-cat retains bipartite entanglement. Fidelities with respect to the ideal target states are $\mathcal{F}_{\text{GHZ}_{\text{cat}}} = (73 \pm 1.3)\,\%$ and $\mathcal{F}_{\text{W}_{\text{cat}}} = (57 \pm 1.6)\,\%$, calculated using density matrix reconstruction. Error bars represent statistical uncertainties obtained from 500 bootstrap rounds.

To verify our state-creation and tomography methods, we perform full-pulse Hamiltonian simulations using realistic device parameters. We use the displaced-frame transformation on each bosonic mode to make the computationally intensive simulation feasible, requiring a manageable Hilbert space dimension of approximately 20k for $\alpha = 1.5$. Fig. 5.7 shows the resulting Pauli fingerprints for the simulated W-cat (dark blue) and GHZ-cat (orange). Both show excellent agreement with the expected theoretical predictions. The slight deviations from the ideal values arise from the residual overlap between $|\alpha\rangle$ and $|-\alpha\rangle$ for $\alpha = 1.5$ of approximately $1\%$.

The Pauli fingerprints reveal the distinct entanglement signatures of the two states. The GHZ-cat displays clear 3-mode correlations with only trivial $ZZ$-type 2-mode correlations. Tracing out any single mode destroys all entanglement, leaving the system in a completely mixed state. In contrast, the W-cat exhibits a multitude of both 3-mode and 2-mode correlations. Even when 1 mode is traced out, bipartite entanglement remains between the other 2 modes, demonstrating the W-cat's robustness.

We present preliminary experimental data for the GHZ-cat (yellow bars) and W-cat state (light blue bars) at $\alpha = 1.5$ in Fig. 5.7. Both states are implemented through the protocols introduced at the beginning of this chapter. The distribution step for the GHZ-cat is dominated by the 3-mode ECD gate and takes approximately $2.5$ μs, while the ECD and UECD gates in the W-cat require larger displacements, bringing the gate time to approximately $2.8$ μs each, for a total distribution time of $5.6$ μs. The collection step is identical up to a single qubit pulse for both states and takes about $3.4$ μs, dominated by the post-selection measurement. Finally, we use an ECD gate with a small displacement amplitude to measure the real or imaginary part of the characteristic function in $4$ μs. The measured points are scaled against the contrast of $\mathrm{Re}[\mathcal{C}_{|\mathrm{vac}\rangle}(0,0,0)]$ to isolate state creation errors from measurement errors.

In both cases, the experimental data shows good correspondence with the simulated results, with the main deviations appearing in the amplitudes of Pauli operators corresponding to multimode coherences. The variation in coherence amplitudes for the W-cat can be attributed to the different modes participating in each correlator and their corresponding different loss channels. To quantify the quality of our states, we reconstruct the density matrices and compare them to the ideal target states. For the reconstruction, we use linear inversion with a unit trace constraint, followed by maximum-likelihood estimation to ensure physicality. We find fidelities of $\mathcal{F}_{\mathrm{GHZ_{cat}}} = (73 \pm 1.3)\,\%$ and $\mathcal{F}_{\mathrm{W_{cat}}} = (57 \pm 1.6)\,\%$. To estimate the statistical uncertainties in our Pauli construction and fidelity calculation, we perform $500$ bootstrap resamples of our data. The resulting uncertainties on the Pauli expectation values are shown as error bars in Fig. 5.7.

To assess whether we have successfully created genuine tripartite entanglement, we employ fidelity-based entanglement witnesses as introduced in Ref. [160]. They show that the fidelity of a GHZ state with any biseparable state, a state with at most $2$ systems entangled, cannot exceed $50\%$. Furthermore, a fidelity above $75\%$ strictly witnesses GHZ-type entanglement, whereas below $75\%$, no distinction between W-type and GHZ-type entanglement can be made.

For our measured fidelity of $\mathcal{F}_{\mathrm{GHZ}_{\mathrm{cat}}} = (73 \pm 1.3)\,\%$, the GHZ-cat demonstrates genuine tripartite entanglement but falls short of witnessing strict GHZ-type entanglement. Similarly, for a W-state, a fidelity above $66.\bar{6}\%$ witnesses W-type entanglement. Our measured fidelity of $\mathcal{F}_{\mathrm{W}_{\mathrm{cat}}} = (57 \pm 1.6)\,\%$ is below this threshold. In summary, we observe genuine tripartite entanglement in the GHZ-cat state, yet further improvements are required to witness strict GHZ-type and W-type entanglement.

While these preliminary results establish proof of principle that our experimental hardware can implement multipartite entangled cat states, the reduced contrast in Pauli operators corresponding to multimode coherences, which translates to lower fidelities, reveals current hardware limitations. In the final section, I will analyze the impact of different decoherence mechanisms on state creation fidelities and use this analysis to chart a path forward to successfully complete this experiment.

## 5.6 Impact of decoherence

To quantify the impact of decoherence on the multipartite cat state creation fidelities, we run master equation simulations with parameters motivated by the device parameters used to create the GHZ-cat state. Full simulations of the protocol are computationally unfeasible, as the density matrices, even for modest-sized states with $\alpha = 1.5$, require several GB of memory. We circumvent this limitation by simulating the impact of decoherence on the states after the distribution step in each protocol, when the cavity states components are spread between the qubit states.

$$|GHZ_{\text{cat-distr}}\rangle \approx \frac{1}{\sqrt{2}}\left(|g\rangle\,|\alpha\rangle_a\,|\alpha\rangle_b\,|\alpha\rangle_c + |e\rangle\,|-\alpha\rangle_a\,|-\alpha\rangle_b\,|-\alpha\rangle_c\right) \tag{5.23}$$

$$|W_{\text{cat-distr}}\rangle \approx \frac{1}{\sqrt{3}}(|g\rangle\,|\alpha\rangle_a\,|-\alpha\rangle_b\,|-\alpha\rangle_c + |e\rangle\,|-\alpha\rangle_a\,|\alpha\rangle_b\,|-\alpha\rangle_c \tag{5.24}$$

$$+\,|f\rangle\,|-\alpha\rangle_a\,|-\alpha\rangle_b\,|\alpha\rangle_c) \tag{5.25}$$

After evolving these states under realistic noise conditions, we apply the collection step through gates and calculate fidelities with respect to the ideal $|GHZ_{\text{cat}}\rangle$ and $|W_{\text{cat}}\rangle$ states.

Fig. 5.8 shows the individual and combined effects of qubit decay $T_1^q$, qubit dephasing $T_\phi^q$, cavity decay $T_1^c$, and cavity dephasing $T_\phi^c$. We use measured parameters where available, with the cavity dephasing rate set much lower than the values reported in the literature [157].

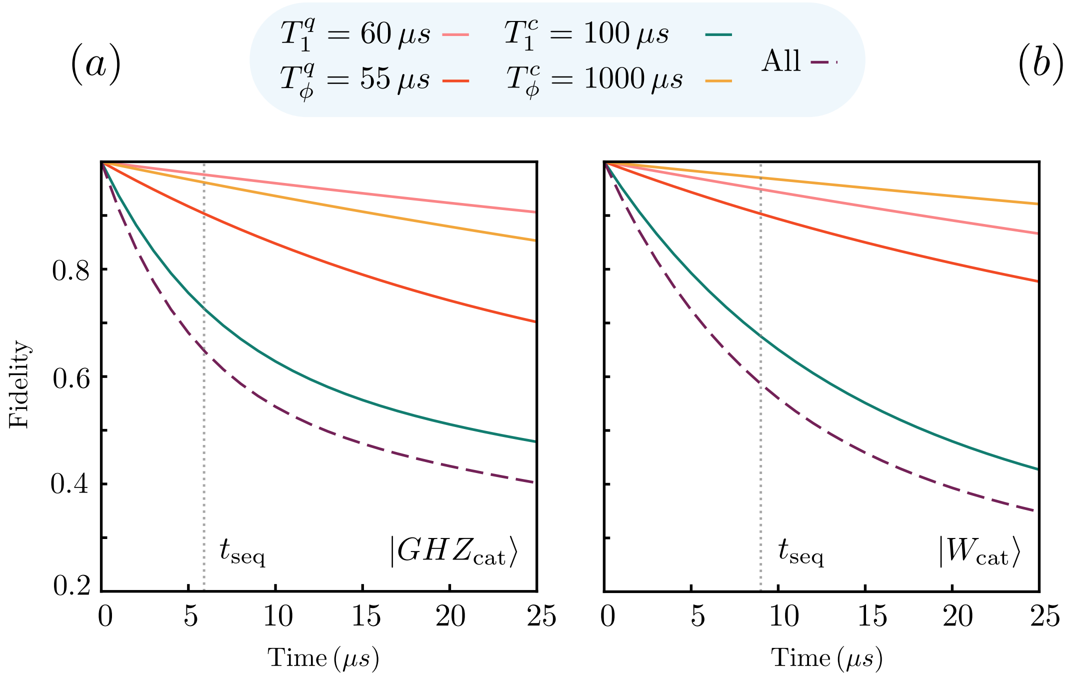

Figure 5.8: **Impact of decoherence during state creation.** Simulation results show the impact of qubit decay $T_1^q$, qubit dephasing $T_\phi^q$, cavity decay $T_1^c$, and cavity dephasing $T_\phi^c$ on the states $|\text{GHZ}_{\text{cat-distr}}\rangle$ (a) and $|\text{W}_{\text{cat-distr}}\rangle$ (b). The dotted vertical line indicates the length of the state creation sequence $t_{\text{seq}}$. Fidelities are calculated with respect to the ideal $|\text{GHZ}_{\text{cat}}\rangle$ and $|\text{W}_{\text{cat}}\rangle$ states after applying the collection step through gates. The dominant error mechanism for both states is cavity decay.

For the GHZ-cat, we find that the simulation overestimates the error with a fidelity of $64.8\%$ after $5.9$ µs, about $10\%$ lower than found from the experimental data. One explanation for this discrepancy is the fact the photon loss induced dephasing of the cat state is more relevant for the state after the distribution step compared to the evolving state during the distribution. This is backed by full protocol simulations on one and two modes. The same reasoning applies to the W-state, for which we find a fidelity after $9$ µs of $58\%$. Crucially, in both cases, we can identify photon loss as the dominant error mechanism, accounting for a $28\%$ drop in fidelity for the GHZ-cat and a $33\%$ drop for the W-cat state. Qubit dephasing follows second with about $10\%$ each.

The simulated results provide a clear insight into the low contrast observed in the measured GHZ-cat three-mode correlators. These correlators are constructed from characteristic function measurements at points like $\mathrm{Re}[\mathcal{C}(\pm 2\alpha, \pm 2\alpha, \pm 2\alpha)]$, which probe the multimode generalization of the coherence blobs whose fragility to photon loss was extensively discussed in chapter 4. Thus, their significant degradation is consistent with photon loss dominating the drop in fidelity.

This analysis reveals that a few improvements to key parameters have the potential to significantly improve the fidelity of the measured contrast of the Pauli expectation values. The identification of the dominant decoherence mechanisms provides a clear roadmap for optimization. Specifically, we need to optimize the post-selection time, gate durations, as well as the device parameters $T_1^c$ and $T_\phi^q$.

## 5.7 Discussion

This chapter establishes the experimental foundation for creating and studying multipartite entangled cat states in superconducting bosonic circuits. We successfully demonstrated the creation of a GHZ-cat state and developed the theoretical framework, which is now ready to be tested for the creation of a W-cat state. Part of the framework is the novel UECD transfer, which allows for conditional displacements with a qutrit. While the current device limits the achievable state creation fidelities, our theoretical discussion revealed specific improvements that can increase the quality of subsequent measurements.

Both, the GHZ-cat and W-cat data indicate, to the best of my knowledge, the creation of the first tripartite entangled cat states in bosonic cQED. The fidelity for the GHZ-cat witnesses genuine tripartite entanglement, yet the fidelities for both states need further improvements to claim genuine GHZ-type and W-type entanglement.

Currently, the photon loss rate of the hairpins is the limiting factor. While previous iterations have shown that this hardware can achieve lifetimes above 250 µs current fabrication inconsistencies have prevented us from consistently achieving these lifetimes. The etching step is currently unstable, as the same parameters do not consistently achieve the same outcomes across different batches. Ongoing investigations suspect variations in thickness between the purchased films as well as unstable etching rates. Furthermore, we are exploring the implementation of more rigorous chemical processing protocols to treat the oxide, including those based on HF. Besides decreasing the photon loss rate, we can decrease the overall protocol length. Here, we are currently limited by time it takes to do the post-selection measurement, as well as by length of our displacement gates as we are maxing out the DAC amplitudes. Both of these issues can be addressed by increasing the length of the corresponding coupling pins in a next cooldown.

The combination of these protocol improvements project a GHZ-cat protocol duration of $\sim$ 3-4 μs and a W-cat protocol of $\sim$ 4-5 μs. With a qubit Hahn echo time of 60 μs and cavity lifetimes between 200-300 μs, we expect fidelities in the 80% range, leading to a significant improvement of the measured bipartite and tripartite correlators. These advancements should enable the utilization of these states in the exploration of multimode bosonic codes, quantum information protocols, and quantum sensing.

The broader impact of this work extends beyond the creation of multipartite entanglement. The bedrock of this work is the powerful multimode adaptability of the ECD-gate in a one-to-all coupling architecture. The trivial generalization of the ECD gate, in both control and tomography applications, demonstrates the power of hardware-aware protocol design philosophies, crucial for manipulating and probing ever larger quantum systems. I am looking forward to seeing these design principles put into practice, which will open the field to multimode bosonic codes with increased error-correction capabilities as already demonstrated in Ref. [155].

# Chapter 6

# Conclusion and outlook

Quantum computation has reached a critical juncture where the focus must shift from simply building more to engineering fundamentally better qubits. Recent work has shown that achieving lower error rates significantly improves logical performance, while scaling processors remains challenging [161, 162]. This paradigm shift highlights the brilliance of bosonic modes, harnessing the large Hilbert space of quantum harmonic oscillators to efficiently encode a logical qubit using a single physical element [163]. While several break-even experiments have consolidated the bosonic code approach as a serious contender [48, 52, 53], significant challenges to scaling remain.

Below, I will briefly review the main results of my thesis in the context of what I believe to be a promising path forward. This hardware-aware design philosophy emphasizes the co-development of theory and experiment for compound returns.

In the first experiment of this thesis, we demonstrate how awareness of the dominant error mechanisms of a quantum harmonic oscillator can be leveraged to construct intrinsically more robust bosonic codewords. In particular, we showed that phase space compression protects the coherence features of a cat state against photon loss, the dominant error mechanism in bosonic cQED cavities. Based on the understanding that photon loss acts as a Gaussian filter in reciprocal phase space, we used our compression protocol to shift the interference features below this filter, thereby protecting them. Our experimental results demonstrate a fivefold enhancement of effective lifetimes at a compression level of $-7.6$ dB.

The second experiment plays into this idea from a different angle. Recent results have shown that the combined Hilbert space of a multimode bosonic code may offer performance and scaling advantages over single-mode approaches [153–155], yet multimode control and characterization are challenging. We utilize the remarkable multimode capacity of the echo conditional displacement gate in a one-to-all coupling architecture to develop a testbed that allows the efficient implementation and characterization of multimode entangled bosonic cat states. In particular, we demonstrate genuine tripartite entanglement in our GHZ-cat state and data that hints at the creation of a W-cat state. While our fidelities fall short of claiming genuine GHZ-type and W-type entanglement, respectively, we identified the specific hardware improvements required to lift the fidelities above the bounds. Further, we developed an efficient tomography method that directly maps characteristic function points to Pauli expectation values, enabling practical verification of genuine tripartite entanglement.

The direct continuation to the presented data on tripartite entanglement is to improve the hardware to lift the fidelities above the bounds to claim both genuine GHZ-type and W-type entanglement. The provided analysis points the way ahead, and I am confident that we will succeed once we achieve higher cavity lifetimes.

The idea of reshaping the phase space distribution to enhance the protection of physical qubits against natural system errors has already been demonstrated in an impressive experiment. By implementing a scheme to dissipatively stabilize a squeezed cat qubit, they achieved a staggering 160-fold increase in bit flip time [126] of their logical squeezed cat qubit. What remains to be shown is the advantage of the squeezed cat qubits in a multi-qubit architecture to beat the threshold and create a hardware-aware logical qubit.

The developed multimode testbed and control techniques open up avenues for several interesting experiments. First, it directly opens the gate to probe the nature and utility of the different kinds of correlations tripartite entangled states offer and to utilize them for sensing and quantum information tasks [44, 153].

Another exciting direction is to implement and test the various multimode bosonic codes proposed. By leveraging the larger combined Hilbert space of multiple modes, these codes should, in principle, enable the correction of a broader class of errors, potentially relaxing the stringent overhead requirements that plague current quantum error correction approaches [155, 164, 165].

# Appendix A

# Derivation of the echo conditional displacement parameters

The echoed conditional displacement (ECD) gate is implemented through the action of the following Hamiltonian:

$$\frac{\boldsymbol{H}}{\hbar} = -\chi \boldsymbol{a}^\dagger \boldsymbol{a} \frac{\boldsymbol{\sigma}_z z(t)}{2} + \varepsilon^*(t)\boldsymbol{a} + \varepsilon(t)\boldsymbol{a}^\dagger \tag{A.1}$$

where $z(t) = \pm 1$ represents the sign of $\boldsymbol{\sigma}_z$ before and after the qubit $\pi$-pulse, $\chi$ is the dispersive coupling strength, and $\varepsilon(t)$ is the time-dependent cavity drive amplitude.

To solve the resulting time evolution of this Hamiltonian, we chose the following ansatz for the time evolution operator [99]:

$$\boldsymbol{U} = e^{i\theta\frac{\boldsymbol{\sigma}_z}{2}} e^{\boldsymbol{a}^\dagger(\gamma+\delta\boldsymbol{\sigma}_z) - \boldsymbol{a}(\gamma^*+\delta^*\boldsymbol{\sigma}_z)} e^{i\phi \boldsymbol{a}^\dagger \boldsymbol{a}\boldsymbol{\sigma}_z} \tag{A.2}$$

where $\theta(t)$, $\gamma(t)$, $\delta(t)$, and $\phi(t)$ are time-dependent parameters to be determined.

To find these parameters, we substitute $\boldsymbol{H}$ from eq. A.1 and $\boldsymbol{U}$ from eq. A.2 into the Schrödinger equation $i\hbar\frac{\partial \boldsymbol{U}}{\partial t} = \boldsymbol{H}\boldsymbol{U}$. First, we evaluate the left side, the time derivative of $\boldsymbol{U}$.

$$i\hbar\frac{\partial \boldsymbol{U}}{\partial t} = i\hbar(i\frac{\boldsymbol{\sigma}_z}{2}\partial_t\theta + \partial_t \boldsymbol{a}^\dagger\gamma + \boldsymbol{a}^\dagger\partial_t\gamma + \partial_t\boldsymbol{a}^\dagger\delta\boldsymbol{\sigma}_z \tag{A.3}$$

$$+ \boldsymbol{a}^\dagger\partial_t\delta\boldsymbol{\sigma}_z - \partial_t\boldsymbol{a}\gamma^* - \boldsymbol{a}\partial_t\gamma^* - \partial_t\boldsymbol{a}\delta^*\boldsymbol{\sigma}_z \tag{A.4}$$

$$- \boldsymbol{a}\partial_t\delta^*\boldsymbol{\sigma}_z + i\partial_t\phi\boldsymbol{a}^\dagger\boldsymbol{a}\boldsymbol{\sigma}_z + i\phi\partial_t\boldsymbol{a}^\dagger\boldsymbol{a}\boldsymbol{\sigma}_z + i\phi\boldsymbol{a}^\dagger\partial_t\boldsymbol{a}\boldsymbol{\sigma}_z)\boldsymbol{U} \tag{A.5}$$

As a result, we can cancel $\boldsymbol{U}$ on both sides of the equation. Furthermore, we need to calculate the time derivative $\boldsymbol{a}$, which is given by $\frac{\partial a}{\partial t} = -\frac{i}{\hbar}[\boldsymbol{H}, \boldsymbol{a}]$. After reordering the left-hand side and dividing by $\hbar$, we find

$$
\begin{aligned}
&-\varepsilon^*\gamma - \varepsilon\gamma^* + \boldsymbol{\sigma}_z\left(-\varepsilon^*\delta - \varepsilon\delta^* - \frac{\partial_t\theta}{2}\right) + \boldsymbol{a}^\dagger\boldsymbol{a}\boldsymbol{\sigma}_z(-\partial_t\phi) + \boldsymbol{a}^\dagger\boldsymbol{\sigma}_z\left(-\frac{\chi_z(t)\gamma}{2} + i\partial_t\delta + i\phi\varepsilon\right) \\
&+ \boldsymbol{a}\boldsymbol{\sigma}_z\left(-\frac{\chi_z(t)\gamma^*}{2} - i\partial_t\delta^* - i\phi\varepsilon^*\right) + \boldsymbol{a}^\dagger\left(-\frac{\chi_z(t)\delta}{2} + i\partial_t\gamma\right) + \boldsymbol{a}\left(-\frac{\chi_z(t)\delta^*}{2} - i\partial_t\gamma^*\right) \\
&= -\chi\boldsymbol{a}^\dagger\boldsymbol{a}\frac{\boldsymbol{\sigma}_z z(t)}{2} + \varepsilon\boldsymbol{a}^\dagger + \varepsilon^*\boldsymbol{a} \qquad \text{(A.6)}
\end{aligned}
$$

From here, we can find equations that determine the $\theta$, $\gamma$, $\delta$, $\phi$ by comparing the left and right sides by operators. This yields the following equations:

$$
\begin{aligned}
\frac{\partial\theta}{\partial t} &= -2\mathrm{Re}[\varepsilon^*\delta] && \text{(A.7)}\\
\frac{\partial\gamma}{\partial t} &= -i\frac{\chi}{2}z(t)\delta - i\varepsilon && \text{(A.8)}\\
\frac{\partial\delta}{\partial t} &= -i\frac{\chi}{2}z(t)\gamma - \phi && \text{(A.9)}\\
\frac{\partial\phi}{\partial t} &= -\frac{\chi}{2}z(t) && \text{(A.10)}
\end{aligned}
$$

Integrating these differential equations with initial conditions $\theta(0) = \gamma(0) = \delta(0) = \phi(0) = 0$, we obtain the solutions:

$$
\begin{aligned}
\theta(t) &= -2\int_0^t d\tau \mathrm{Re}[\varepsilon^*(\tau)\delta(\tau)] && \text{(3.5)}\\
\gamma(t) &= -i\int_0^t d\tau \cos[\phi(\tau) - \phi(t)]\varepsilon(\tau) && \text{(3.6)}\\
\delta(t) &= -\int_0^t d\tau \sin[\phi(\tau) - \phi(t)]\varepsilon(\tau) && \text{(3.7)}\\
\phi(t) &= -\frac{\chi}{2}\int_0^t d\tau z(\tau) && \text{(3.8)}
\end{aligned}
$$

During the sequence, a qubit $\pi$-pulse is applied at $t = T/2$, causing $z(t)$ to change sign. This ensures that $\phi(T) = 0$, eliminating the qubit state-dependent rotation of the oscillator. Finally, we use the Baker-Campbell-Hausdorff formula to rewrite the Unitary evolution operator as

$$
\boldsymbol{U} = \boldsymbol{\sigma}_x e^{i\theta'\boldsymbol{\sigma}_z/2}\boldsymbol{D}(\lambda)\boldsymbol{C}\boldsymbol{D}(\beta) \qquad \text{(A.11)}
$$

with $\theta' = \theta(T) + 2\mathrm{Im}[\gamma(T)\delta(T)]$, $\lambda = \gamma(T)$ and $\beta = 2\delta(T)$. The $\boldsymbol{\sigma}_x$ operator accounts for the qubit flip in the middle of the sequence.

To achieve a high-fidelity ECD gate, we have to account for the picked-up qubit phase and cancel the unwanted unconditional displacement. For the qubit phase, we can calibrate the phase and take it into account by applying a virtual $\sigma_z$ gate after we play an ECD gate. To cancel the unconditional displacement in the experiment where we are bound by amplitude and bandwidth constraints on our microwave drives, we use semiclassical trajectories to optimize the phase space trajectories.

# Appendix B

# Characteristic function measurement protocol

The characteristic function $\mathcal{C}(\beta) = \langle \boldsymbol{D}(\beta) \rangle$ provides a complete description of quantum states and serves as a fundamental tool for state characterization in circuit QED experiments.

The measurement protocol begins with the qubit in $|g\rangle$. A pre-selection measurement is helpful to ensure proper system initialization before executing the measurement sequence. The core sequence consists of a $\pi/2$ qubit rotation followed by the ECD operation $\boldsymbol{ECD}(\beta) = |e\rangle \langle g| \boldsymbol{D}(\beta/2) + |g\rangle \langle e| \boldsymbol{D}(-\beta/2)$, and concludes with a final $\pi/2$ rotation whose phase controls which quadrature of the characteristic function we measure.

Following the initial qubit rotation and ECD gate application, the combined qubit-cavity system evolves into the entangled state:

$$|\Psi\rangle = \frac{1}{\sqrt{2}} \left( |g\rangle |\psi_-\rangle + |e\rangle |\psi_+\rangle \right) \tag{B.1}$$

where I use the compact notation $|\psi_\pm\rangle = \boldsymbol{D}(\pm\beta/2) |\psi\rangle$ to represent the displaced cavity states.

To simplify the calculation, I decompose the cavity state space into orthogonal components. The first part is uniquely entangled with the qubit ground state, labeled $|\psi_g\rangle$, the next with the excited state, $|\psi_e\rangle$, and the last part is entangled with both $|\psi_{||}\rangle$.

This decomposition allows us to rewrite the system state as:

$$|\Psi\rangle = \frac{1}{\sqrt{2}} \left[ \gamma_{g-} |g\rangle |\psi_g\rangle + \gamma_{e+} |e\rangle |\psi_e\rangle + ( \gamma_{||-} |g\rangle + \gamma_{||+} |e\rangle) |\psi_{||}\rangle \right] \tag{B.2}$$

where the coefficients $\gamma_{||-} = \langle \psi_{||} | \psi_- \rangle$, $\gamma_{||+} = \langle \psi_{||} | \psi_+ \rangle$, and so forth represent the overlaps between the displaced states and our chosen decomposition, this decomposition is visualized in Fig. B.1.

To model the measurement process, we need to transform the pure state $|\Psi\rangle$ into its corresponding density matrix and trace over the cavity degrees of freedom to obtain the reduced qubit

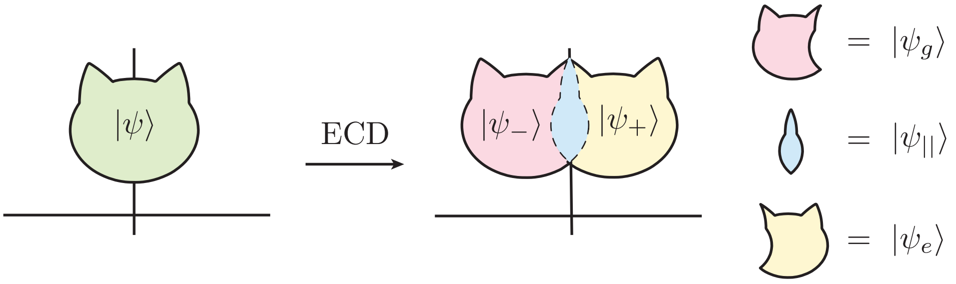

Figure B.1: **State decomposition after ECD.** An ECD gate displaces the cavity components associated to $|g\rangle$ and $|e\rangle$ in opposite directions as visualized by $|\psi_-\rangle$ and $|\psi_+\rangle$, respectively. If the displacement is sufficiently small, $|\psi_-\rangle$ and $|\psi_+\rangle$ will overlap as indicated by the blue region. To simplify the calculation, we decompose our state into three parts: one entangled only with $|g\rangle$ (red region), one entangled only with $|e\rangle$ (yellow region), and one entangled with both $|g\rangle$ and $|e\rangle$ (blue region).

density matrix. Due to the orthogonality of our chosen cavity basis states, only the diagonal elements $|\psi_g\rangle\langle\psi_g|$, $|\psi_e\rangle\langle\psi_e|$, and $|\psi_{||}\rangle\langle\psi_{||}|$ survive the partial trace operation. Further, since the final Ramsey measurement probes the qubit coherences through $\boldsymbol{\sigma}_x$ and $\boldsymbol{\sigma}_y$ operators, we only care about the off-diagonal elements of the reduced density matrix that contribute to $|g\rangle\langle e|$ and $|e\rangle\langle g|$ terms. Following, I will only write out these terms explicitly.

The partial trace over the cavity yields the reduced qubit density matrix:

$$\mathrm{tr}_{\mathrm{cav}}(|\Psi\rangle\langle\Psi|) = \frac{1}{2}\left(\gamma_{||-}\gamma^*_{||+}|g\rangle\langle e| + \gamma_{||+}\gamma^*_{||-}|e\rangle\langle g| + \dots\right) \tag{B.3}$$

The key insight emerges when we recognize that the product $\gamma_{||+}\gamma^*_{||-}$ directly encodes the characteristic function. Specifically:

$$\gamma_{||+}\gamma^*_{||-} = \langle\psi_-|\psi_{||}\rangle\langle\psi_{||}|\psi_+\rangle = \langle\psi_-|\psi_+\rangle = \langle\psi|\boldsymbol{D}(-\beta/2)\boldsymbol{D}(\beta/2)|\psi\rangle = \langle\boldsymbol{D}(\beta)\rangle \tag{B.4}$$

This result follows as $\langle\psi_-|\psi_g\rangle\langle\psi_g|\psi_+\rangle = \langle\psi_-|\psi_e\rangle\langle\psi_e|\psi_+\rangle = 0$.

Substituting this relationship into the reduced density matrix expression gives:

$$\mathrm{tr}_{\mathrm{cav}}(|\Psi\rangle\langle\Psi|) = \frac{1}{2}\left(\langle\boldsymbol{D}(\beta)\rangle^*|g\rangle\langle e| + \langle\boldsymbol{D}(\beta)\rangle|e\rangle\langle g| + \dots\right) \tag{B.5}$$

The final measurement step involves computing the expectation values of the Pauli operators $\sigma_x$ and $\sigma_y$ with respect to the reduced qubit state. These observables directly extract the real and imaginary components of the characteristic function:

$$\mathrm{tr}(|\Psi\rangle\langle\Psi|\boldsymbol{\sigma}_x) = \frac{1}{2}\left(\langle\boldsymbol{D}(\beta)\rangle + \langle\boldsymbol{D}(\beta)\rangle^*\right) = \mathrm{Re}(\langle\boldsymbol{D}(\beta)\rangle) \tag{B.6}$$

$$\mathrm{tr}(|\Psi\rangle\langle\Psi|\boldsymbol{\sigma}_y) = \frac{i}{2}\left(\langle\boldsymbol{D}(\beta)\rangle - \langle\boldsymbol{D}(\beta)\rangle^*\right) = \mathrm{Im}(\langle\boldsymbol{D}(\beta)\rangle) \tag{B.7}$$

This measurement protocol thus provides direct access to the characteristic function by mapping the expectation value of the displacement operator onto the qubit observables. It is important to note that the ECD gate comes with an intrinsic qubit-phase pickup that scales quadratically with the conditional displacement amplitude $\beta$ and has to be accounted for to avoid mixing real and imaginary part of $\mathcal{C}$.

# Appendix C

# Dynamics of interference features

Here, we derive the time evolution of the maxima of the interference blob amplitudes in the characteristic function under photon loss, corresponding to the momentum interference fringes in the Wigner function [166]. For this, we start from the marginal characteristic function.

$$C_{\pm,s,\tau}(0,\nu_p) = e^{-(1-\eta)\nu_p^2/2}/(2 \pm 2e^{|\alpha_0|^2}) \tag{C.1}$$

$$\times\,(2e^{-\eta\nu_p^2/2s^2} \pm e^{-(s|\alpha_0|-\sqrt{\eta}\nu_p)^2/2s^2} \tag{C.2}$$

$$\pm\, e^{-(s|\alpha_0|+\sqrt{\eta}\nu_p)^2/2s^2}) \tag{C.3}$$

where ± stand for an even or odd parity cat, $\nu_p = \mathrm{Im}[\nu]/\sigma_0$ is the normalized frequency of oscillations in the momentum marginal distribution, $\alpha_0 = \alpha/\sigma_0$ is the normalized amplitude of the coherent state, $s = e^{-\frac{\tau_s}{2T_1^c}}$ is the linear amplitude compression factor while $\tau_s$ is the exponential compression factor, $\eta = e^{-\frac{\tau}{T_1^c}}$ is the amplitude dumping faction as a function of $\tau$ and $\sigma_0$ is the standard deviation vacuum Gaussian. We can simplify this expression by considering the dynamics relative to the undamped cat state at $\tau = 0$ with compression factor $s$, which we find by calculating their ratio;

$$F_{s,\tau} = \frac{C_{\pm,s,\tau}(0,\nu_p)}{C_{\pm,s,0}(0,\nu_p)} = \exp\left(-\frac{1}{2}(e^{\tau/T_1^c} - 1)s^2|\alpha_0|^2\right) \tag{C.4}$$

We call this quantity the fidelity $F_{s,\tau}$, as it quantifies the amplitude of the decayed state relative to the undamped state. Smaller $s$ makes $F_{s,\tau}$ asymptotically approach unity and thus bring the blobs to their maximal amplitudes as $\tau$ and $\alpha_0$ increase. Furthermore, smaller $s$ corresponding to larger compression is required for larger $\alpha_0$ and larger $\tau$ to reach fidelity $F_{s,\tau} \to 1$. In the limit of short times $\tau \ll T_1^c$, we can approximate the scaling as:

$$F_{s,\tau} \approx \exp\left(-\frac{\tau}{2T_{\text{eff}}}|\alpha_0|^2\right) \tag{C.5}$$

Where $T_{eff} = T_1^c/s^2$ is the effective decay constant of a cat state with compression $s$. We use this model in the main text to find the effective decay constants for our data.

On the other hand, for longer times $\tau \gg T_1^c$, $F_{s,\tau}$ takes the form

$$F_{\pm,s,\tau} \approx \exp\left(-\frac{1}{2}e^{(\tau-\tau_s)/T_1^c}|\alpha_0|^2\right) \tag{C.6}$$

where the potential compression factor $\tau_s$ effectively reduces the decay time $\tau$. These dynamics fully describe the behavior of the interference blobs of the characteristic function under photo loss.

While a lower $s$ (higher compression) applied along the momentum axis to $\mathcal{C}_{\pm,s,\tau}(\nu_x, \nu_p)$ will protect the $\nu_p$ features, it will eventually increase the $\nu_x$ features, rendering it more vulnerable to photon loss. By choosing $s = |\alpha_0|^{-1}$, we can achieve a compression of the cat state that approximately symmetrizes the contours of both the Wigner and characteristic functions, protecting the $\nu_x$ and $\nu_p$ features equally. Under this, we can find the scaling for the fidelity of the interference blobs as

$$F_{\pm,s=|\alpha|^{-1},\tau} \approx \exp\left[-\frac{1}{2}(e^{\tau/T_1^c} - 1)\right] \tag{C.7}$$

which is a universal form, holding up for arbitrarily large $|\alpha_0|$. Meaning, the interference blobs do not decay faster for larger $|\alpha_0|$, but through the aid of compression, any of the interference blobs of any cat state can decay as for a small kitten with $\alpha_0 = 1$.

We can translate this analysis to parity decay as a function of cat size and compression. This recovers the expression derived in Ref. [122].

# Appendix D

# Predicting the geometric phase of a driven dispersively coupled QHO

The weak dispersive coupling regime utilizes large phase space displacements as a lever to achieve fast conditional displacements. However, the qubit picks up a trajectory-dependent geometric phase in the process, which has to be accounted for. Following, we will give a brief derivation of the equation we use to calculate that phase for a given qubit state. This discussion is based on an analysis done by my collaborator Kehui Yu.

The general Hamiltonian of a driven dispersively coupled QHO in the double rotation frame of the ancilla and QHO can be written as:

$$\frac{\boldsymbol{H}}{\hbar} = -\chi \boldsymbol{a}^\dagger \boldsymbol{a} \boldsymbol{q}^\dagger \boldsymbol{q} - \alpha \boldsymbol{q}^{\dagger \mathbf{2}} \boldsymbol{q} + \varepsilon(t) \boldsymbol{a}^\dagger + \varepsilon^*(t) \boldsymbol{a} \tag{D.1}$$

where $\chi$ is the dispersive coupling strength, $\alpha$ the ancilla anharmonicity, and I assumed that the other higher-order terms are negligible. Now, assuming the transmon to be in an energy eigenstate $|i\rangle$ allows us to rewrite the Hamiltonian as

$$\frac{\boldsymbol{H}}{\hbar} = -\chi_i \boldsymbol{a}^\dagger \boldsymbol{a} + \varepsilon(t) \boldsymbol{a}^\dagger + \varepsilon^*(t) \boldsymbol{a} \tag{D.2}$$

where $\chi_i$ is the corresponding dispersive coupling strength

The time evolution of this Hamiltonian is given by

$$\boldsymbol{U}(t) = e^{i\phi_i \boldsymbol{a}^\dagger \boldsymbol{a}} e^{\beta(t) \boldsymbol{a}^\dagger + \beta^*(t) \boldsymbol{a}} e^{\mathcal{O}(t^2)} \tag{D.3}$$

where $\phi_i(t) = \chi_i t$, $\beta(t) = \int_0^t -i\varepsilon(\tau) d\tau$ and $e^{\mathcal{O}(t^2)}$ contains resulting from applying the Baker–Campbell–Hausdorff formula.

For infinitesimal time intervals $dt$, we can drop the terms quadratic in $dt$ and write the action of the time evolution operator on an initial state $|\alpha_1\rangle$ as for one time step as:

$$\begin{aligned}
\boldsymbol{R}(d\phi_{g1})\boldsymbol{D}(d\beta_1)\,|\alpha_1\rangle &= \boldsymbol{R}(d\phi_{g1})\boldsymbol{D}(d\beta_1)\boldsymbol{D}(\alpha_1)\,|0\rangle && \text{(D.4)}\\
&= \boldsymbol{R}(d\phi_{g1})e^{(d\beta_1\alpha_1^* - d\beta_1^*\alpha_1)/2}\,|\alpha_1 + d\beta_1\rangle && \text{(D.5)}\\
&= e^{i\mathrm{Im}[d\beta_1\alpha_1^*]}\,|(\alpha_1 + d\beta_1)e^{id\phi_{g1}}\rangle && \text{(D.6)}\\
&= e^{i\mathrm{Im}[d\beta_1\alpha_1^*]}\,|\alpha_2\rangle && \text{(D.7)}\\
&= e^{id\theta_1}\,|\alpha_2\rangle && \text{(D.8)}
\end{aligned}$$

where $d\theta_j = \mathrm{Im}[d\beta_j\alpha_j^*]$. An additional time step takes us to

$$\begin{aligned}
\boldsymbol{R}(d\phi_{g2})\boldsymbol{D}(d\beta_2)e^{id\theta_1}\,|\alpha_2\rangle &= e^{id\theta_1}\boldsymbol{R}(d\phi_{g2})\boldsymbol{D}(d\beta_2)\,|\alpha_2\rangle && \text{(D.9)}\\
&= e^{i(d\theta_1 + d\theta_2)}\,|\alpha_3\rangle && \text{(D.10)}
\end{aligned}$$

We can thus find the acquired phase of the full sequence by solving the integral

$$\begin{aligned}
\theta_i(t) &= \int \mathrm{Im}[d\beta \cdot \alpha_i^*] && \text{(D.11)}\\
&= \int_0^t \mathrm{Im}[(d\beta(\tau)/dt)\alpha_i^*(\tau)]dt && \text{(D.12)}\\
&= \int_0^t \mathrm{Im}[(-i\epsilon(\tau))\alpha_i^*(\tau)]dt && \text{(D.13)}
\end{aligned}$$

where $\alpha_i$ is the trajectory for the qubit in $|i\rangle$. We use this formula to calculate the acquired phases on $|g\rangle$, $|e\rangle$, and $|f\rangle$ in the UECD transfer.

# Bibliography

[1] A. M. Turing, "On computable numbers, with an application to the entscheidungsproblem", *Proceedings of the London Mathematical Society*, 1936.

[2] C. E. Shannon, "A symbolic analysis of relay and switching circuits", *Electrical Engineering*, vol. 57, no. 12, pp. 713–723, 1938.

[3] C. E. Shannon, "A mathematical theory of communication", *The Bell System Technical Journal*, vol. 27, no. 3, pp. 379–423, 1948.

[4] A. Einstein, "The photoelectric effect", *Annalen der Physik*, vol. 17, pp. 132–147, 1905.

[5] L. de Broglie, "Recherches sur la théorie des quanta", PhD thesis, University of Paris, 1924.

[6] C. Davisson and L. H. Germer, "Diffraction of electrons by a crystal of nickel", *Phys. Rev.*, vol. 30, pp. 705–740, 6 1927. [Online]. Available: `https://link.aps.org/doi/10.1103/PhysRev.30.705`.

[7] J. V. Neumann, "Mathematical Foundations of Quantum Mechanics", First. Princeton University Press, 1932.

[8] A. Einstein, B. Podolsky, and N. Rosen, "Can quantum-mechanical description of physical reality be considered complete?" *Phys. Rev.*, vol. 47, pp. 777–780, 10 1935. [Online]. Available: `https://link.aps.org/doi/10.1103/PhysRev.47.777`.

[9] J. S. Bell, "On the einstein podolsky rosen paradox", *Physics Physique Fizika*, vol. 1, pp. 195–200, 3 1964. [Online]. Available: `https://link.aps.org/doi/10.1103/PhysicsPhysiqueFizika.1.195`.

[10] S. J. Freedman and J. F. Clauser, "Experimental test of local hidden-variable theories", *Phys. Rev. Lett.*, vol. 28, pp. 938–941, 14 1972. [Online]. Available: `https://link.aps.org/doi/10.1103/PhysRevLett.28.938`.

[11] A. Aspect, J. Dalibard, and G. Roger, "Experimental test of bell's inequalities using time-varying analyzers", *Phys. Rev. Lett.*, vol. 49, pp. 1804–1807, 25 1982. [Online]. Available: `https://link.aps.org/doi/10.1103/PhysRevLett.49.1804`.

[12] B. Hensen, H. Bernien, A. E. Dréau, A. Reiserer, N. Kalb, M. S. Blok, J. Ruitenberg, *et al.*, "Loophole-free bell inequality violation using electron spins separated by 1.3 kilometres", *Nature*, vol. 526, no. 7575, pp. 682–686, 2015. [Online]. Available: `https://doi.org/10.1038/nature15759`.

[13] M. Giustina, M. A. M. Versteegh, S. Wengerowsky, J. Handsteiner, A. Hochrainer, K. Phelan, F. Steinlechner, J. Kofler, J.-Å. Larsson, C. Abellán, W. Amaya, V. Pruneri, M. W. Mitchell, J. Beyer, T. Gerrits, A. E. Lita, L. K. Shalm, S. W. Nam, T. Scheidl, R. Ursin, B. Wittmann, and A. Zeilinger, "Significant-loophole-free test of bell's theorem with entangled photons", *Physical Review Letters*, vol. 115, p. 250 401, 2015. [Online]. Available: `https://doi.org/10.1103/PhysRevLett.115.250401`.

[14] J. Bardeen and W. H. Brattain, "The transistor, a semi-conductor triode", *Phys. Rev.*, vol. 74, pp. 230–231, 2 1948. [Online]. Available: `https://link.aps.org/doi/10.1103/PhysRev.74.230`.

[15] G. E. Moore *et al.*, "Cramming more components onto integrated circuits", 1965.

[16] Cerebras Systems, "Cerebras systems unveils world's fastest ai chip with whopping 4 trillion transistors",, 2024. [Online]. Available: `https://www.cerebras.ai/press-release/cerebras-announces-third-generation-wafer-scale-engine`.

[17] C. E. Leiserson, N. C. Thompson, J. S. Emer, B. C. Kuszmaul, B. W. Lampson, D. Sanchez, and T. B. Schardl, "There's plenty of room at the top: What will drive computer performance after moore's law?" *Science*, vol. 368, no. 6495, eaam9744, 2020.

[18] D. Deutsch, "Quantum theory, the church-turing principle and the universal quantum computer", *Proceedings of the Royal Society of London. A. Mathematical and Physical Sciences*, vol. 400, no. 1818, pp. 97–117, 1985.

[19] D. Deutsch and R. Jozsa, "Rapid solution of problems by quantum computation", *Proceedings of the Royal Society of London. Series A: Mathematical and Physical Sciences*, vol. 439, no. 1907, pp. 553–558, 1992.

[20] P. W. Shor, “Polynomial-time algorithms for prime factorization and discrete logarithms on a quantum computer”, *SIAM Journal on Computing*, vol. 26, no. 5, pp. 1484–1509, 1997.

[21] L. K. Grover, “A fast quantum mechanical algorithm for database search”, *arXiv preprint quant-ph/9605043*, 1996.

[22] P. W. Shor, “Scheme for reducing decoherence in quantum computer memory”, *Physical Review A*, vol. 52, no. 4, R2493–R2496, 1995.

[23] A. M. Steane, “Multiple-particle interference and quantum error correction”, *Proceedings of the Royal Society of London. Series A: Mathematical, Physical and Engineering Sciences*, vol. 452, no. 1954, pp. 2551–2577, 1996. arXiv: `quant-ph/9601029`.

[24] D. Gottesman, “Class of quantum error-correcting codes saturating the quantum hamming bound”, *Physical Review A*, vol. 54, no. 3, pp. 1862–1868, 1996. arXiv: `quant-ph/9604038`.

[25] A. Kitaev, “Fault-tolerant quantum computation by anyons”, *Annals of Physics*, vol. 303, no. 1, pp. 2–30, 2003. arXiv: `quant-ph/9707021`.

[26] D. Aharonov and M. Ben-Or, “Fault-tolerant quantum computation with constant error”,, pp. 176–188, 1997.

[27] A. Y. Kitaev, “Quantum computations: Algorithms and error correction”, *Russian Mathematical Surveys*, vol. 52, no. 6, pp. 1191–1249, 1997.

[28] J. P. Dowling and G. J. Milburn, “Quantum technology: The second quantum revolution”, *Philosophical Transactions of the Royal Society of London. Series A: Mathematical, Physical and Engineering Sciences*, vol. 361, no. 1809, pp. 1655–1674, 2003. arXiv: `quant-ph/0206091`.

[29] C. Monroe, D. Meekhof, B. King, W. Itano, and D. Wineland, “Demonstration of a fundamental quantum logic gate”, *Physical Review Letters*, vol. 75, no. 25, pp. 4714–4717, 1995.

[30] M. Brune, F. Schmidt-Kaler, A. Maali, J. Dreyer, E. Hagley, J. Raimond, and S. Haroche, “Quantum rabi oscillation: A direct test of field quantization in a cavity”, *Physical Review Letters*, vol. 76, no. 11, pp. 1800–1803, 1996.

[31] Y. Nakamura, Y. A. Pashkin, and J. Tsai, "Coherent control of macroscopic quantum states in a single-cooper-pair box", *nature*, vol. 398, no. 6730, pp. 786–788, 1999.

[32] A. J. Leggett, "Macroscopic quantum systems and the quantum theory of measurement", *Progress of Theoretical Physics Supplement*, vol. 69, pp. 80–100, 1980.

[33] J. M. Martinis, M. H. Devoret, and J. Clarke, "Energy-level quantization in the zero-voltage state of a current-biased josephson junction", *Physical Review Letters*, vol. 55, no. 15, pp. 1543–1546, 1985.

[34] V. Bouchiat, D. Vion, P. Joyez, D. Esteve, and M. H. Devoret, "Quantum coherence with a single cooper pair", *Physica Scripta*, vol. 1998, no. T76, pp. 165–170, 1998.

[35] M. Metcalfe, E. Boaknin, V. Manucharyan, R. Vijay, I. Siddiqi, C. Rigetti, L. Frunzio, R. Schoelkopf, and M. Devoret, "Measuring the decoherence of a quantronium qubit with the cavity bifurcation amplifier", *Physical Review B*, vol. 76, no. 17, p. 174 516, 2007. arXiv: `0706.0765`.

[36] A. Blais, R.-S. Huang, and A. Wallraff, "Cavity quantum electrodynamics for superconducting electrical circuits: An architecture for quantum computation", *Physical Review A—Atomic, Molecular, and Optical Physics*, vol. 69, no. 6, p. 062 320, 2004.

[37] J. Koch, T. M. Yu, J. Gambetta, A. A. Houck, D. I. Schuster, J. Majer, A. Blais, M. H. Devoret, S. M. Girvin, and R. J. Schoelkopf, "Charge-insensitive qubit design derived from the cooper pair box", *Physical Review A*, vol. 76, no. 4, p. 042 319, 2007. arXiv: `cond-mat/0703002`.

[38] A. A. Houck, J. A. Schreier, B. R. Johnson, J. M. Chow, J. Koch, J. M. Gambetta, D. I. Schuster, L. Frunzio, M. H. Devoret, S. M. Girvin, and R. J. Schoelkopf, "Controlling the spontaneous emission of a superconducting transmon qubit", *Phys. Rev. Lett.*, vol. 101, p. 080 502, 8 2008. [Online]. Available: `https://link.aps.org/doi/10.1103/PhysRevLett.101.080502`.

[39] H. Paik, D. I. Schuster, L. S. Bishop, G. Kirchmair, G. Catelani, A. P. Sears, B. R. Johnson, M. J. Reagor, L. Frunzio, L. I. Glazman, S. M. Girvin, M. H. Devoret, and R. J. Schoelkopf, "Observation of high coherence in josephson junction qubits measured in a three-dimensional circuit qed architecture", *Phys. Rev. Lett.*, vol. 107, p. 240 501, 24 2011. [Online]. Available: `https://link.aps.org/doi/10.1103/PhysRevLett.107.240501`.

[40] F. Arute, K. Arya, R. Babbush, D. Bacon, J. C. Bardin, R. Barends, R. Biswas, S. Boixo, F. G. Brandao, D. A. Buell, *et al.*, "Quantum supremacy using a programmable superconducting processor", *Nature*, vol. 574, no. 7779, pp. 505–510, 2019.

[41] E. Dennis, A. Kitaev, A. Landahl, and J. Preskill, "Topological quantum memory", *Journal of Mathematical Physics*, vol. 43, no. 9, pp. 4452–4505, 2002.

[42] A. G. Fowler, M. Mariantoni, J. M. Martinis, and A. N. Cleland, "Surface codes: Towards practical large-scale quantum computation", *Physical Review A—Atomic, Molecular, and Optical Physics*, vol. 86, no. 3, p. 032 324, 2012.

[43] D. Gottesman, A. Kitaev, and J. Preskill, "Encoding a qubit in an oscillator", *Physical Review A*, vol. 64, no. 1, p. 012 310, 2001.

[44] S. L. Braunstein and P. Van Loock, "Quantum information with continuous variables", *Reviews of modern physics*, vol. 77, no. 2, pp. 513–577, 2005.

[45] M. Reagor, W. Pfaff, C. Axline, R. W. Heeres, N. Ofek, K. Sliwa, E. Holland, C. Wang, J. Blumoff, K. Chou, M. J. Hatridge, L. Frunzio, M. H. Devoret, L. Jiang, and R. J. Schoelkopf, "Quantum memory with millisecond coherence in circuit qed", *Phys. Rev. B*, vol. 94, p. 014 506, 1 2016. [Online]. Available: `https://link.aps.org/doi/10.1103/PhysRevB.94.014506`.

[46] P. Campagne-Ibarcq, A. Eickbusch, S. Touzard, E. Zalys-Geller, N. E. Frattini, V. V. Sivak, P. Reinhold, S. Puri, S. Shankar, R. J. Schoelkopf, L. Frunzio, M. Mirrahimi, and M. H. Devoret, "Quantum error correction of a qubit encoded in grid states of an oscillator", *Nature*, vol. 584, no. 7821, pp. 368–372, 2020. arXiv: `1907.12487`. [Online]. Available: `https://www.nature.com/articles/s41586-020-2603-3`.

[47] M. Mirrahimi, Z. Leghtas, V. V. Albert, S. Touzard, R. J. Schoelkopf, L. Jiang, and M. H. Devoret, "Dynamically protected cat-qubits: A new paradigm for universal quantum computation", *New Journal of Physics*, vol. 16, p. 045 014, 2014.

[48] Z. Ni, S. Li, X. Deng, Y. Cai, L. Zhang, W. Wang, Z.-B. Yang, H. Yu, F. Yan, S. Liu, C.-L. Zou, L. Sun, S.-B. Zheng, Y. Xu, and D. Yu, "Beating the break-even point with a discrete-variable-encoded logical qubit", *Nature*, vol. 616, pp. 56–60, 2023.

[49] J. D. Teoh, P. Winkel, H. K. Babla, B. J. Chapman, J. Claes, S. J. de Graaf, J. W. O. Garmon, W. D. Kalfus, Y. Lu, A. Maiti, K. Sahay, N. Thakur, T. Tsunoda, S. H. Xue, L. Frunzio, S. M. Girvin, S. Puri, and R. J. Schoelkopf, "Dual-rail encoding with superconducting cavities", *Proceedings of the National Academy of Sciences*, vol. 120, no. 41, e2221736120, 2023.

[50] K. S. Chou, T. Shemma, H. McCarrick, T.-C. Chen, D. R. M. Arvidsson-Shukur, J. Claes, L. C. G. Govia, Y. Lu, L. Menard-Jacobs, A. Milsted, K. Noh, T. Tsunoda, J. O. Yen, L. Frunzio, S. M. Girvin, L. Jiang, S. Puri, and R. J. Schoelkopf, "A superconducting dual-rail cavity qubit with erasure-detected logical measurements", *Nature Physics*, vol. 20, pp. 1454–1460, 2024. [Online]. Available: `https://www.nature.com/articles/s41567-024-02539-4`.

[51] S. J. de Graaf, S. H. Xue, B. J. Chapman, J. D. Teoh, T. Tsunoda, P. Winkel, J. W. Garmon, K. M. Chang, L. Frunzio, S. Puri, *et al.*, "A mid-circuit erasure check on a dual-rail cavity qubit using the joint-photon number-splitting regime of circuit qed", *npj Quantum Information*, vol. 11, no. 1, p. 1, 2025.

[52] N. Ofek, A. Petrenko, R. Heeres, P. Reinhold, Z. Leghtas, B. Vlastakis, Y. Liu, L. Frunzio, S. M. Girvin, L. Jiang, M. Mirrahimi, M. H. Devoret, and R. J. Schoelkopf, "Extending the lifetime of a quantum bit with error correction in superconducting circuits", *Nature*, vol. 536, no. 7617, pp. 441–445, 2016.

[53] V. V. Sivak, A. Eickbusch, B. Royer, S. Singh, I. Tsioutsios, S. Ganjam, A. Miao, B. L. Hodson, A. J. Hung, L. Ding, *et al.*, "Real-time quantum error correction beyond break-even", *Nature*, vol. 616, no. 7955, pp. 50–55, 2023. arXiv: `2211.09116`.

[54] Y. Y. Gao, M. A. Rol, S. Touzard, and C. Wang, "Practical guide for building superconducting quantum devices", *PRX Quantum*, vol. 2, p. 040 202, 4 2021. [Online]. Available: `https://link.aps.org/doi/10.1103/PRXQuantum.2.040202`.

[55] A. Blais, A. L. Grimsmo, S. M. Girvin, and A. Wallraff, "Circuit quantum electrodynamics", *Rev. Mod. Phys.*, vol. 93, p. 025 005, 2 2021. [Online]. Available: `https://link.aps.org/doi/10.1103/RevModPhys.93.025005`.

[56] S. Haroche and J.-M. Raimond, "Exploring the Quantum: Atoms, Cavities, and Photons", (Oxford Graduate Texts). Oxford, UK: Oxford University Press, 2006, ISBN: 9780198509141.

[57] M. A. Nielsen and I. L. Chuang, "Quantum Computation and Quantum Information: 10th Anniversary Edition", 10th Anniversary. Cambridge, UK: Cambridge University Press, 2010, ISBN: 9781107002173.

[58] M. J. Reagor, "Superconducting cavities for circuit quantum electrodynamics", Ph.D. thesis, Yale University, 2016.

[59] C. J. Axline, "Building blocks for modular circuit qed quantum computing", Ph.D. thesis, Yale University, 2018.

[60] Y. Y. Gao, "Multi-cavity operations in circuit quantum electrodynamics", Ph.D. thesis, Yale University, 2018.

[61] S. Touzard, "Stabilization of bosonic codes in superconducting circuits", Dissertation director: Michel H. Devoret, Ph.D. thesis, Yale University, 2019.

[62] E. P. Wigner, "On the quantum correction for thermodynamic equilibrium", *Physical Review*, vol. 40, no. 5, pp. 749–759, 1932. [Online]. Available: `https://doi.org/10.1103/PhysRev.40.749`.

[63] R. L. Hudson, "When is the wigner quasi-probability density non-negative?" *Reports on Mathematical Physics*, vol. 6, pp. 249–252, 1974.

[64] A. Mari and J. Eisert, "Positive wigner functions render classical simulation of quantum computation efficient", *Physical Review Letters*, vol. 109, p. 230 503, 2012.

[65] C. M. Caves, "Quantum-mechanical noise in an interferometer", *Physical Review D*, vol. 23, no. 8, pp. 1693–1708, 1981.

[66] J. Aasi *et al.*, "Enhanced sensitivity of the ligo gravitational wave detector by using squeezed states of light", *Nature Photonics*, vol. 7, no. 8, pp. 613–619, 2013.

[67] X. Pan, T. Krisnanda, A. Duina, K. Park, P. Song, C. Y. Fontaine, A. Copetudo, R. Filip, and Y. Y. Gao, "Realization of versatile and effective quantum metrology using a single bosonic mode", *PRX Quantum*, vol. 6, p. 010 304, 2025.

[68] A. Joshi, "High-q tantalum resonators for circuit qed", Thesis Advisor: Assistant Professor Yvonne Y. Gao, M.S. thesis, National University of Singapore, Singapore, 2023.

[69] S. S. Ganjam, "Improving the coherence of superconducting quantum circuits through loss characterization and design optimization", Ph.D. dissertation, Yale University, 2024.

[70] C. R. H. McRae, H. Wang, J. Gao, M. R. Vissers, T. Brecht, A. Dunsworth, D. P. Pappas, and J. Mutus, “Materials loss measurements using superconducting microwave resonators”, *Review of Scientific Instruments*, vol. 91, no. 9, p. 091 101, 2020.

[71] M. Reagor, W. Pfaff, C. Axline, R. W. Heeres, N. Ofek, K. Sliwa, E. Holland, C. Wang, J. Blumoff, K. Chou, M. J. Hatridge, L. Frunzio, M. H. Devoret, L. Jiang, and R. J. Schoelkopf, “Quantum memory with millisecond coherence in circuit QED”, *Phys. Rev. B*, vol. 94, p. 014 506, 1 2016. [Online]. Available: `https://link.aps.org/doi/10.1103/PhysRevB.94.014506`.

[72] C. A. Brasil, F. F. Fanchini, and R. d. J. Napolitano, “A simple derivation of the lindblad equation”, *arXiv preprint arXiv:1110.2122*, 2011.

[73] B. D. Josephson, “Possible new effects in superconductive tunnelling”, *Physics letters*, vol. 1, no. 7, pp. 251–253, 1962.

[74] F. Motzoi, J. M. Gambetta, P. Rebentrost, and F. K. Wilhelm, “Simple pulses for elimination of leakage in weakly nonlinear qubits”, *Physical Review Letters*, vol. 103, no. 11, p. 110 501, 2009. [Online]. Available: `https://doi.org/10.1103/PhysRevLett.103.110501`.

[75] J. M. Martinis, K. B. Cooper, R. McDermott, M. Steffen, M. Ansmann, K. D. Osborn, K. Cicak, S. Oh, D. P. Pappas, R. W. Simmonds, and C. C. Yu, “Decoherence in josephson qubits from dielectric loss”, *Phys. Rev. Lett.*, vol. 95, p. 210 503, 21 2005. [Online]. Available: `https://link.aps.org/doi/10.1103/PhysRevLett.95.210503`.

[76] J. J. Burnett, A. Bengtsson, M. Scigliuzzo, *et al.*, “Decoherence benchmarking of superconducting qubits”, *npj Quantum Information*, vol. 5, no. 1, p. 54, 2019. [Online]. Available: `https://doi.org/10.1038/s41534-019-0168-5`.

[77] S. De Graaf, L. Ioffe, J. Burnett, S. Kubatkin, A. Danilov, and A. Y. Tzalenchuk, “Two-level systems in superconducting quantum devices due to trapped quasiparticles”, *Science Advances*, vol. 6, no. 51, eabc5055, 2020.

[78] S. Schlör, J. Lisenfeld, C. Müller, A. Bilmes, A. Schneider, D. P. Pappas, A. V. Ustinov, and M. Weides, “Correlating decoherence in transmon qubits: Low frequency noise by single fluctuators”, *Physical review letters*, vol. 123, no. 19, p. 190 502, 2019.

[79] T. Thorbeck, A. Eddins, I. Lauer, D. T. McClure, and M. Carroll, “Two-level-system dynamics in a superconducting qubit due to background ionizing radiation”, *PRX Quantum*, vol. 4, no. 2, p. 020 356, 2023.

[80] M. P. Bland, F. Bahrami, J. G. Martinez, P. H. Prestegaard, B. M. Smitham, A. Joshi, E. Hedrick, A. Pakpour-Tabrizi, S. Kumar, A. Jindal, *et al.*, “2d transmons with lifetimes and coherence times exceeding 1 millisecond”, *arXiv preprint arXiv:2503.14798*, 2025.

[81] M. Tuokkola, Y. Sunada, H. Kivijärvi, J. Albanese, L. Grönberg, J.-P. Kaikkonen, V. Vesterinen, J. Govenius, and M. Möttönen, “Methods to achieve near-millisecond energy relaxation and dephasing times for a superconducting transmon qubit”, *arXiv preprint arXiv:2407.18778*, 2024, arXiv:2407.18778. [Online]. Available: `https://arxiv.org/abs/2407.18778`.

[82] M. F. Dumas, B. Groleau-Paré, A. McDonald, M. H. Muñoz-Arias, C. Lledó, B. D’Anjou, and A. Blais, “Measurement-induced transmon ionization”, *Phys. Rev. X*, vol. 14, p. 041 023, 4 2024. [Online]. Available: `https://link.aps.org/doi/10.1103/PhysRevX.14.041023`.

[83] D. T. McClure, H. Paik, L. S. Bishop, M. Steffen, J. M. Chow, and J. M. Gambetta, “Rapid driven reset of a qubit readout resonator”, *Physical Review Applied*, vol. 5, no. 1, p. 011 001, 2016.

[84] A. Chatterjee, **Schwinger, Jonathan**, and Y. Y. Gao, “Enhanced qubit readout via reinforcement learning”, *Physical Review Applied*, vol. 23, no. 5, p. 054 057, 2025.

[85] M. A. Castellanos-Beltran and K. W. Lehnert, “Widely tunable parametric amplifier based on a superconducting quantum interference device array resonator”, *Applied Physics Letters*, vol. 91, no. 8, p. 083 509, 2007.

[86] K. O’Brien, C. Macklin, I. Siddiqi, and X. Zhang, “Resonant phase matching of josephson junction traveling wave parametric amplifiers”, *Physical Review Letters*, vol. 113, no. 15, p. 157 001, 2014.

[87] R. W. Heeres, P. Reinhold, N. Ofek, L. Frunzio, L. Jiang, M. H. Devoret, and R. J. Schoelkopf, “Implementing a universal gate set on a logical qubit encoded in an oscillator”, *Nature Communications*, vol. 8, no. 1, p. 94, 2017.

[88] L. Sun, A. Petrenko, Z. Leghtas, B. Vlastakis, G. Kirchmair, K. M. Sliwa, A. Narla, M. Hatridge, S. Shankar, J. Blumoff, L. Frunzio, M. Mirrahimi, M. H. Devoret, and R. J. Schoelkopf, "Tracking photon jumps with repeated quantum non-demolition parity measurements", *Nature*, vol. 511, no. 7510, pp. 444–448, 2014.

[89] A. L. Grimsmo, J. Combes, and B. Q. Baragiola, "Quantum computing with rotation-symmetric bosonic codes", *Physical Review X*, vol. 10, no. 1, p. 011 058, 2020.

[90] A. W. Eickbusch, "Quantum control and error correction of grid states in a superconducting oscillator", Ph.D. dissertation, Yale University, New Haven, CT, 2024. [Online]. Available: `https://elischolar.library.yale.edu/gsas_dissertations/1404/`.

[91] S. Krastanov, V. V. Albert, C. Shen, C.-L. Zou, R. W. Heeres, B. Vlastakis, R. J. Schoelkopf, and L. Jiang, "Universal control of an oscillator with dispersive coupling to a qubit", *Physical Review A*, vol. 92, no. 4, p. 040 303, 2015. [Online]. Available: `https://link.aps.org/doi/10.1103/PhysRevA.92.040303`.

[92] C. Arenz, D. I. Bondar, D. Burgarth, C. Cormick, and H. Rabitz, "Amplification of quadratic hamiltonians", *Quantum*, vol. 4, p. 271, 2020. arXiv: `1806.00444`. [Online]. Available: `https://quantum-journal.org/papers/q-2020-05-25-271/`.

[93] S. Touzard, "[title not found - work focused on stabilizing bosonic codes in superconducting circuits]", Supervisor: Michel H. Devoret, Ph.D. dissertation, Yale University, New Haven, CT, 2020.

[94] Y. Y. Gao, B. J. Lester, Y. Zhang, C. Wang, S. Rosenblum, L. Frunzio, L. Jiang, S. M. Girvin, and R. J. Schoelkopf, "Programmable interference between two microwave quantum memories", *Physical Review X*, vol. 8, no. 2, p. 021 073, 2018. arXiv: `1802.08510 [quant-ph]`. [Online]. Available: `https://link.aps.org/doi/10.1103/PhysRevX.8.021073`.

[95] N. E. Frattini, U. Vool, S. Shankar, A. Narla, K. M. Sliwa, and M. H. Devoret, "3-wave mixing josephson dipole element", *Applied Physics Letters*, vol. 110, no. 22, p. 222 603, 2017. arXiv: `1702.00869 [cond-mat.supr-con]`. [Online]. Available: `https://doi.org/10.1063/1.4984142`.

[96] A. Maiti, J. W. O. Garmon, Y. Lu, A. Miano, L. Frunzio, and R. J. Schoelkopf, "A linear quantum coupler for clean bosonic control", *arXiv preprint arXiv:2501.18025*, 2025. arXiv: `2501.18025 [quant-ph]`. [Online]. Available: `https://arxiv.org/abs/2501.18025`.

[97] C. Wang, Y. Y. Gao, P. Reinhold, R. W. Heeres, N. Ofek, K. Chou, C. Axline, M. Reagor, J. Blumoff, K. M. Sliwa, L. Frunzio, S. M. Girvin, L. Jiang, M. Mirrahimi, M. H. Devoret, and R. J. Schoelkopf, "A schrödinger cat living in two boxes", *Science*, vol. 352, no. 6289, pp. 1087–1091, 2016.

[98] A. Grimm, N. E. Frattini, S. Puri, S. O. Mundhada, S. Touzard, M. Mirrahimi, S. M. Girvin, S. Shankar, and M. H. Devoret, "Stabilization and operation of a Kerr-cat qubit", *Nature*, vol. 584, pp. 205–209, 2020.

[99] A. Eickbusch, V. Sivak, A. Z. Ding, S. S. Elder, S. R. Jha, J. Venkatraman, B. Royer, S. M. Girvin, R. J. Schoelkopf, and M. H. Devoret, "Fast universal control of an oscillator with weak dispersive coupling to a qubit", *Nature Physics*, vol. 18, no. 12, pp. 1464–1469, 2022.

[100] V. Sivak, "Quantum error correction beyond break-even", Dissertation Director: Michel H. Devoret, Ph.D. dissertation, Yale University Graduate School of Arts and Sciences, 2023. [Online]. Available: `https://elischolar.library.yale.edu/gsas_dissertations/895`.

[101] E. Schrödinger, "Die gegenwärtige situation in der quantenmechanik", *Naturwissenschaften*, vol. 23, no. 50, pp. 844–849, 1935.

[102] O. Milul, B. Guttel, U. Goldblatt, S. Hazanov, L. M. Joshi, D. Chausovsky, N. Kahn, E. Çiftyürek, F. Lafont, and S. Rosenblum, "A superconducting quantum memory with tens of milliseconds coherence time", *arXiv preprint arXiv:2302.06442*, 2023.

[103] W. H. Zurek, "Sub-Planck structure in phase space and its relevance for quantum decoherence", *Nature*, vol. 412, p. 712, 2001.

[104] W. Schleich, M. Pernigo, and F. L. Kien, "Nonclassical state from two pseudoclassical states", *Physical Review A*, vol. 44, p. 2172, 1991.

[105] C. Gerry and P. Knight, "Quantum superpositions and Schrödinger cat states in quantum optics", *American Journal of Physics*, vol. 65, p. 964, 1997.

[106] W. Qin, A. Miranowicz, H. Jing, and F. Nori, "Generating long-lived macroscopically distinct superposition states in atomic ensembles", *Physical Review Letters*, vol. 127, p. 093 602, 2021.

[107] J. Joo, W. J. Munro, and T. P. Spiller, "Quantum metrology with entangled coherent states", *Physical Review Letters*, vol. 107, p. 083 601, 2011.

[108] A. Facon, E.-K. Dietsche, D. Grosso, S. Haroche, J.-M. Raimond, M. Brune, and S. Gleyzes, "A sensitive electrometer based on a Rydberg atom in a Schrödinger-cat state", *Nature*, vol. 535, p. 262, 2016.

[109] P. A. Knott, T. J. Proctor, A. J. Hayes, J. P. Cooling, and J. A. Dunningham, "Practical quantum metrology with large precision gains in the low-photon-number regime", *Physical Review A*, vol. 93, p. 033 859, 2016.

[110] K. Duivenvoorden, B. M. Terhal, and D. Weigand, "Single-mode displacement sensor", *Physical Review A*, vol. 95, p. 012 305, 2017.

[111] S. J. van Enk and O. Hirota, "Entangled coherent states: Teleportation and decoherence", *Physical Review A*, vol. 64, p. 022 313, 2001.

[112] Z. Leghtas, S. Touzard, I. M. Pop, A. Kou, B. Vlastakis, A. Petrenko, K. M. Sliwa, A. Narla, S. Shankar, M. J. Hatridge, M. Reagor, L. Frunzio, R. J. Schoelkopf, M. Mirrahimi, and M. H. Devoret, "Confining the state of light to a quantum manifold by engineered two-photon loss", *Science*, vol. 347, pp. 853–857, 2015.

[113] S. Puri, S. Boutin, and A. Blais, "Engineering the quantum states of light in a Kerr-nonlinear resonator by two-photon driving", *npj Quantum Information*, vol. 3, p. 18, 2017.

[114] S. Touzard, A. Grimm, Z. Leghtas, S. O. Mundhada, P. Reinhold, C. Axline, M. Reagor, K. Chou, J. Blumoff, K. M. Sliwa, S. Shankar, L. Frunzio, R. J. Schoelkopf, M. Mirrahimi, and M. H. Devoret, "Coherent oscillations inside a quantum manifold stabilized by dissipation", *Physical Review X*, vol. 8, p. 021 005, 2018.

[115] C. Chamberland, K. Noh, P. Arrangoiz-Arriola, E. T. Campbell, C. T. Hann, J. Iverson, H. Putterman, T. C. Bohdanowicz, S. T. Flammia, A. Keller, G. Refael, J. Preskill, L. Jiang, A. H. Safavi-Naeini, O. Painter, and F. G. S. L. Brandão, "Building a fault-tolerant quantum computer using concatenated cat codes", *PRX Quantum*, vol. 3, p. 010 329, 2022.

[116] S. Puri, L. St-Jean, J. A. Gross, A. Grimm, N. E. Frattini, P. S. Iyer, A. Krishna, S. Touzard, L. Jiang, A. Blais, T. Floquet, I. Siddiqi, S. M. Girvin, M. H. Devoret, and M. Mirrahimi, "Bias-preserving gates with stabilized cat qubits", *Science Advances*, vol. 6, eaay5901, 2020.

[117] R. Lescanne, M. Villiers, T. Peronnin, A. Sarlette, M. Delbecq, B. Huard, T. Kontos, M. Mirrahimi, and Z. Leghtas, "Exponential suppression of bit-flips in a qubit encoded in an oscillator", *Nature Physics*, vol. 16, pp. 509–513, 2020.

[118] K. Huang, H. Le Jeannic, J. Ruaudel, V. B. Verma, M. D. Shaw, F. Marsili, S. W. Nam, E. Wu, H. Zeng, Y.-C. Jeong, R. Filip, O. Morin, and J. Laurat, "Optical synthesis of large-amplitude squeezed coherent-state superpositions with minimal resources", *Phys. Rev. Lett.*, vol. 115, p. 023 602, 2015.

[119] J. Etesse, M. Bouillard, B. Kanseri, and R. Tualle-Brouri, "Experimental generation of squeezed cat states with an operation allowing iterative growth", *Phys. Rev. Lett.*, vol. 114, p. 193 602, 2015.

[120] H.-Y. Lo, D. Kienzler, L. de Clercq, M. Marinelli, V. Negnevitsky, B. C. Keitch, and J. P. Home, "Spin–motion entanglement and state diagnosis with squeezed oscillator wavepackets", *Nature*, vol. 521, p. 336, 2015.

[121] C. Flühmann and J. P. Home, "Direct characteristic-function tomography of quantum states of the trapped-ion motional oscillator", *Phys. Rev. Lett.*, vol. 125, p. 043 602, 2020.

[122] H. Le Jeannic, A. Cavaillès, K. Huang, R. Filip, and J. Laurat, "Slowing quantum decoherence by squeezing in phase space", *Phys. Rev. Lett.*, vol. 120, p. 073 603, 2018.

[123] A. Joshi, K. Noh, and Y. Y. Gao, "Quantum information processing with bosonic qubits in circuit QED", *Quantum Science and Technology*, vol. 6, no. 3, p. 033 001, 2021.

[124] D. S. Schlegel, F. Minganti, and V. Savona, "Quantum error correction using squeezed Schrödinger cat states", *Physical Review A*, vol. 106, p. 022 431, 2022.

[125] Q. Xu, G. Zheng, Y.-X. Wang, P. Zoller, A. A. Clerk, and L. Jiang, "Autonomous quantum error correction and fault-tolerant quantum computation with squeezed cat qubits", *arXiv preprint arXiv:2210.13406*, 2022.

[126] R. Rousseau, D. Ruiz, E. Albertinale, P. d'Avezac, D. Banys, U. Blandin, N. Bourdaud, G. Campanaro, G. Cardoso, N. Cottet, C. Cullip, S. Deléglise, L. Devanz, A. Devulder, A. Essig, P. Février, A. Gicquel, É. Gouzien, A. Gras, J. Guillaud, E. Gümüş, M. Hallén, A. Jacob, P. Magnard, A. Marquet, S. Miklass, T. Peronnin, S. Polis, F. Rautschke, U. Réglade, J. Roul, J. Stevens, J. Solard, A. Thomas, J.-L. Ville, P. Wan-Fat, R. Lescanne, Z. Leghtas, J. Cohen, S. Jezouin, and A. Murani, "Enhancing dissipative cat qubit protection by squeezing", *arXiv preprint arXiv:2502.07892*, 2025.

[127] X. Pan, **Schwinger, Jonathan**, N.-N. Huang, P. Song, W. Chua, F. Hanamura, A. Joshi, F. Valadares, R. Filip, and Y. Y. Gao, "Protecting the quantum interference of cat states by phase-space compression", *Physical Review X*, vol. 13, no. 2, p. 021 004, 2023.

[128] U. Leonhardt, "Essential Quantum Optics: From Quantum Measurements to Black Holes", Cambridge, England: Cambridge University Press, 2010.

[129] R. Filip, "Amplification of Schrödinger-cat state in a degenerate optical parametric amplifier", *J. Opt. B*, vol. 3, S1, 2001.

[130] A. Serafini, S. De Siena, F. Illuminati, and M. G. Paris, "Minimum decoherence cat-like states in Gaussian noisy channels", *J. Opt. B*, vol. 6, S591, 2004.

[131] D. Menzies and R. Filip, "Gaussian-optimized preparation of non-Gaussian pure states", *Phys. Rev. A*, vol. 79, p. 012 313, 2009.

[132] R. Filip, "Gaussian quantum adaptation of non-Gaussian states for a lossy channel", *Phys. Rev. A*, vol. 87, p. 042 308, 2013.

[133] K. Park, J. Hastrup, J. S. Neergaard-Nielsen, J. B. Brask, R. Filip, and U. L. Andersen, "Slowing quantum decoherence of oscillators by hybrid processing", *npj Quantum Inf.*, vol. 8, p. 67, 2022.

[134] R. Y. Teh, P. D. Drummond, and M. D. Reid, "Overcoming decoherence of Schrödinger cat states formed in a cavity using squeezed-state inputs", *Phys. Rev. Res.*, vol. 2, p. 043 387, 2020.

[135] P. Winkel, I. Takmakov, D. Rieger, L. Planat, W. Hasch-Guichard, L. Grünhaupt, N. Maleeva, F. Foroughi, F. Henriques, K. Borisov, J. Ferrero, A. V. Ustinov, W. Wernsdorfer, N. Roch, and I. M. Pop, "Nondegenerate parametric amplifiers based on dispersion-engineered Josephson-junction arrays", *Physical Review Applied*, vol. 13, p. 024 015, 2020.

[136] J. Gambetta, W. A. Braff, A. Wallraff, S. M. Girvin, and R. J. Schoelkopf, "Protocols for optimal readout of qubits using a continuous quantum nondemolition measurement", *Physical Review A*, vol. 76, p. 012 325, 2007.

[137] J. Hastrup, K. Park, R. Filip, and U. L. Andersen, "Unconditional preparation of squeezed vacuum from rabi interactions", *Phys. Rev. Lett.*, vol. 126, p. 153 602, 2021.

[138] I. Strandberg, "Simple, reliable, and noise-resilient continuous-variable quantum state tomography with convex optimization", *Physical Review Applied*, vol. 18, p. 044 041, 2022.

[139] T. Hillmann and F. Quijandría, "Quantum error correction with dissipatively stabilized squeezed-cat qubits", *Phys. Rev. A*, vol. 107, p. 032 423, 3. [Online]. Available: `https://link.aps.org/doi/10.1103/PhysRevA.107.032423`.

[140] Q. Xu, G. Zheng, Y.-X. Wang, P. Zoller, A. A. Clerk, and L. Jiang, "Autonomous quantum error correction and fault-tolerant quantum computation with squeezed cat qubits", *npj Quantum Information*, vol. 9, no. 1, p. 78, 2023.

[141] W. J. Munro, K. Nemoto, G. J. Milburn, and S. L. Braunstein, "Weak-force detection with superposed coherent states", *Physical Review A*, vol. 66, p. 023 819, 2002.

[142] W. Dür, G. Vidal, and J. I. Cirac, "Three qubits can be entangled in two inequivalent ways", *Physical Review A*, vol. 62, p. 062 314, 2000.

[143] V. Gorbachev and A. Trubilko, "On multiparticle w states, their implementations and application in the quantum informational problems", *Laser Physics Letters*, vol. 3, no. 2, pp. 59–70, 2006.

[144] J. Wang, Q. Zhang, and C.-J. Tang, "Quantum secure communication scheme with W state", *Communications in Theoretical Physics*, vol. 48, no. 4, p. 637, 2007.

[145] C. Zhu, F. Xu, and C. Pei, "W-state analyzer and multi-party measurement-device-independent quantum key distribution", *Scientific reports*, vol. 5, no. 1, p. 17 449, 2015.

[146] H. Häffner, W. Hänsel, C. Roos, J. Benhelm, D. Chek-al-Kar, M. Chwalla, T. Körber, U. Rapol, M. Riebe, P. Schmidt, *et al.*, "Scalable multiparticle entanglement of trapped ions", *Nature*, vol. 438, no. 7068, pp. 643–646, 2005.

[147] L. DiCarlo *et al.*, "Preparation and measurement of three-qubit entanglement in a superconducting circuit", *Nature*, vol. 467, pp. 574–578, 2010.

[148] S. Chakram, K. He, A. V. Dixit, A. E. Oriani, R. K. Naik, N. Leung, H. Kwon, W.-L. Ma, L. Jiang, and D. I. Schuster, "Multimode photon blockade", *Nature Physics*, vol. 18, no. 8, pp. 879–884, 2022.

[149] X.-L. Wang, L.-K. Chen, W. Li, H.-L. Huang, C. Liu, C. Chen, Y.-H. Luo, Z.-E. Su, D. Wu, Z.-D. Li, *et al.*, "Experimental ten-photon entanglement", *Physical review letters*, vol. 117, no. 21, p. 210 502, 2016.

[150] W. Asavanant, Y. Shiozawa, S. Yokoyama, B. Charoensombutamon, H. Emura, R. N. Alexander, S. Takeda, J.-i. Yoshikawa, N. C. Menicucci, H. Yonezawa, *et al.*, "Generation of time-domain-multiplexed two-dimensional cluster state", *Science*, vol. 366, no. 6463, pp. 373–376, 2019.

[151] J. Roslund, R. M. De Araujo, S. Jiang, C. Fabre, and N. Treps, "Wavelength-multiplexed quantum networks with ultrafast frequency combs", *Nature Photonics*, vol. 8, no. 2, pp. 109–112, 2014.

[152] M. V. Larsen, X. Guo, C. R. Breum, J. S. Neergaard-Nielsen, and U. L. Andersen, "Deterministic generation of a two-dimensional cluster state", *Science*, vol. 366, no. 6463, pp. 369–372, 2019.

[153] Q. Zhuang, Z. Zhang, and J. H. Shapiro, "Distributed quantum sensing using continuous-variable multipartite entanglement", *Physical Review A*, vol. 97, no. 3, p. 032 329, 2018.

[154] B. Royer, S. Singh, and S. Girvin, "Encoding qubits in multimode grid states", *PRX Quantum*, vol. 3, p. 010 335, 1 2022. [Online]. Available: `https://link.aps.org/doi/10.1103/PRXQuantum.3.010335`.

[155] Nord Quantique, "Suppressing logical errors with multimode quantum error correction", Technical Report, Nord Quantique, Sherbrooke, Quebec, Canada, 2025. [Online]. Available: `https://nordquantique.ca/uploads/blog/Nord_Quantique_-_Tesseract_technical_paper_May_2025.pdf`.

[156] J. Conrad, J. Eisert, and F. Arzani, "Gottesman-kitaev-preskill codes: A lattice perspective", *Quantum*, vol. 6, p. 648, 2022.

[157] S. Ganjam, Y. Wang, Y. Lu, A. Banerjee, C. U. Lei, L. Krayzman, K. Kisslinger, C. Zhou, R. Li, Y. Jia, *et al.*, "Surpassing millisecond coherence in on chip superconducting quantum memories by optimizing materials and circuit design", *Nature Communications*, vol. 15, no. 1, p. 3687, 2024.

[158] K. D. Crowley, R. A. McLellan, A. Dutta, N. Shumiya, A. P. M. Place, X. H. Le, Y. Gang, T. Madhavan, M. P. Bland, R. Chang, N. Khedkar, Y. C. Feng, E. A. Umbarkar, X. Gui, L. V. H. Rodgers, Y. Jia, M. M. Feldman, S. A. Lyon, M. Liu, R. J. Cava, A. A. Houck, and N. P. de Leon, "Disentangling losses in tantalum superconducting circuits", *Phys. Rev. X*, vol. 13, p. 041 005, 4 2023. [Online]. Available: `https://link.aps.org/doi/10.1103/PhysRevX.13.041005`.

[159] Z. K. Minev, Z. Leghtas, S. O. Mundhada, L. Christakis, I. M. Pop, and M. H. Devoret, "Energy-participation quantization of josephson circuits", *npj Quantum Information*, vol. 7, no. 1, p. 131, 2021.

[160] "Classification of mixed three-qubit states", *Physical Review Letters*, vol. 87, no. 4, p. 040 401, 2001.

[161] G. Q. AI and Collaborators, "Quantum error correction below the surface code threshold", *Nature*, vol. 638, no. 8052, pp. 920–926, 2025.

[162] S. Bravyi, A. W. Cross, J. M. Gambetta, D. Maslov, P. Rall, and T. J. Yoder, "High-threshold and low-overhead fault-tolerant quantum memory", *Nature*, vol. 627, no. 8005, pp. 778–782, 2024.

[163] H. Putterman, K. Noh, C. T. Hann, G. S. MacCabe, S. Aghaeimeibodi, R. N. Patel, M. Lee, W. M. Jones, H. Moradinejad, R. Rodriguez, *et al.*, "Hardware-efficient quantum error correction via concatenated bosonic qubits", *Nature*, vol. 638, no. 8052, pp. 927–934, 2025.

[164] K. Noh, S. Girvin, and L. Jiang, "Encoding an oscillator into many oscillators", *Physical Review Letters*, vol. 125, no. 8, p. 080 503, 2020.

[165] A. J. Brady, A. Eickbusch, S. Singh, J. Wu, and Q. Zhuang, "Advances in bosonic quantum error correction with gottesman–kitaev–preskill codes: Theory, engineering and applications", *Progress in Quantum Electronics*, vol. 93, p. 100 496, 2024.

[166] J. Janszky, A. Petak, C. Sibilia, M. Bertolotti, and P. Adam, "Optical schrödinger-cat states in a directional coupler", *Journal of Optics B*, vol. 7, p. 145, 1995.